Stefan Stoll
Spectral Simulations in Solid-State Electron Paramagnetic Resonance

Spectral Simulations in Solid-State Electron Paramagnetic Resonance

Dissertation for the degree of
Doctor of Natural Sciences

submitted to the
Eidgenössische Technische Hochschule Zürich

presented by
Stefan Stoll
Dipl.-Ing. Technical University Graz
Mag. art. Academy of Music Graz
born October 27, 1973
citizen of Austria, Italy

accepted on the recommendation of
Prof. Dr. Arthur Schweiger, examiner
Prof. Dr. Beat H. Meier, co-examiner

2003

On the front cover: the EasySpin grid from Figure 4.6 (p. 99), the sampling of a sinc function from Figure 3.15 (p. 75) and the adaptive eigenfield computation method from Figure 2.5 (p. 27). On the back cover: the adaptive grid for a looping transition (Figure 4.14, p. 111).

The Road to Wisdom. / The road to wisdom? – Well, it's plain / and simple to express: / Err / and err / and err again / but less / and less / and less.

Piet Hein[1] (1905–1996)

There is no science without fancy, and no art without facts.

Vladimir Nabokov[2] (1899–1977)

[1] "The Road to Wisdom", *Grooks*, MIT Press (1966), p. 34
[2] "An interview with Nabokov", *Wisconsin Studies in Contemporary Literature* **8**(2), 140–141 (1967)

German synopsis

In der Festkörper-EPR sind computergestützte numerische Simulationen unabdingbar, um verlässlich experimentelle Spektren von ungeordneten Systemen (Pulvern, Gläser, gefrorenen Lösungen) interpretieren und Rückschlüsse auf die elektronische Struktur der gemessenen paramagnetischen Substanzen ziehen zu können. Das Thema dieser Doktorarbeit sind die solchen Simulationen zu Grunde liegenden Prinzipien. An vielen Stellen konnten deutliche Verbesserungen theoretischer und algorithmischer Natur angebracht werden. Diese Verbesserungen bewirken deutlich kürzere Berechnungszeiten und eine allgemeinere Anwendbarkeit der Simulationsmethoden.

In dieser Arbeit konnten Simulationen von cw-EPR-, ENDOR- und Puls-EPR-Spektren von ungeordneten Systemen unter einem einheitlichen Schema zusammengefasst und algorithmisch gleich behandelt werden. Alle Simulationen bestehen aus zwei aufeinanderfolgenden Schritten.

Im ersten Schritt wird – ausgehend vom Spin-Hamiltonoperator und den experimentellen Parametern – eine Liste von spektralen Peaks mit deren Positionen, Amplituden und Linienbreiten berechnet. Eine Verbesserung für diesen Schritt ist eine neue, robuste Methode zur Berechnung von Resonanzfeldern für cw-EPR im Zustandsraum. Für die allgemeine quantenmechanische Berechnung von Puls-EPR-Linien wurden neue Formeln und ein generischer Algorithmus entwickelt, der für alle Pulssequenzen gültig ist. Die Liste spektraler Linien, definiert entweder auf einer Magnetfeld- (cw-EPR und Feldscans) oder einer Frequenzachse (alle anderen EPR-Varianten), kann interpolativ vergrößert werden. Für Puls-EPR wurde eine Methode entwickelt, die nur signifikante Linien berechnet und damit den Simulationszeitaufwand deutlich reduziert.

Im zweiten Schritt wird die so erhaltene Liste spektraler Linien zur Berechnung des Spektrums verwendet. Je nach Art des Experiments müssen unterschiedliche Methoden benutzt werden. In dieser Arbeit wurde ein neuer Algorithmus zur Umwandlung von Puls-EPR-Peakdaten in ein Zeitdomänensignal entwickelt, der Berechnungszeiten verkürzt und die Genauigkeit erhöht.

Die Verbesserungen schließen mit einer Neubewertung der verschiedenen Orientierungsnetze, auf die EPR- und NMR-Simulationen von ungeordneten Systemen aufbauen. Zum ersten Mal wurden korrekte Gewichtungsfaktoren für homogene Netze berechnet. Ein ganz neuer Ansatz wird mit adaptiven Netzen präsentiert. Diese ermöglichen es, der stark schwankenden Abhängigkeit eines EPR-Spektrums von der Orientierung des paramagnetischen Zentrums Rechnung zu tragen und nur relevante Orientierungen in die Simulation mit einzubeziehen. Vor allem bei der Berechnung von stark orientierungsselektiven ENDOR- und Puls-EPR-Experimenten ergeben sich dadurch deutliche Zeitgewinne.

Russian synopsis

Для получения информации об электронной структуре парамагнитных центров в твердых неупорядоченных системах (порошки, стекла, замороженные растворы) необходима надежная интерпретация спектров ЭПР этих центров. Данная диссертация посвящена принципам, лежащим в основе компьютерного моделирования спектров ЭПР. Предложены существенные усовершенствования как в теории расчета, так и в компьютерных алгоритмах. Усовершенствования привели к значительному увеличению производительности вычислений и расширили область применимости симуляций.

В данной работе моделирование спектров непрерывного и импульсного ЭПР и ДЭЯР в неупорядоченных системах осуществляется по единой схеме, допуская применение общих вычислительных коцепций. Моделирование проводится в два этапа.

На первым этапе вычисляется набор спектральных пиков, включая их положения, амплитуды и ширины, используя заданный спин гамильтониан и экспериментальные параметры. Одним из усовершенствований на этом этапе является новый адаптивный метод для вычисления значений резонансных полей в пространстве спиновых состояний. Получены новые общие выражения для квантово-механических вычислений пиков импульсного ЭПР в частотной области. Развит общий алгоритм, применимый ко всем импульсным последовательностям. Набор спектральных пиков, определенных либо как функция магнитного поля (стандартный ЭПР и другие методы исползующие протяжку магнитного поля) либо как функция частоты (все другие ЭПР эксперименты), может быть расширен за счет интерполяции. Введен новый пороговый метод для импульсного ЭПР, который выделяет и вычисляет только те резонансные пики, которые дают значительный вклад в спектр.

На втором этапе набор спектральных пиков преобразуется в спектр, сравнимый с экспериментальным. Выбор метода преобразования зависит от вида эксперимента. В данной работе представлен новый общий алгоритм для преобразования списка пиков в сигнал во временной области. Это значительно уменьшает как погрешности, так и время, необходимое для моделирования спектров импульсного ЭПР.

Другие усовершенствования включают переоценку наиболее часто встречающихся в литературе ориентационных сеток, используемых для моделирования спектров ЭПР и ЯМР в неупорядоченных системах. Впервые

вычислены общие корректные весовые множители. Введена новая, в высшей степени однородная сетка октаэдральной симметрии. Новым подходом является также введение адаптивних сеток, которые позволяют адаптировать разрешение ориентационной сетки к поведению резонансных функций и вычислять только те ориентации, влад которых в конечный спектр значителен. Этот новый метод имеет существенные преимущества при моделировании ДЭЯР и ЭПР спектров имеющих сильную угловую зависимость.

Synopsis

In solid-state EPR, computer-based numerical simulations are mandatory to reliably interpret experimental spectra of disordered systems (powders, glasses, frozen solutions) and to obtain information on the electronic structure of the measured paramagnetic substances. This PhD thesis is concerned with all principles underlying such simulations, improving theory and algorithms on many crucial points. The improvements result in better performance and extended applicability of the simulations. *Simulations*

In this work, simulations of cw EPR, ENDOR and pulse EPR spectra of disordered systems are dealt with under one unifying scheme, allowing the application of rather general computational concepts. All simulations proceed in two steps. *Two steps*

The first step starts from the spin Hamiltonian and the experimental parameters and computes a list of spectral peaks with their positions, amplitudes and line widths. One improvement for this step is a new adaptive method for computing cw EPR resonance fields in state space. For the quantum-mechanical computations of pulse EPR peaks new general expressions operating in frequency domain have been derived. A generic algorithm applicable to all pulse sequences has been developed. The list of spectral peaks, defined either as a function of magnetic field (cw EPR and other field scans) or frequency (all other EPR experiments), can be enlarged interpolatively. For pulse EPR a new thresholding method is introduced, which selects and actually computes only peaks significantly contributing to the spectrum. *(1) Peak list computation*

In the second step the list of spectral peaks is converted to a spectrum comparable to the experimental one. The choice of method depends on the nature of the experiment. In this work a new general algorithm for converting a peak list to a time-domain signal is presented. It greatly reduced both error and time consumption of pulse EPR simulations. *(2) Spectrum construction*

Other improvements include a re-evaluation of most published orientational grids used in EPR and NMR simulations of disordered systems. For the first time, general correct weighting factors have been computed. A new highly homogeneous grid with octahedral symmetry is introduced. Adaptive meshes are presented as a new and promising approach. They allow to adapt the resolution of the orientational grid to the behaviour of the resonance functions and to compute only orientations relevant to the final spectrum. This new method is very advantageous for the simulation of strongly orientation-selective ENDOR and pulse EPR spectra. *Grids*

Preface

In addition to articles published in scientific journals, there are two purposes of a separately written PhD thesis. First, it collects all the new results—published piecewise—and puts them into a consistent framework, as far as that is possible. Second, by including material which is relevant but not new, it collects insight gained during the work, and helps the reader find his way across the fragmented world of publications on the topic.

This work is not entirely written in formal language. A large fraction of the text might be in line with the strict standards of scientific publishing, but some concepts are treated in a more sloppy way. They have to be taken *con alcuna licenza*. If more concise formulations of the content are sought, I recommend reading the cited publications. When writing the following pages, it was relieving not having to observe strictly the dry code of scientific text-casting. Still, given the subject, this text cannot possibly be considered elegant prose.

Not only the form, but also the content and the emphasis of this thesis differ from a scientific publication. A beginning PhD student should be able to read this PhD thesis with little prior knowledge on computational EPR and to learn all that is needed for successfully simulating EPR spectra. Details about spectral simulations are scattered in the literature, so this collective overview can be very handy. I hope the work comes up to its premises and proves useful. Simulation of magnetic resonance spectra in powders is the province of a few specialists, but this work should address a larger audience.

This booklet puts forward a concise description how to numerically compute solid-state EPR, ENDOR and pulse EPR spectra of disordered systems from spin Hamiltonian parameters. After setting the scene by introducing the field of computational EPR and explaining in some detail the core concept of the spin Hamiltonian in Chapter 1, Chapter 2 collects old and new methods for the computation of peak positions and amplitudes for all common EPR experiments, including cw EPR, ENDOR and pulse EPR. Chapter 3 contains a lot of new material and explains how a set of peaks characterised by spectral positions, amplitudes and widths is converted to a spectrum comparable to that obtained experimentally. In Chapter 4, orientational distributions are discussed and analysed in unprecedented detail. A new orientational grid is presented, and the concept of adaptive meshes is introduced. Such meshes are state of the art in numerical electro- or hydrodynamics for the solution of differential equations in 3D space. This PhD thesis applies the concept to EPR and shows its clear advantages.

There remains, however, a lot to be done. Pulse EPR simulation techniques are still far from being fast and accurate enough to allow spectral fitting. In ESEEM,

amplitudes of simulated spectral peaks often are not close to those measured, even when peak positions and shapes match. A systematic comparison of experimental data to simulated spectra combined with careful analysis to identify the shortcomings of the current theory has still to be done. There is much latitude in improvement of the adaptive mesh methods proposed in this work.

EasySpin   Most of the theoretical and algorithmical concepts developed in this PhD thesis have been tested and implemented in the program package EasySpin, a collection of functions for Matlab, a numerical computation environment. Besides spectral simulation functions, functionality for making basic spin physical computations and for spectral analysis is included. EasySpin is freely available[1] and currently used worldwide in established EPR labs. It is briefly described in Chapter 5.

Some other simulation software packages are available[2], but their scope is much more limited than EasySpin. The only commercial undertake similar to EasySpin is XSophe, a simulation program covering cw EPR only. It has been developed by Bruker Biospin GmbH (Germany) together with the group of Graeme Hanson at the University of Queensland (Australia) [Gri99].

Internet   Nowadays scientific research is unimaginable without the use of the internet. It gives the critical and screening user access to invaluable resources, although many times one fishes in superficial, incomplete or wrong information. But people, databases, library catalogues, usenet forums, online book shops and a host of other resources collected through the Internet foster interactive and interdisciplinary thinking in an unprecedented way.

Thanks   In this place I would like very much to thank all those who have patiently and efficiently accompanied my work. Above all I wish to thank my supervisor Arthur Schweiger, who made it possible for me to carry out research in the field of computational EPR. I am also indebted to Sabine Van Doorslaer, now at the University of Antwerp, for her numerous and valuable hints and encouraging comments. I am grateful also to all the other members in my research group[3] who have contributed very much to create a pleasant working atmosphere. Last but not least I wish to express special thanks to Daniella Goldfarb for her hospitality and help during my stay at the Weizmann Institute of Science.

---

[1] http://www.esr.ethz.ch

[2] A partial list is: EPR-NMR (John Weil and Michael Mombourquette, University of Saskatchewan, Canada), Igor pro (John Boswell, Oregon Health & Science University, USA), GENDOR (Brian M. Hoffman, Northwestern University, IL, USA), Simfonia (Bruker, Germany), MSPEN/MSGRA (Jürgen Hüttermann, Universität des Saarlandes, Germany), QPOW (Mark J. Nilges, University Illinois at Urbana-Champain, IL, USA), MAGRES (Ed J. Reijerse, University of Nijmegen, Netherlands), SIM/SIMSPC (Høgni Weihe, University of Copenhagen), tryscore (Daniella Goldfarb, Weizmann Institute of Science, Israel). There are many programs from earlier times in the EPR Software database at http://epr.niehs.nih.gov/software.html

[3] Carlos Calle, Cinzia Finazzo, Jeff Harmer, George Mitrikas, Alex Angerhofer, Moritz Kälin, Matvey Fedin, Igor Gromov, Anna Ferretti, Boris Epel, Rafail Rakhmatoullin, Inés García Rubio, Lorenz Liesum, Rüdiger Eichel, Josef Granwehr, Zoltan Mádi. Walter Lämmler, Barbara Feurer, Jörg Forrer, Willi Groth, Irène Müller.

Contents

1 Introduction

> New in this chapter:
>
> ▷ A general two-step scheme for the computation of all EPR spectra

In this introductory chapter we give a general overview of computational EPR[1] and its two sub-disciplines, structural and spectral simulations. We show that spectral simulations in EPR can be generally divided into two equally important steps linked by the peak list, a concept central to this entire thesis. Then we present the core physical model behind all EPR spectra, the spin system, and its associated mathematical realisation, the spin Hamiltonian. This model depends on a host of magnetic parameters which we shall list and describe shortly. In reality, any parameter will not have a single value, but a discrete or continuous distribution. We discuss these distributions, with special emphasis on the orientational distribution giving rise to powder spectra.

Outline

1.1 Computational EPR

In experimental EPR, spectra of paramagnetic molecules or other paramagnetic centres are measured and used to derive structural information. This structural information ranges from the test whether a certain atom is present and close to the unpaired electron to detailed angular and distance information between atoms. Sometimes the electron density distribution around the paramagnetic centre can be mapped out.

Structural information

The interpretation of an EPR spectrum can be anything between trivial and impossible, depending on the complexity of the measured molecular structure, the complexity of the experiment and the resolution and S/N ratio of the spectrum. The quantum-mechanical theory underlying EPR is reasonably well understood, and many simple spectra can be analysed by means of compact analytical formulas derived from the basic equations [Sch01]. For more complex systems, which are the rule rather than the exception, these formulas are too approximate or even not valid anymore. In such cases, numerical simulations are the only feasible way

Spectral interpretation

---

[1] In this thesis, EPR is used as a collective term for cw (continuous wave) EPR (electron paramagnetic resonance), ENDOR (electron-nuclear double resonance) and pulse EPR methods such as ESEEM (electron spin echo envelope modulation). If specific EPR experiments or spectra are meant, they are referred to explicitly.

PSfrag replacements

(2) spectral simulation   (1) structural simulation

| spectrum | | magnetic parameters | | geometric structure |
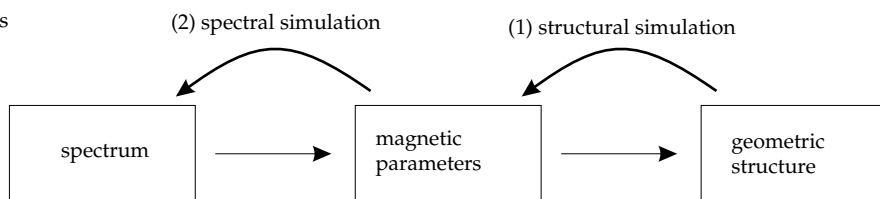
Figure 1.1: Spectral analysis (normal arrows) and computational synthesis (bold arrows) of an EPR spectrum.

of extracting magnetic parameters and through them structural information from EPR spectra.

Analysis vs. synthesis

Although in spectral analysis one starts from a measured spectrum, extracts the magnetic parameters and then deduces structural information from them, a numerical approach has to proceed in the opposite direction (see Figure 1.1). Magnetic parameters can only be computed from a molecular structure, and not vice versa. Similarly, it is only possible to generally compute spectra from parameters and not the other way round.

Fitting

Eventually, once methods in computational EPR are advanced enough, they might operate along the analysis way, taking an EPR spectrum and deriving their magnetic parameters by means of optimisation routines. These tasks are, however, extremely difficult, since even an almost noise-free spectrum can be fitted well with many different sets of magnetic parameters. Many times it is almost impossible to find or even define a global minimum in parameter space. Most EPR spectra are not structured enough to allow reliable extraction of all magnetic parameters. The only way out of this would be a simultaneous fit of spectra obtained at different frequencies or/and with different experimental methods. For this multi-spectral fitting, however, the simulation of all sorts of EPR spectra has to be general, robust and quick, which is currently not the case for pulse EPR spectra.

Computers

Computers have already been employed for simulations in EPR for decades (see e.g. [Mac69, Tay75, Pil99]). Most of the programs written implemented analytical formulas which were too complicated to evaluate manually. It is only for a short time that the basic equations and not special solutions are being implemented and that a cw EPR (or ENDOR or pulse EPR) spectrum can be derived from the geometric structure of the paramagnetic centre, at least in principle.

Two tasks

The computational connection between structure and spectrum consists of two different tasks. One is to compute magnetic parameters from a given molecular structure. The structure itself could be arrived at either experimentally or computationally. The second task consists of computing the EPR spectrum from the magnetic parameter set (see Figure 1.1).

PSfrag replacements

| spin system | $\longrightarrow$ | peak list | $\longrightarrow$ | spectrum |
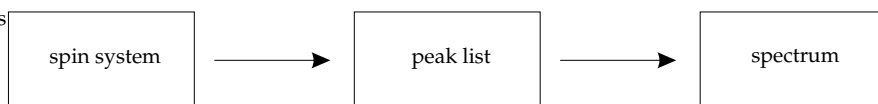
Figure 1.2: General schematics for simulation in structural EPR.

1.1.1 Quantum chemistry

The first step in computing the EPR spectrum from a molecular structure is the computation of a set of magnetic parameters which more directly determine the shape of any EPR spectrum. This falls into the realm of quantum chemistry. Using methods of various degrees of sophistication (semi-empirical methods, Hartree-Fock methods, density functional theory, coupled cluster) [Jen99], state energies and many other observables can be computed from a simple geometric model of the molecular structure giving nuclear isotopes and their coordinates. These uniquely determine the molecular Hamiltonian operator. The solution of the associated Schrödinger equation gives wave functions (or an electron density) which unambiguously determine all measurable properties of the system, including all possible magnetic parameters.

Quantum chemistry

The computation of magnetic parameters (see next section) from a molecular structure is a relatively new field in quantum chemistry. Most promising are methods based on DFT (density functional theory). In NMR they are already applied with great success, whereas in EPR their accuracy varies strongly. They are reasonably accurate for organic radicals. For paramagnetic molecules containing transition metal ions, however, results are currently not reliable due to deficiencies in the theory and the fact that the obtained wave functions are not accurate enough. None of the available methods gives magnetic parameters consistent with experiments [Mun99, Kau02b]. We will comment on the reliability of numerical values when discussing the various magnetic parameters in the next section.

EPR parameters

1.1.2 Spectral simulations

The second step in computing the EPR spectrum from a molecular structure is the computation of the EPR spectrum from the magnetic parameters of the paramagnetic centre (see Figure 1.1). The parameters can be computationally derived, published and known values, or just educated guesses from measured spectra. This second step is the subject of the present PhD thesis.

EPR spectrum

In a very general picture, the numerical computation of a powder spectrum in EPR can be subdivided into two steps, quite independent of the nature of the experiment (cw EPR, ENDOR or pulse EPR). This is illustrated in Figure 1.2.

Spin system → peaks

In the first step, a list of peaks is computed. Each peak p is represented by its

Peak list

position y_p (either a resonance field or a resonance frequency), its amplitude A_p and its line width Γ_p.

$$\text{peak } p: \qquad (y_p, A_p, \Gamma_p) \tag{1.1}$$

Under many circumstances, peaks can be assumed to have identical line widths Γ, so that the peak list is simpler

$$\text{peak } p: \qquad (y_p, A_p) \tag{1.2}$$

If broadening is absent ($\Gamma = 0$), the resulting theoretical spectrum is called a stick spectrum[1].

This peak list contains all physical information about the spectrum, although not in the final form. The details of the computation of the peak list depend on the kind of experiment performed. In all cases the computation starts from the spin Hamiltonian and a set of experimental parameters and uses quantum-mechanical equations to arrive at the peak list.

There are a host of possibilities to compute the peak data. They can be obtained ab initio from full analytical formulas (exact or perturbational approximations) or from a complete numerical treatment. Peaks can also be obtained from other peaks by interpolation or extrapolation. Methods for computing peaks for most EPR experiments are dealt with in Chapter 2.

Peaks → spectrum

The second step takes the peak list and converts it into the final spectrum. This is a very general procedure, which does not depend on the details of the experiment or the spin Hamiltonian. It does, however, depend on the mode of measurement in the experiment. Spectra are either acquired directly in the spectral domain (cw EPR, ENDOR) or in the inverse (usually time) domain. Only these differences have to be taken into account. Appropriate methods are discussed in Chapter 3.

The peak list is the central concept in EPR spectral simulations. Constructing it is a major quantum-mechanical undertaking, whereas converting it to a spectrum is a purely geometric endeavour.

1.2 Interactions

Geometric reach

The EPR spectra of a certain molecule depend on its isotope composition, its geometric structure (both static and dynamic) and its surroundings. But not all geometric parameters are equally relevant to explain EPR spectra. The further away from the paramagnetic centre atoms, bonds and other spins are, the smaller is their impact on EPR spectra. Interactions observable in EPR are locally confined to the paramagnetic centre and have a typical horizon of about 0.5 nm around an unpaired electron. Interactions between several unpaired electrons can be measured by EPR up to distances of more than 5 nm.

---

[1] Note that in spectra acquired in time domain there is broadening even in this case due to the nature of the measurement process.
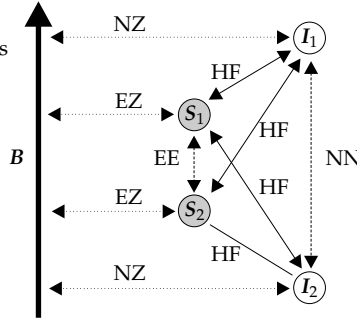
Figure 1.3: A network of two electron and two nuclear magnetic moments in an external magnetic field *B* and the various magnetic interactions.

All relevant influences are summarised and parameterised in a phenomenological model called the spin Hamiltonian which describes the behaviour of the set of states observable by EPR. These states are sub-states of the electronic ground state and are usually due to electronic and nuclear spins interacting with each other. The spin Hamiltonian is not a full physical model, its purpose is only to accurately describe and parameterise "interactions" having influence on the magnetic resonance spectra. It describes the EPR behaviour of the systems without bothering about the physical details[1]. — Spin Hamiltonian

The general spin Hamiltonian for *n* electrons and *m* nuclei with non-zero spins

$$\mathcal{H} = \sum_{i \neq j} \mathcal{H}_{\text{EE}}(\boldsymbol{S}_i, \boldsymbol{S}_j) + \sum_{i,k} \mathcal{H}_{\text{HF}}(\boldsymbol{S}_i, \boldsymbol{I}_k) + \sum_{k \neq l} \mathcal{H}_{\text{NN}}(\boldsymbol{I}_k, \boldsymbol{I}_l)$$
$$+ \sum_i \left[\mathcal{H}_{\text{EZ}}(\boldsymbol{B}, \boldsymbol{S}_i) + \mathcal{H}_{\text{ZF}}(\boldsymbol{S}_i) \right] + \sum_k \left[\mathcal{H}_{\text{NZ}}(\boldsymbol{B}, \boldsymbol{I}_k) + \mathcal{H}_{\text{NQ}}(\boldsymbol{I}_k) \right] \tag{1.3}$$

is a sum over interactions between the magnetic momenta of the electron spins *S*, the nuclear spins *I* and the external magnetic field *B* (see schematic representation in Figure 1.3). *S*, *I* and *B* are 3-element column vectors. Whereas their components are real scalars for *B*, they are operator matrices for *S* and *I*. Details of these spin operators are relegated to Appendix A.

$\mathcal{H}$ and its component Hamiltonians have units of energy. In magnetic resonance it is more convenient to use them in frequency units — Units

$$H = \mathcal{H}/h \tag{1.4}$$

with the Planck constant *h*. In pulse EPR, *angular* frequency units are often used. In this text we will use *H* in *normal* frequency units throughout except in the sections on pulse EPR in Chapter 2, where we use angular units.

---

[1] For a lucid and very comprehensive exposition of the concept of spin Hamiltonian in EPR, see [Rud01]

In the following we shortly present each interaction and its relation to structural features. The main purpose is to provide all formulas needed in spectral simulations. For a more complete theoretical treatment of the interactions, see [Abr86, Poo87, Pil90, Wei94].

EZ Electron Zeeman interaction

The linear interaction of the paramagnetic centre with the external magnetic field

$$\mathcal{H}_{\mathrm{EZ}}(\boldsymbol{B}, \boldsymbol{S}) = h H_{\mathrm{EZ}}(\boldsymbol{B}, \boldsymbol{S}) = -\boldsymbol{B}^{\mathrm{T}} \boldsymbol{\mu}_{\mathrm{e}} = \mu_{\mathrm{B}} \boldsymbol{B}^{\mathrm{T}} \boldsymbol{g} \boldsymbol{S} \ . \tag{1.5}$$

is parameterised by the $\boldsymbol{g}$ matrix. $\mu_{\mathrm{B}} = 9.27401 \cdot 10^{-24} \, \mathrm{J\,T^{-1}}$ is the Bohr magneton. The product $\boldsymbol{\mu}_{\mathrm{e}} = -\mu_{\mathrm{B}} \boldsymbol{g} \boldsymbol{S}$ represents the magnetic moment due to the combination of spin and orbital angular momentum, which in general is different from the pure spin angular momentum both in direction and magnitude. Therefore, $\mathcal{H}_{\mathrm{EZ}}$ is an effective Hamiltonian[1].

For a free electron, the Zeeman interaction is isotropic with scalar $g = g_{\mathrm{e}} = 2.0023193$. For any electron confined to an orbital in a molecular structure, it is anisotropic, and $\boldsymbol{g}$ is a 3×3 matrix deviating from g_{e}. For organic compounds the deviation is small, for transition metal complexes it can be large. The deviation depends on the nature and symmetry of the spin orbital(s) of the unpaired electron(s) and on the strength of spin-orbit coupling. This depends on the amount of mixing between the EPR-observable electronic ground state and any low-lying excited state. The lower the excited state, the bigger the influence on $\boldsymbol{g}$.

g frame   In its eigenframe representation, $\boldsymbol{g}$ is a diagonal matrix

$$\boldsymbol{g} = \begin{pmatrix} g_1 & 0 & 0 \\ 0 & g_2 & 0 \\ 0 & 0 & g_3 \end{pmatrix} = g_{\mathrm{e}} \mathbb{1}_3 + \Delta \boldsymbol{g} = g_{\mathrm{e}} \mathbb{1}_3 + \begin{pmatrix} \Delta g_1 & 0 & 0 \\ 0 & \Delta g_2 & 0 \\ 0 & 0 & \Delta g_3 \end{pmatrix} \ , \tag{1.6}$$

where g_1, g_2 and g_3 are the values along the three principal axes of $\boldsymbol{g}$. These are orthonormal and are commonly used to define a molecule-fixed reference coordinate system (see Section 2.1.1). Orientations of other interaction tensors and matrices are specified relative to this $\boldsymbol{g}$ frame.

Numerical   The computation of $\boldsymbol{g}$ matrices from molecular orbital data obtained by quan-
computation   tum chemical methods has attracted much interest in recent years (see [Kau02b] and references therein). The computation of $\Delta \boldsymbol{g}$ is particularly demanding, since $\Delta \boldsymbol{g}$ is determined by purely relativistic effects, mainly spin-orbit coupling. Methods differ by the number of terms they include and the level of their treatment (perturbational or exact). The basis sets employed can have a large impact on the results. The best agreement with experiment is found for $\boldsymbol{g}$ matrices of organic and other first-row radicals. Computed values for $\Delta \boldsymbol{g}$ usually deviate not more

---

[1] Similarly, $\boldsymbol{S}$ is an *effective* spin. A related concept is the *fictitious* spin. See [Rud01] for the differences between these entities.

than 50% from experimental ones, in some cases they are accurate to within a few percent [Kau02a]. For transition metal ions, the situation is much worse. Values can deviate by up to a factor of 10 [Kau02b]. Occasionally, even the sign is wrong.

HF Hyperfine interaction

The hyperfine term describes the magnetic interaction of an electronic spin S with a nuclear spin I by means of a 3×3 matrix A

$$H_{\text{HF}}(S, I) = \mathcal{H}_{\text{HF}}(S, I)/h = S^{\text{T}} A I = S^{\text{T}} (a_{\text{iso}} \mathbb{1}_3 + T) I . \tag{1.7}$$

The interaction consists of two components, a dipolar and an isotropic one.

The dipolar interaction (described by the traceless matrix T) acts through space directly between the nucleus and the electron (for formulas see [Sch01]). As the unpaired electron is delocalised in its orbital (single occupied molecular orbital, SOMO), the dipolar interaction depends on the integral over the SOMO. For orbitals with an inversion centre at the nucleus, this interaction vanishes. However, by virtue of the unpaired electron's different interaction with electrons of different spins, it spin-polarises other doubly occupied orbitals. These polarised orbitals will also interact with the nucleus. For 3d complexes, there is often significant spin density in the 2p and 3p orbitals [Mun00]. *(margin: Dipolar interaction)*

The isotropic interaction (a_{iso}) is due to the finite probability of finding the electron at the site of the nucleus. Its value is proportional to the spin density at the nucleus $\rho_{\text{n}}^{\alpha-\beta} = |\Phi^{\alpha}(r_{\text{n}})|^2 - |\Phi^{\beta}(r_{\text{n}})|^2$ *(margin: Isotropic interaction)*

$$a_{\text{iso}} = \frac{1}{3h} \mu_0 \mu_{\text{B}} \mu_{\text{n}} g_{\text{e}} g_{\text{n}} \langle S_z \rangle^{-1} \rho_{\text{n}}^{\alpha-\beta} . \tag{1.8}$$

This "Fermi contact" interaction depends again on the symmetry of any spin-polarised orbitals. If an orbital has a node at the site of the nucleus, any electron residing in it will have no isotropic interaction with the nucleus. Still, other orbitals centred on the same nucleus might become spin-polarised, transferring spin density from the SOMO to the nucleus. In 3d complexes, this usually proceeds via 2s and 3s orbitals [Mun00].

Generally the g and A matrices of a paramagnetic centre are not aligned. Since the g eigenframe is usually the molecular reference frame (see Section 2.1.1), the orientation of the A matrix is specified relative to the g frame. If A is in its eigenframe, then the g-frame representation A_g is *(margin: Relative orientation)*

$$A_g = R(\alpha_A, \beta_A, \gamma_A) A R(\alpha_A, \beta_A, \gamma_A)^{\text{T}} \tag{1.9}$$

with the Euler rotation angles α_A, β_A and γ_A (see Appendix C). When using published data, the exact definition of the rotation angles has to be carefully checked.

Spin polarisation cannot be accurately modelled with quantum chemical methods, therefore computed hyperfine interaction matrices often deviate strongly from experimental ones. The situation is worst for transition metal nuclei with an unpaired electron in an orbital centred at that nucleus [Mun99]. *(margin: Numerical computation)*

NZ Nuclear Zeeman interaction

The interaction of a nuclear magnetic moment with the external static field

$$\mathcal{H}_{NZ}(\boldsymbol{B}, \boldsymbol{I}) = hH_{NZ}(\boldsymbol{B}, \boldsymbol{I}) = -\boldsymbol{B}^{T}\boldsymbol{\mu}_{n} = -\mu_{N}g_{n}\boldsymbol{B}^{T}\boldsymbol{I} \qquad (1.10)$$

is analogous to that of the electron, with the nuclear spin[1] vector $\boldsymbol{I}$, the nuclear g factor g_n and the nuclear magneton $\mu_N = 5.0507866 \cdot 10^{-27}\,\text{J}\,\text{T}^{-1}$.

Sign of g_e, g_n The sign convention of the g factor in EPR is inconsistent with the convention for nuclear g_n values [Bro00]. According to the definition

$$\boldsymbol{\mu}_{n} = \mu_{N}g_{n}\boldsymbol{I} \qquad (1.11)$$

g_n is positive when the magnetic moment $\boldsymbol{\mu}_n$ and the angular momentum $\boldsymbol{I}$ are parallel, and negative if they are antiparallel. For the electron the sign is different

$$\boldsymbol{\mu}_{e} = -\mu_{B}g\boldsymbol{S} \ , \qquad (1.12)$$

meaning that g is positive when $\boldsymbol{\mu}_e$ and $\boldsymbol{I}$ are *anti*parallel. This inconsistency is regrettable, but we bow to tradition and define the sign of both nuclear and electron g factors in the conventional way.

    g_n is a constant depending only on the nuclear isotope. g_n can be positive or negative, its magnitude ranges from 0.01175 for ^{68}Ga to 7.3 for ^{97}Nb. Chemical shifts (deviations from g_n) and chemical shift anisotropies measurable by NMR are of no relevance in EPR, since they are by orders of magnitude too small to be resolvable. Theoretically computed values for chemical shifts are quite accurate, at least in diamagnetic compounds [Sch98].

NQ Nuclear quadrupole interaction

Quadrupole moment   The nuclear angular momentum direction is linked to the actual shape of the nucleus, that is, to the axis of symmetry of its charge distribution. When a nucleus has a spin $I \geq 1$, it has an electric quadrupole moment, which causes it to align along the electric field gradient (EFG) in the surrounding space. In paramagnetic centres, such electric fields are generated by the nuclei and the electron distribution in the immediate neighbourhood of the nucleus.

Interaction term   The energy of alignment of a nuclear spin in the total electric field is described by the nuclear quadruple interaction term

$$\mathcal{H}_{NQ}(\boldsymbol{I})/h = H_{NQ}(\boldsymbol{I}) = \boldsymbol{I}^{T}\boldsymbol{P}\boldsymbol{I} = \frac{e^{2}qQ}{4I(2I-1)h}\left[3I_{z}^{2} - \boldsymbol{I}^{T}\boldsymbol{I} + \eta\left(I_{x}^{2} - I_{y}^{2}\right)\right], \quad (1.13)$$

where the nuclear quadruple tensor is

$$\boldsymbol{P} = \frac{e^{2}qQ}{4I(2I-1)h}\begin{pmatrix} -(1-\eta) & 0 & 0 \\ 0 & -(1+\eta) & 0 \\ 0 & 0 & 2 \end{pmatrix} \qquad (1.14)$$

---

[1] $\boldsymbol{I}$ is *not* the pure spin, but the total angular momentum of the nucleus, consisting of orbital and spin momenta of the particles in the nucleus.

with the magnitude eq of the EFG at the nucleus, its quadrupole moment Q and the elementary charge e. η is the asymmetry parameter. Note that NQ is an electric, not a magnetic interaction, in contrast to all other interactions of Eq. (1.3). In the literature, usually the values of the prefactor in Eq. (1.14) and η are given. P is transformed from its eigenframe to the g frame in analogy to Eq. (1.9).

P contains through its magnitude and its orientation a wealth of information on the local surroundings of nuclei in paramagnetic centres. Although EFGs of small atoms in diamagnetic molecules can be computed quite accurately (see e.g. [Bai00]), there have been only a few studies involving paramagnetic centres [Sta02]. *Numerical computation*

NN Nucleus-nucleus interaction

Nuclear spins can couple either directly through space (dipole-dipole interaction) or by means of the electron orbitals surrounding both of them (J coupling). Both interactions are anisotropic. The total interaction is described by

$$\mathcal{H}_{\mathrm{NN}}(I_1, I_2)/h = H_{\mathrm{NN}}(I_1, I_2) = I_1^{\mathrm{T}} J I_2 \ . \tag{1.15}$$

This term is not larger than $100\,\mathrm{kHz}$ in magnitude and is usually neglected in EPR, since it cannot be resolved by most EPR experiments. It contributes to inhomogeneous broadening, though.

ZF Electron zero field splitting

The fact that the total magnetic moment is due to the sum of spin and orbital angular momenta but described only by the spin operator S leads to the appearance of a term of the form

$$\mathcal{H}_{\mathrm{ZF}}(S)/h = H_{\mathrm{ZF}}(S) = S^{\mathrm{T}} D S = D\left[S_z^2 - \frac{1}{3}S(S+1)\right] + E(S_x^2 - S_y^2) \tag{1.16}$$

with

$$D = \begin{pmatrix} D_x & 0 & 0 \\ 0 & D_y & 0 \\ 0 & 0 & D_z \end{pmatrix} = \begin{pmatrix} -\frac{1}{3}D + E & 0 & 0 \\ 0 & -\frac{1}{3}D - E & 0 \\ 0 & 0 & \frac{2}{3}D \end{pmatrix} \ . \tag{1.17}$$

Usually the axes of D are defined such that $|D_x| \leq |D_y| \leq |D_z|$. The ZF term is formally analogous to the NQ term. Note that it is customary to use the letter D to indicate both the interaction matrix and one of its two scalar parameter.

A term of the same form appears if two or more electrons interact strongly and are represented by a single spin $S > 1/2$ in a coupled representation, e. g. $S = 5/2$ for high-spin Fe^{3+} ions. D is transformed from its eigenframe to the g frame in analogy to Eq. (1.9).

In a very general way the zero field splitting can additionally contain terms with S^4 and S^6. These are important for high-spin transition and rare earth ions. *S^4, S^6*

9

They are summarised in Appendix A on p. 121. For a detailed discussion, see [Rud87].

Numerical computation

There are very few studies with theoretically computed values for D and E, although the theory was developed some years ago [Nee98]. The reliability of numerical D values has not yet been studied in detail.

EE Electron-electron interaction

If two electrons interact weakly, they are usually represented by separate spins in the uncoupled representation. There are two mechanisms by which one electron can influence the other. One is, as in the case of two nuclei or one nucleus and one electron, the through-space dipolar interaction. The other is the Heisenberg exchange interaction. Collectively, the interactions are parameterised in the spin Hamiltonian by the term

$$\mathcal{H}_{\mathrm{EE}}(S_1, S_2)/h = H_{\mathrm{EE}}(S_1, S_2) = S_1^{\mathrm{T}} X S_2 \ , \tag{1.18}$$

where X is in general not traceless. For details refer to [Ben90].

1.3 Distributions

Parameter space

The spin Hamiltonian of Eq. (1.3) depends on a set of parameters. This set can be visualised as a single point in a multi-dimensional parameter space $\mathcal{P}$, a space where each dimension represents the possible values of one parameter.

Above absolute zero, molecules are dynamic species and vibrate. Since spin Hamiltonian parameters depend to some degree on the geometry of the paramagnetic centre, all parameters are dynamical and change with time.

Dynamical regimes

In solid-state EPR we usually can neglect these dynamic changes, since most measurements are made at temperatures where structural fluctuations are minimal. Indeed, most pulse EPR experiments are impossible when centres are completely mobile. When centres are fully mobile, effective values of parameters like g and A assume the average of their principal values and become isotropic. Between the rigid limit and the full motional freedom, there is a region called the slow motional regime. In the associated temperature ranges interaction tensors and matrices are only partially averaged out. EPR spectra differ from those in the rigid limit and contain valuable information [Sch89].

Rigid limit

In this thesis, we restrict ourselves to the rigid limit, which assumes that spin Hamiltonian parameters are independent of time or at least change on a timescale much larger than the experimental one. Macroscopically, the rigid limit is valid in frozen solutions, crystals, powders and glasses at low temperatures.

Distributed systems

In the rigid limit, one paramagnetic centre corresponds to one point in $\mathcal{P}$. Usual samples contain more than 10^{10} centres, each one with a slightly different structural surrounding. As a consequence of these static structural variations,

each centre corresponds to a different point in $\mathcal{P}$, i.e. each spin Hamiltonian parameter may vary from one centre to the other, resulting in an overall distribution rather than a single point. The result is a so-called inhomogeneous broadening of the spectrum. In contrast, homogeneous (life-time) broadening is present even when all centres have exactly the same spin Hamiltonian.

A distinction can be made between the distribution in the orientation of the paramagnetic centres and structural distributions resulting in distributions of all other spin Hamiltonian parameters. There are discrete and continuous orientational distributions. For a single crystal, paramagnetic centres are aligned along one of a limited number of symmetry-related orientations with respect to the crystal system. Anisotropic parameters will assume a small set of different values associated with these orientations. In powders the orientational distribution is not discrete, but continuous and uniform. The paramagnetic centres assume all possible orientations Ω in space. Powders are often referred to as disordered systems.

Orientations

Structural variations (also called strains [Hag85b]) in the immediate surroundings of a paramagnetic centre cause variations in spin Hamiltonian parameters, mainly in g, A and D. These distributions are always continuous. The explicit form of a distribution in one of these parameters depends on the nature of the structural strains. Since all spin Hamiltonian parameters depend on structural properties, they are correlated and cannot change independently of each other. Often distributions are random, so that they can be approximated by Gaussians (see Appendix B). If a distribution is small in magnitude, it is usually small in effect and can be incorporated in a linear approximation into the line width (see Section 2.3). For clearly not random, large, or correlated parameter distributions, the simulation of the associated spectra must include an explicit integration over the distribution.

Strains

1.4 Powder spectra

From the experimental side, a powder is a collection of a very large number of paramagnetic centres randomly oriented in space, so that the resulting orientational distribution is uniform, that is, each orientation has the same probability of occurring. Only in the infinite limit, however, this distribution is uniform. Theoretical considerations are always based on the infinite limit. In general, the resonance position $y_{\text{res}}(\Omega)$ (field or frequency), the intensity $A(\Omega)$ and the line width $\Gamma(\Omega)$ depend on the relative orientation Ω between molecule and laboratory frame.

The powder spectrum is an integral function[1] of field or frequency y. The kernel of the integral function is the orientation-dependent single crystal spectrum,

Density of
states

---

[1] Note the subtle difference between an integral $F(x) = \int_c^x f(t)\,dt$ and an integral function $F(x) = \int f(x,t)\,dt$.

it is integrated[1] over all possible orientations of the paramagnetic centre

$$S(y) = \oint_{\Omega} A(\boldsymbol{\Omega}) f[y - y_{\text{res}}(\boldsymbol{\Omega}), \Gamma(\boldsymbol{\Omega})] \, d\boldsymbol{\Omega} \, . \tag{1.19}$$

If we neglect, for simplicity, the line width Γ, we obtain the stick spectrum

$$S(y) = \oint_{\Omega} A(\boldsymbol{\Omega}) \delta_{\text{D}}[y - y_{\text{res}}(\boldsymbol{\Omega})] \, d\boldsymbol{\Omega} \, , \tag{1.20}$$

with the Dirac delta function[2] δ_{D}. Eq. (1.20) shows that the stick spectrum is the total density of states along y for all orientations of the paramagnetic centre.

Surface integral   Using the Heaviside function defined by $dH(x)/dx = \delta_{\text{D}}(x)$, Eq. (1.20) can be rewritten

$$S(y) = \frac{d}{dy} \oint_{\Omega} A(\boldsymbol{\Omega}) H[y - y_{\text{res}}(\boldsymbol{\Omega})] \, d\boldsymbol{\Omega} \tag{1.21}$$

and as a consequence

$$S(y) = \frac{d}{dy} \oint_{y_{\text{res}}(\boldsymbol{\Omega}) \leq y} A(\boldsymbol{\Omega}) \, d\boldsymbol{\Omega} \, . \tag{1.22}$$

This means that the powder spectrum is a weighted surface integral over all orientations where y_{res} is smaller than the given y. For a given y, the *resonance surface* $y_{\text{res}}(\boldsymbol{\Omega})$ is divided into regions separated by borders at the contour lines $y_{\text{res}}(\boldsymbol{\Omega}) = y$. The integral describes how the weighted area of the regions with $y_{\text{res}} \leq y$ changes, when y (the border) is moved.

Line integral   A third way to look at Eq. (1.20) is the following. Transforming to natural coordinates where $\boldsymbol{n}$ is perpendicular to the contour lines and $\boldsymbol{s}$ parallel to them, we get

$$S(y) = \frac{d}{dy} \oint_{y_{\text{res}}(\boldsymbol{\Omega}) \leq y} A(\boldsymbol{\Omega}) \, d\boldsymbol{s} d\boldsymbol{n} = \frac{d}{dy} \oint_{y_{\text{res}}(\boldsymbol{\Omega}) \leq y} A(\boldsymbol{\Omega}) \, d\boldsymbol{s} \frac{dy}{|\nabla y_{\text{res}}(\boldsymbol{\Omega})|} \tag{1.23}$$

$$= \frac{d}{dy} \int_{-\infty}^{y} \oint_{y_{\text{res}}(\boldsymbol{\Omega}) = y} \frac{A(\boldsymbol{\Omega})}{|\nabla y_{\text{res}}(\boldsymbol{\Omega})|} \, d\boldsymbol{s} dy = \oint_{y_{\text{res}}(\boldsymbol{\Omega}) = y} \frac{A(\boldsymbol{\Omega})}{|\nabla y_{\text{res}}(\boldsymbol{\Omega})|} \, d\boldsymbol{s} \tag{1.24}$$

This is a line integral. The powder spectrum (or density of states) at y is the weighted line integral over the contour line $y_{\text{res}} = y$.

---

[1] There is some ambiguity in the terminology. Are disordered systems described by a powder *average* or by a powder *integral* of N centres? Viewed from the single centres, we are indeed *summing* up, but compared to a single crystal with the same number of centres, the powder is an orientational *average*. Both terms are sensible and are used without distinction.

[2] Note the difference between the Kronecker and Dirac delta functions $\delta(x)$ and $\delta_{\text{D}}(x)$. For $x \neq 0$, both are zero, whereas for $x = 0$ we have $\delta(0) = 1$ and $\delta_{\text{D}}(0) = \infty$.

2 Peaks

New in this chapter:

▷ Analytical formulas for energy and state derivatives

▷ A classification of methods for computing cw EPR resonance fields

▷ A new iterative and very robust method for doing so

▷ Frequency-domain expressions for the efficient simulation of arbitrary pulse EPR experiments

▷ Simulations of pulse EPR spectra in the lab frame

▷ Monotony-conserving interpolation methods applied to EPR

▷ Adaptive thresholding in FD pulse EPR computations

In this chapter we will present most ingredients necessary to compute peak positions and amplitudes (i.e. the peak list) for cw EPR, cw and pulse ENDOR and any conceivable pulse EPR experiment. In the first section, some basic formulas are collected. In two separate sections we treat cw EPR and ENDOR peaks. Most of the rest of the chapter is devoted to pulse EPR peaks. The last two sections deal with interpolation and thresholding. At the end we make some comments about performance issues.

Outline

2.1 Basics

Although Dirac introduced it first ad hoc into the relativistic Schrödinger equation, spin is a non-relativistic phenomenon. That was found[1] in 1967, but many textbooks and even monographs still erroneously present it as a relativistic particle property. Spin-orbit coupling *is* a relativistic phenomenon, though.

Spin

Particles with spin have non-zero magnetic moments, by which they interact. These interactions (see Chapter 1) are represented by $N \times N$ matrices and cause a splitting of the degenerate spin states $|u\rangle$ into N states. A state (ket) is represented by a normalised complex column vector of dimension $N \times 1$. Its conjugate transpose (bra) $\langle u| = |u\rangle^{\dagger}$ is a row vector. Mathematically, the N states span the state space, which is a Hilbert space of dimension N. A transition between two states $|u\rangle$ and $|v\rangle$ can be written either as an $N \times N$ matrix $|u\rangle\langle v|$ or as an $N^2 \times 1$

Hilbert spaces

---

[1] Lévy-Leblond [Lév67] has shown that the spin can be derived from symmetry properties of the non-relativistic Schrödinger equation.

vector $|u\rangle \otimes |v\rangle$, where $\otimes$ is the Kronecker tensor product as defined in Eq. (A.14) on p. 123. All transitions span another Hilbert space of dimension N^2. State space operators are vectors in this transition (Liouville) space, which are acted upon by superoperator matrices of dimension $N^2 \times N^2$.

Spin operators and their matrix representations are standard textbook fare and are summarised in Appendix A on p. 121. For a good textbook on general quantum mechanics, see [Sak85]. Liouville space is nicely treated in [Ern89].

2.1.1 Coordinate systems

External fields

The spin Hamiltonian depends on the orientation of the spin system in the laboratory frame, i.e. its relative orientation with respect to the external field $\boldsymbol{B} = \boldsymbol{B}_0 + \boldsymbol{B}_1(t) + \boldsymbol{B}_2(t)$, usually consisting of several components: $\boldsymbol{B}_0$ is the static magnetic field. $\boldsymbol{B}_1$ is the magnetic component of the incident microwave (mw) radiation. It is usually perpendicular to $\boldsymbol{B}_0$, but some experiments use $\boldsymbol{B}_1 \| \boldsymbol{B}_0$. In ENDOR experiments the magnetic component $\boldsymbol{B}_2$ of the additional radio frequency (rf) radiation is perpendicular to $\boldsymbol{B}_0$.

L and M frame

There are two frames used to describe the experimental setup. The laboratory frame L is defined with

$$z_\mathrm{L} \| \boldsymbol{B}_0 \qquad x_\mathrm{L} \| \boldsymbol{B}_1 \qquad y_\mathrm{L} = z_\mathrm{L} \times x_\mathrm{L} \ . \tag{2.1}$$

The molecular frame M is defined as coinciding with the principal axis system of the $\boldsymbol{g}$ matrix of the paramagnetic centre (or some other interaction matrix if $\boldsymbol{g}$ is isotropic). For axial $\boldsymbol{g}$ matrices, z_M is usually along $g_\|$, and x_M and y_M depend on some other molecular or spin physical direction. For orthorhombic $\boldsymbol{g}$ matrices, there are three possibilities for alignment of M with $\boldsymbol{g}$. L and M are related by three Euler angles ϕ, θ and χ, so that the L and M representations of a vector $\boldsymbol{v}$ are[1]

$$v_\mathrm{L} = \boldsymbol{R}(\phi, \theta, \chi) v_\mathrm{M} \quad \text{and} \quad v_\mathrm{M} = \boldsymbol{R}(-\chi, -\theta, -\phi) v_\mathrm{L} \tag{2.2}$$

(see Figure 2.1 and Appendix C).

M preferred

Of course, the spin Hamiltonian can be formulated in both frames

$$H_\mathrm{M} = F_\mathrm{M} + \boldsymbol{B}_\mathrm{M}^\mathrm{T} \boldsymbol{G}_\mathrm{M} \qquad H_\mathrm{L} = F_\mathrm{L} + \boldsymbol{B}_\mathrm{L}^\mathrm{T} \boldsymbol{G}_\mathrm{L} \ . \tag{2.3}$$

F is independent of the orientation of the external fields and contains all internal interactions (ZF, EE, HF, NN, NQ), but its representations in L and M are different, since it contains spin vectors $\boldsymbol{S}_\mathrm{L}$ or $\boldsymbol{S}_\mathrm{M}$. $\boldsymbol{G} = (G_\mathrm{x}, G_\mathrm{y}, G_\mathrm{z})^\mathrm{T}$ describes all Zeeman interactions (EZ, NZ and higher-order terms linear in the magnetic field). It is easier to use the M representation of all these operators, since then only $\boldsymbol{B}_\mathrm{M}$ changes if the spin system is physically rotated, whereas F_M and $\boldsymbol{G}_\mathrm{M}$ do not change. $\boldsymbol{B}_\mathrm{M}$ is given by

$$\boldsymbol{B}_\mathrm{M} = \boldsymbol{R}(-\chi, -\theta, -\phi) \boldsymbol{B}_\mathrm{L} \ . \tag{2.4}$$

---

[1] These are *passive* rotations, that is, only the representation of v is changed. v itself remains untouched.
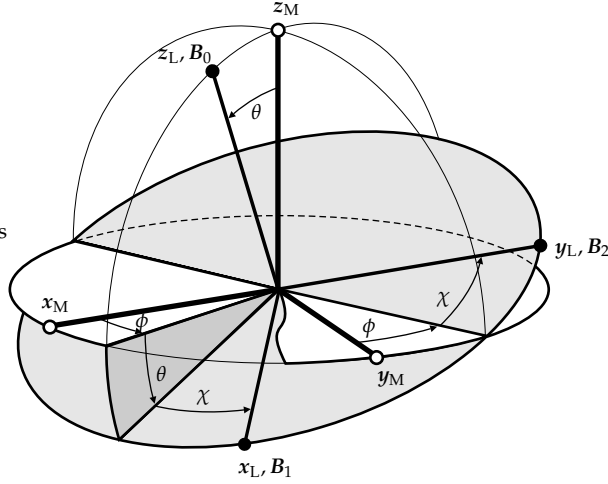
Figure 2.1: Relation between laboratory frame L and molecular frame M with the three Euler angles ϕ, θ and χ. This figure is a special case of Figure C.1 (p. 128) with $\alpha = \phi$, $\beta = \theta$ and $\gamma = \chi$.

The L unit vectors are in the M frame explicitly given by

$$x_{\mathrm{L,M}} = \begin{pmatrix} c\phi c\theta c\chi - s\phi s\chi \\ s\phi c\theta c\chi + c\phi s\chi \\ -s\phi c\chi \end{pmatrix} \quad y_{\mathrm{L,M}} = \begin{pmatrix} -c\phi c\theta s\chi - s\phi c\chi \\ -s\phi c\theta s\chi + c\phi c\chi \\ s\theta s\chi \end{pmatrix} \quad z_{\mathrm{L,M}} = \begin{pmatrix} c\phi s\theta \\ s\phi s\theta \\ c\theta \end{pmatrix}$$
$$(2.5)$$

with the abbreviations $c\phi = \cos\phi$, $s\phi = \sin\phi$ etc. The three L frame components of G in M representation are

$$G_{\mathrm{xL,M}} = x_{\mathrm{L,M}}^{\mathrm{T}} G_{\mathrm{M}} \qquad G_{\mathrm{yL,M}} = y_{\mathrm{L,M}}^{\mathrm{T}} G_{\mathrm{M}} \qquad G_{\mathrm{zL,M}} = z_{\mathrm{L,M}}^{\mathrm{T}} G_{\mathrm{M}} \qquad . \qquad (2.6)$$

With $B_{0,\mathrm{M}} = B_0 z_{\mathrm{L,M}}$ we get for the spin Hamiltonian in the absence of radiating fields

Static Hamiltonian

$$H_{\mathrm{M}} = F_{\mathrm{M}} + B_0 z_{\mathrm{L,M}} G_{\mathrm{M}} = F_{\mathrm{M}} + B_0 (c\phi s\theta\, G_{\mathrm{xM}} + s\phi s\theta\, G_{\mathrm{yM}} + c\theta\, G_{\mathrm{zM}}) \, , \qquad (2.7)$$

which depends only on two of the three Euler angles.

From now on we use all operators and vectors in the M frame representation and drop all M subscripts. The orientation of the external magnetic field z_{L} will occasionally be referred to as Ω.

Notation

2.1.2 States and energies

In a static external magnetic field, each of the N eigenstates $|u\rangle$ of a spin system

Degeneracy points

(a) (b)

PSfrag replacements

energy contours at $\boldsymbol{B}_0 = $ const

z_M

y_M

x_M
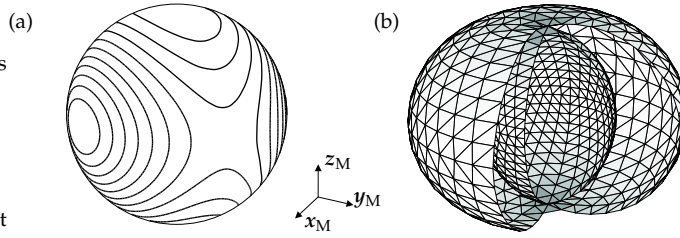
Figure 2.2: (a) Contour map of a typical function $E_u(\boldsymbol{B}_0)$ on the sphere defined by $|\boldsymbol{B}_0| =$ const. (b) Energy surfaces touching each other in single points. The surface is defined by $E_u(\boldsymbol{B}_0)\boldsymbol{z}_\mathrm{L}$ with constant B_0. A part is sliced out. Note that the 3D spaces in (a) and (b) are completely different.

has a defined energy (its eigenvalue) E_u, satisfying

$$H(\boldsymbol{B}_0)|u\rangle = E_u|u\rangle \ . \tag{2.8}$$

If all spins in the system are coupled and interact with the external magnetic field $\boldsymbol{B}_0$, the energies of different states will be different[1] for all $\boldsymbol{B}_0$ except possibly for some *isolated* points $\boldsymbol{B}_\mathrm{d}$, where two or more energies are degenerate $E_v(\boldsymbol{B}_\mathrm{d}) = E_u(\boldsymbol{B}_\mathrm{d})$. In addition, $E_u(\boldsymbol{B}_0)$ is a differentiable function in the entire $\boldsymbol{B}_0$ space except at $\boldsymbol{B}_\mathrm{d}$. It is physically intuitive that such points of degeneracy are indeed isolated, since any change of $\boldsymbol{B}_0$ away from $\boldsymbol{B}_\mathrm{d}$ will remove the degeneracy via the Zeeman interaction (if, again, all the spins are coupled).

State ordering 　As a consequence, E_v is either always $\geq E_u$ or always $\leq E_u$. We can distinguish between a higher and a lower state. Hence states can be ordered and labelled with numbers $|1\rangle, \dots, |N\rangle$ running from lowest to highest energy

$$E_1 < E_2 < \cdots < E_N \quad \text{for} \quad \boldsymbol{B}_0 \neq \boldsymbol{B}_\mathrm{d} \ . \tag{2.9}$$

Surfaces 　Geometrically, $E_u(\boldsymbol{B}_0)$ is a scalar field in 3D space. Experimental situations where the magnitude of $\boldsymbol{B}_0$ is held constant are equivalent to cutting out a sphere with radius B_0 (see Figure 2.2(a)). Energies will have orientation-dependent values on the sphere surface. They can also be pictured as smooth, closed surfaces $E_u(\boldsymbol{B}_0)\boldsymbol{z}_\mathrm{L}$, so-called energy surfaces (see Figure 2.2(b)). Any two surfaces can touch in single isolated points, but will never cross.

Anticrossings 　If one varies $\boldsymbol{B}_0$ in a way that it passes through $\boldsymbol{B}_\mathrm{d}$, states $|u\rangle$ and $|v\rangle$ seem to cross. Therefore points $\boldsymbol{B}_\mathrm{d}$ are usually referred to as "crossings". Of course, in the small neighbourhood of $\boldsymbol{B}_\mathrm{d}$, the two eigenvalues E_u and E_v are very close. This behaviour is usually called "anticrossing". Note that crossings occur only at single *points*, whereas anticrossings occur in the *space* around these singularities. Sometimes there are no degeneracy points and the surfaces just come very close, giving anticrossing regions without crossing points. State vectors change very

---

[1] For the mathematical background, see for example [Kat82], p. 72.
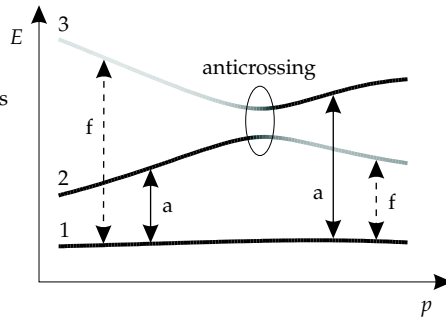
Figure 2.3: State energies E and state vectors (gray coded lines) as a function of a spin Hamiltonian parameter p. Transition $|1\rangle \leftrightarrow |2\rangle$ is allowed (a) on the left and forbidden (f) on the right of the anticrossing, transition $|1\rangle \leftrightarrow |3\rangle$ vice versa.

rapidly in an anticrossing region, as can be seen in Figure 2.3. This implies rapid changes of transition probabilities.

The properties of the $\boldsymbol{B}_0$ dependence of E_u cannot be generalised to other Hamiltonian parameters. In many cases, permanent degeneracies occur like for the system described by $H = DS_z^2$. Here, two energies $E_u(D)$ are degenerate independent of D.

Due to the finite numerical accuracy of $\boldsymbol{B}_0$, isolated degeneracies in $\boldsymbol{B}_0$ space will never be encountered in numerical computations, except at the uninteresting $\boldsymbol{B}_0 = 0$. We can therefore neglect the existence of crossing points and assume $E_u < E_v$ for all $\boldsymbol{B}_0$. The finite numerical accuracy can lead to another effect. Very sharp anticrossings can appear as degeneracies, if the splitting $E_v - E_u$ is smaller than the accuracy of the diagonalisation routine. In spectral simulations, this sometimes happens with three or more equivalent nuclei with small HF splitting. States with small total nuclear magnetic spin quantum number $\sum m_I$ in the centre of each electron manifold occasionally appear to be degenerate. To avoid these coincidental degeneracies, the HF constants are changed by a small random amount (10^{-8} relative so as not to hamper the overall accuracy) before the simulation.

There has been an attempt to determine whether an anticrossing or a real crossing (with degenerate states) occurs between two points in $\boldsymbol{B}_0$ space [Gri90]. By comparing the character of the eigenstates on the left and on the right, a possible crossing should be identified, if the eigenvectors exchange their character. But this is true for very sharp anticrossings as well and depends on the sharpness of anticrossings compared to the distance between the two field values used.

Sometimes [vV78, Kre91, Mis99] it has been proposed that the Jacobi diagonalisation method [Gol96] conserves the "right" order of the eigenstates when using the eigenstates on the left of the (anti)crossing to compute the eigenstates on the right. It is true that the Jacobi method orders states according to their character and not their eigenvalues. But in this case the eigenvalues will swap at the anti-

(margin notes) Numerical aspects

"Tracking"

Jacobi "order"

crossing point, so that $E_1 < E_2$ on the left and $E_1 > E_2$ on the right. This creates a false discontinuity and is not correct.

Transitions   Transitions are labelled by the numbers u and v of the two eigenstates connected by the transition. Transition frequencies are differences of the associated energies

$$\Delta_{vu} = E_v - E_u \ . \tag{2.10}$$

Like the energies, they are analytical functions of B_0 and can be pictured as surfaces. Since they are differences of the energies, they can cross without complications for the labelling and the computation.

2.1.3 Perturbation theory

Classical PT   A theoretical concept much applied in simulations of EPR spectra is the classical Rayleigh-Schrödinger perturbation theory (PT) [Sak85]. Although it was heavily used to derive approximative analytical solutions, it can be and is used for numerical work as well, since its results are closely related to eigenvalue and eigenvector derivatives, as we will see in Section 2.1.4. Here we collect general and compact formulas which are not available in the EPR literature.

In perturbation theory, an eigensystem with unknown solution

$$(H - E_u)|u\rangle = (H^{(0)} + H^{(1)} - E_u)|u\rangle = 0 \tag{2.11}$$

is solved in terms of an eigensystem

$$(H^{(0)} - E_u^{(0)})|u^{(0)}\rangle = 0 \tag{2.12}$$

with known solution. $H^{(1)}$ should be small compared to $H^{(0)}$. The eigenvectors $|u^{(0)}\rangle$ are normalised to unity. We expand eigenvalues and eigenvectors of the unsolved system in a power series in λ

$$\left(H^{(0)} + \lambda H^{(1)} - \sum_{k=0}^{\infty} \lambda^k E_u^{(k)}\right) \sum_{k=0}^{\infty} \lambda^k |u^{(k)}\rangle = 0 \tag{2.13}$$

with the important constraint $\langle u^{(k)}|u^{(0)}\rangle = 0$. With $\lambda = 0$, the solution is known, and going to $\lambda = 1$ gives the unsolved eigensystem. The solution is found by the requirement that all coefficients to λ^k must vanish (since the above equation must be valid for all λ).

The resulting expression for the energy corrections $E_u^{(k)}$ are staggeringly simple

$$E_u = \sum_{k=0}^{\infty} E_u^{(k)} \quad \text{with} \quad E_u^{(k)} = \langle u^{(0)}|H^{(1)}|u^{(k-1)}\rangle \ . \tag{2.14}$$

Eigenvector corrections are slightly more complicated

$$|u\rangle = \sum_{k=0}^{\infty} |u^{(k)}\rangle \quad \text{with} \quad |u^{(k)}\rangle = P_u \left(H^{(1)}|u^{(k-1)}\rangle - \sum_{l=1}^{k-1} E_u^{(l)}|u^{(k-l)}\rangle\right) \tag{2.15}$$

with the complementary projector

$$P_u = - \sum_{v \neq u} \frac{|v^{(0)}\rangle \langle v^{(0)}|}{E_v^{(0)} - E_u^{(0)}} \ . \tag{2.16}$$

The corrected eigenvector $|u\rangle$ has to be re-normalised.

The above formulas are only a special case of the general expressions obtained   General PT
if H is also expanded into a powder series in λ

$$H = \sum_{k=0}^{\infty} \lambda^k H^{(k)} \tag{2.17}$$

and not truncated after the first order as in classical Rayleigh-Schrödinger theory.
The general solutions are

$$E_u^{(k)} = \langle u^{(0)}| \sum_{l=1}^{k} H^{(l)} |u^{(k-l)}\rangle \tag{2.18}$$

$$|u^{(k)}\rangle = P_u \left(\sum_{l=1}^{k-1} \left(H^{(l)} - E_u^{(l)} \right) |u^{(k-l)}\rangle + H^{(k)} |u^{(0)}\rangle \right) \ . \tag{2.19}$$

A special form of perturbation theory is frequency-shift (or eigenfield) perturbation theory. It is discussed in Section 2.2.1, since it is only applicable to cw EPR.

Numerically, Eq. (2.14) and Eq. (2.15) can be implemented very compactly in   Matrix form
matrix form, so that the corrections for all eigenvalues and eigenvectors are computed simultaneously. $H^{(0)}$ is diagonalised

$$V^{(0)\dagger} H^{(0)} V^{(0)} = E^{(0)} \ , \tag{2.20}$$

giving a unitary matrix $V^{(0)}$ with the eigenvectors along the rows and a diagonal
matrix $E^{(0)}$ with the eigenvalues on the diagonal. All operators (including $H^{(1)}$)
are then transformed to the eigenbasis of $H^{(0)}$. In this basis, $H^{(0)} = E^{(0)}$, $V^{(0)} = \mathbb{1}_N$, and P_u is diagonal for each u. The diagonals of all P_u can then be collected as
rows into the projector matrix Q with elements

$$Q(v, u) = - \frac{\delta_{v,u}}{E_0(v, v) - E_0(u, u)} \ . \tag{2.21}$$

The resulting matrix expressions[1] for the perturbational corrections are

$$E^{(k)} = \text{diag} \left(R^{(k-1)} \right) \quad \text{with} \quad R^{(k)} = H^{(1)} V^{(k)} \tag{2.22}$$

$$V^{(k)} = Q .* \left[R^{(k-1)} - \sum_{l=1}^{k-1} V^{(k-l)} E^{(l)} \right] \ . \tag{2.23}$$

These formulas are derived here for the first time.

---

[1] $\text{diag}(A)$ of matrix A is A with all off-diagonal elements set to zero. The operator $.*$ indicates
element-wise multiplication.

2.1.4 Derivatives

Derivatives of energy eigenvalues and eigenvectors with respect to the external magnetic field and other spin Hamiltonian parameters are of prime importance in spectral simulations. They are used for interpolation, resonance field computations, strain modelling and optimisation algorithms. Here we summarise the most important formulas[1].

Feynman's theorem   The first derivative of a non-degenerate energy eigenvalue E_u with respect to a parameter p of the Hamiltonian is given by the Hellmann-Feynman theorem [Fey39]

$$\frac{\partial E_u}{\partial p} = \langle u|\frac{\partial H}{\partial p}|u\rangle \ , \tag{2.24}$$

where $|u\rangle$ is the associated eigenvector. Most important is the derivative with respect to the external magnetic field

$$\frac{\partial E_u}{\partial B} = \langle u|\frac{\partial H}{\partial B}|u\rangle = \langle u|G_{zL}|u\rangle \ . \tag{2.25}$$

General derivatives   Second derivatives were also derived [Mis76]. More generally, if $\partial^2 H/\partial p^2 = 0$, i.e. when p is a linear parameter of the spin Hamiltonian, which is commonly the case, then the derivatives are proportional to the classical perturbational corrections of Eq. (2.14) and Eq. (2.15) with $H^{(1)} = \partial H/\partial p$

$$\frac{\partial^k E_u}{\partial p^k} = \frac{k!}{(p-p_0)^{k-1}}E_u^{(k)} \qquad \frac{\partial^k|u\rangle}{\partial p^k} = \frac{k!}{(p-p_0)^{k-1}}E_u^{(k)}|u^{(k)}\rangle \ , \tag{2.26}$$

where p_0 is the value of the parameter p in the unperturbed Hamiltonian $H^{(0)}$.

If p is not a linear parameter of H, then the perturbational corrections of Eq. (2.18) and $H^{(k)} = \partial^k H/\partial p^k$ have to be used instead. All formulas are valid only for non-degenerate eigenvalues. All energy derivatives are real, since E_u is real and all parameters p of the spin Hamiltonian are real.

Orientational gradient   Another important quantity is the orientational gradient of a state energy. For constant B_0, E_u is defined on a sphere $|B_0| = $ const in B_0 space. If the orientation of the magnetic field is changed, E_u changes as well. This is equivalent to moving on the sphere surface of Figure 2.2(a). Therefore, for a point on the sphere surface, the orientational gradient of a state energy E_u in the laboratory frame can be calculated

$$\nabla E_u = \begin{pmatrix} \langle u|G_{xL}|u\rangle \\ \langle u|G_{yL}|u\rangle \end{pmatrix} \tag{2.27}$$

with the external magnetic field along z_L. ∇E_u is the projection of the gradient of the 3D function $E_u(B_0)$ onto the tangent plane of the 2D sphere surface. An often

---

[1] Many workers use difference quotient approximations to some of these derivatives and seem not to be aware of the analytical formulas.

needed quantity is the magnitude of this gradient for a transition frequency

$$|\nabla(E_v - E_u)| = \sqrt{(\langle v|G_{\mathrm{xL}}|v\rangle - \langle u|G_{\mathrm{xL}}|u\rangle)^2 + (\langle v|G_{\mathrm{yL}}|v\rangle - \langle u|G_{\mathrm{yL}}|u\rangle)^2}. \quad (2.28)$$

The differences in this formula (and similar terms like the $1/g$ factor, see Eq. (2.52)) can be computed in a quick and very handy way

$$\langle v|A|v\rangle - \langle u|A|u\rangle = \mathrm{Re}\left[(\langle v| + \langle u|)A(|v\rangle - |u\rangle)\right], \quad (2.29)$$

saving two of the four vector-matrix multiplications.

2.2 cw EPR peaks

In this section, we first give an overview of existing methods for computing cw EPR resonance fields, before introducing a new one. After that we describe the computation of line intensities.

2.2.1 Resonance fields - known methods

For a spin system with magnetic field orientation $\boldsymbol{\Omega} \equiv \boldsymbol{z}_{\mathrm{L}}$, resonance in the cw EPR experiment occurs each time the magnetic field reaches a value such that the energies of two states $|u\rangle$ and $|v\rangle$ in the spin system are separated exactly by a quantum ν of the radiating microwave

Eigenfields

$$\begin{aligned}
\left[F + BG_{\mathrm{zL}}(\boldsymbol{\Omega})\right]|u\rangle &= E_u|u\rangle \\
\left[F + BG_{\mathrm{zL}}(\boldsymbol{\Omega})\right]|v\rangle &= (E_u + \nu)|v\rangle \ .
\end{aligned} \quad (2.30)$$

These fields B are called the resonance fields or eigenfields of the system. This is equivalent to finding the roots of the implicit function $\Delta_{vu}(B) - \nu$

$$\Delta_{vu}(B) - \nu = E_v(B) - E_u(B) - \nu = 0 \ . \quad (2.31)$$

The set of equations Eq. (2.30) is not directly solvable in state space, neither numerically nor analytically. In Liouville space, however, the problem can be formulated and solved in an explicit form [Bel73]. Then the eigenfields are the eigenvalues B from the general eigenvalue problem[1]

General eigenproblem

$$(F \otimes \mathbb{1}_N - \mathbb{1}_N \otimes F^* - \nu\mathbb{1}_N \otimes \mathbb{1}_N)Z = B(G_{\mathrm{zL}}^* \otimes \mathbb{1}_N - \mathbb{1}_N \otimes G_{\mathrm{zL}})Z \quad (2.32)$$

with $Z = |u\rangle \otimes |v\rangle$. If B is an eigenfield and Z its associated transition eigenvector, the states $|u\rangle$ and $|v\rangle$ are at resonance.

---

[1] The $\otimes$ product is defined in Appendix A. Its definition and consequently the exact form of Eq. (2.32) is different from that in [Bel73].

Table 2.1: Published numerical methods for locating resonance fields for a given orientation.

Class	Method	References
Direct	eigenfield	[Bel73, Scu82]
Extrapolation	classical PT	[Kei87, Gri90]
	frequency-shift PT	[Bel74, Nil79, Wan96, Gri99]
Root finding	Newton-Raphson	[Swa64, vV78, Kre91, Gaf93, Mor99]
	Muller's method	[Mac69, Net85]
Homotopy	Newton-Raphson[†]	[Gat98]
	least-squares	[Mis76]
Interpolation	cubic splines	[Gle91, Gaf98]
	Chebyshev	[Mab92]

[†] Uses Rayleigh inverse iteration instead of full diagonalisation.

For a pair of states there might exist more than one resonance field, so that more than one line appears in the field-swept spectrum. This is in marked contrast to frequency-swept spectra, where only one resonance per state pair is possible. Transitions with multiple resonance fields are referred to as looping transitions [Gaf98]. They can only occur if ν is not larger than the largest eigenvalue difference at zero field [Bel73]

$$\nu \leq E_N(0) - E_1(0) \ . \tag{2.33}$$

In the other case, only one resonance field per state pair is possible.

Numerics
The properties of Eq. (2.32) have been studied in detail [Bel73]. A few possibilities for speed-up of the numerical implementation have been hinted at [Čug94]. Still, the eigenfield method is very expensive. E.g. for an $S = 1/2$ system with a ^{63}Cu and four ^{14}N nuclei coupled to the electron, there are 628 states. Since none of the nuclei can be neglected, the eigenfield equation would have to deal with matrices of dimension $628^2 = 394384$. Using double precision arithmetic (16 bytes per complex number), a real matrix would need 2318 GB of memory. Methods for handling sparse matrices can reduce this amount, but nevertheless general eigenfield computations are feasible only for small systems or on very powerful computers. Approximation methods that operate in the much smaller state space are necessary and have been used extensively.

Approximations
Such approximation methods are often based on perturbation theory. Analytical perturbational methods were used to derive explicit formulas for resonance fields for certain spin Hamiltonians (see [Tay75] for a collection of formulas). But when two interactions in the spin Hamiltonian are of comparable magnitude, these formulas are not valid anymore, and one has to resort to a completely numerical treatment. Different published approaches are summarised in Table 2.1 and discussed in the following.

Taylor series
One class of methods uses extrapolation. If the resonance field B is sufficiently

close to a starting guess B_0, E_u and E_v can be expanded in a Taylor series around B_0

$$E_u(B) = \sum_{k=0}^{\infty} \frac{1}{k!} (B - B_0)^k \frac{\partial^k E_u(B_0)}{\partial B^k} \tag{2.34}$$

and truncated after the first order. After inserting the derivatives from Eq. (2.26), the resulting linear equation gives a first-order estimate of the resonance field

$$B = B_0 + \frac{\nu - (E_v^{(0)} - E_u^{(0)})}{\langle v^{(0)}|G_{zL}|v^{(0)}\rangle - \langle u^{(0)}|G_{zL}|u^{(0)}\rangle} \ . \tag{2.35}$$

Truncating Eq. (2.34) after the second order gives the quadratic equation

$$\nu = (E_v^{(0)} - E_u^{(0)}) + (E_v^{(1)} - E_u^{(1)})(B - B_0) + (E_v^{(2)} - E_u^{(2)})(B - B_0)^2 \ , \tag{2.36}$$

which can also be used to compute B. The eigenvectors are then corrected by inserting B into the similar equation

$$|u\rangle = |u^{(0)}\rangle + (B - B_0)|u^{(1)}\rangle + (B - B_0)^2|u^{(2)}\rangle \ . \tag{2.37}$$

(or the linear one).

A similar approach occasionally used [Nil79, Scu82] is frequency-shift perturbation theory [Bel74], also called eigenfield perturbation theory [Wan96]. In contrast to classical perturbation theory, the eigenvectors and the spin Hamiltonian are corrected to all orders, whereas the energy difference between two states is only corrected to first order with

$$E_{vu}^{(1)} = \nu - (E_v^{(0)} - E_u^{(0)}) \ . \tag{2.38}$$

The resonance field is obtained as a sum over all orders of corrections to an initial field guess $B^{(0)}$

$$B = \sum_k B^{(k)} \quad \text{with} \quad B^{(1)} = \frac{E_{vu}^{(1)}}{\langle v^{(0)}|G_{zL}|v^{(0)}\rangle - \langle u^{(0)}|G_{zL}|u^{(0)}\rangle}$$
$$B^{(k)} = \sum_{l=1}^{k-1} B^{(l)} \frac{\langle v^{(0)}|G_{zL}|v^{(k-l)}\rangle - \langle u^{(0)}|G_{zL}|u^{(n-l)}\rangle}{\langle v^{(0)}|G_{zL}|v^{(0)}\rangle - \langle u^{(0)}|G_{zL}|u^{(0)}\rangle} \ . \tag{2.39}$$

The zeroth-order eigenpairs are obtained from a starting guess. Eigenvectors are computed from Eq. (2.18). Note that the first-order correction is identical to the one of Eq. (2.35).

For a given orientation $\mathbf{\Omega}$ and transition $|u\rangle \leftrightarrow |v\rangle$, Eq. (2.30) can also be solved for B by applying standard root finding algorithms [Pre92] to Eq. (2.31). The Newton-Raphson method has often been used, sometimes supplemented with bisection, quadratic interpolation (Muller's method [Mac69, Net85]) and other

methods. In the Newton-Raphson method, a starting guess B_0 is iteratively refined using

$$B_n = B_{n-1} - \frac{E_v(B_{n-1}) - E_u(B_{n-1}) - \nu}{\langle v|G_{zL}|v\rangle - \langle u|G_{zL}|u\rangle} \, , \qquad (2.40)$$

until convergence is reached. In contrast to the perturbational approaches mentioned above, eigenvalues and eigenvectors are recomputed here in each iteration step. This makes the method much more expensive, but also much more reliable. Starting guesses do not have to be so close to the eigenfield as in the other approaches. The first step $B_0 \to B_1$ in this approach is identical to the Taylor series approach to first order (Eq. (2.35)).

Bracketing All extrapolation and root-finding methods work reliably only on a narrow field range, so that the experimental field range is usually divided into segments, each being searched separately for resonance fields. By this segmentation, the roots of Eq. (2.31) are bracketed. For non-looping transitions, the resonance field for a given transition will lie only in one of the segments. Otherwise, any number of resonance fields in any number of segments are basically possible. The number of segments must be sufficiently high to be sure that there is no more than one eigenfield per segment. When extrapolation methods are used, energy levels and states have to be traced carefully across segments.

Homotopy Resonance fields and eigenpairs of a spin Hamiltonian for a given orientation can be computed in two different ways. The simple one is to construct and diagonalise the Hamiltonian independently without using any results of prior diagonalisations. The other one is to use the known eigenpairs of a close and already diagonalised spin Hamiltonian as starting points for computing the unknown eigenpairs. This so-called homotopy method has been applied to trace eigenpairs both across orientation and magnetic field changes. Gates [Gat98] has used Rayleigh inverse iteration combined with Newton-Raphson to find the resonance fields, whereas Misra [Mis76] has employed Jacobi diagonalisation together with an iterative least-squares minimisation of $(\Delta_{vu}(B) - \nu)^2$. In both methods, the resonance field of a close orientation is used as starting value for the root-search iteration.

Homotopy is elegant and saves some time, but it is not very robust in the case of anticrossings and bigger changes in B. Looping transitions are difficult to treat [Gat98]. In contrast to all other methods, the computation of resonance fields for different orientations is not independent in homotopy, so the method is not easily parallelisable and needs more elaborate data handling.

Level diagram Another method to find resonance fields for a given orientation is to diagonalise the spin Hamiltonian for a number of fields in the given experimental range and to interpolate between them with cubic splines or Chebyshev polynomials to model the full energy level diagram and to find the solutions to Eq. (2.31) [Gle91, Gaf98, Mab92]. Still, the number and the values of the field at which the Hamiltonian is diagonalised must be specified by hand. We will now present an improved method that builds upon this modelling approach.
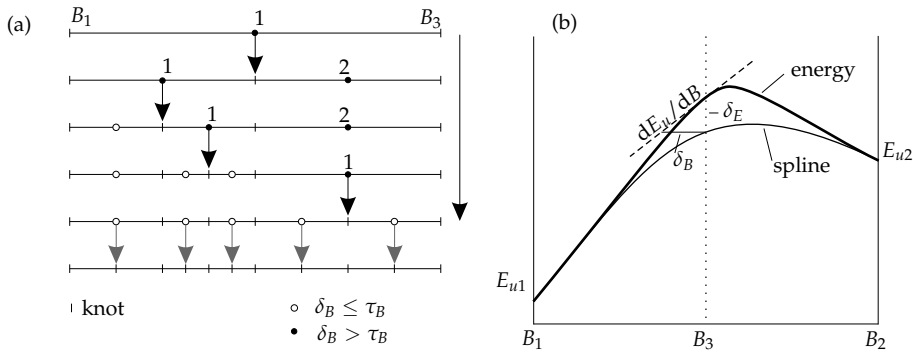
Figure 2.4: (a) The adaptive segmentation iteratively subdivides the segment with the largest error estimate until all segment errors are below threshold τ_B. In the last step, segment centres and corners are combined. (b) Approximating an energy level by a cubic spline with the error at the segment centre.

2.2.2 Resonance fields - new method

The methods of the previous section have problems. The eigenfield method is too expensive. Extrapolation methods do not know whether their truncation is accurate enough for the given starting field. Root finding methods are only locally convergent and might fail due to inappropriate starting guesses. Homotopy methods can fail on anticrossings and looping transitions [Wan96].

The primary remedy is to divide the field search range into a number K of small segments. Their centre fields serve as extrapolation points or as reasonable starting values for root finding algorithms. However, it is the user who has to inspect the final spectrum and decide whether a certain K is accurate enough or not [Wan96]. But it is easy to devise a scheme that is completely robust and does not need intervention by the user.

The method models the energy diagram using cubic polynomials (splines) as   Principles energy level approximations in each of a number of segments. Cubic modelling has already been applied by others [Gle91, Gaf98] using a given number of segments. Here, we use an *adaptive* segmentation procedure. Starting from one initial segment with the border knots $B_{\min}$ and $B_{\max}$, the modelling error for each segment is estimated and the segment with the largest error is subdivided into two segments by placing a new knot at the centre (or near it). This procedure is repeated until the largest segment error falls below a threshold (see Figure 2.4(a)). As a result, the number of segments is just high enough to give a good spline model and not higher. The knot density adapts to the local complexity of the energy diagram.

For a given field, E_u and $\partial E_u / \partial B$ can be computed by diagonalising the spin   Hermite Hamiltonian and applying Eq. (2.26). For a field segment with borders B_1 and B_2 spline it is then straightforward to compute the cubic Hermite interpolation polynomial

25

for each energy level. In a convenient matrix notation it reads

$$\tilde{E}_u(B) = \boldsymbol{t}^{\mathrm{T}}\boldsymbol{M}\boldsymbol{c}_u = \begin{pmatrix} t^3 & t^2 & t & 1 \end{pmatrix} \begin{pmatrix} 2 & -2 & 1 & 1 \\ -3 & 3 & -2 & -1 \\ 0 & 0 & 1 & 0 \\ 1 & 0 & 0 & 0 \end{pmatrix} \begin{pmatrix} E_u(B_1) \\ E_u(B_2) \\ \Delta B\, \partial E_u(B_1)/\partial B \\ \Delta B\, \partial E_u(B_2)/\partial B \end{pmatrix} \quad (2.41)$$

with $t = (B - B_1)/\Delta B$ and $\Delta B = B_2 - B_1$. $\tilde{E}_u(B)$ passes through the two border points with the two slopes supplied (Figure 2.4(b)).

Error estimate   Of course, this polynomial will deviate to some degree from the true E_u curve between B_1 and B_2 (see Figure 2.4(b)). It is desirable to minimise the maximum deviation of the interpolated energy levels from the true ones δ_E. The only viable method to get hold of an estimate of this deviation is to check $\tilde{E}_u$ at the segment centre $B_3 = (B_1 + B_2)/2$ (i.e. $t = 1/2$)

$$\tilde{E}_u(B_3) = \frac{1}{2}\Big[E_u(B_1) + E_u(B_2)\Big] + \frac{\Delta B}{8}\left[\frac{\partial E_u(B_1)}{\partial B} - \frac{\partial E_u(B_2)}{\partial B}\right] \quad (2.42)$$

against the correct energies there and look for the largest deviation

$$\tilde{\delta}_E = \max_u \left| E_u(B_3) - \tilde{E}_u(B_3) \right| . \quad (2.43)$$

It is the resonance field though which we are interested in, so it is more appropriate to use

$$\tilde{\delta}_B = \max_u \left| \frac{E_u(B_3) - \tilde{E}_u(B_3)}{\partial E_u(B_3)/\partial B} \right| \quad (2.44)$$

as the error measure. If the denominator is close to zero, $\tilde{\delta}_B$ will be large, meaning that flat regions are modelled more accurately.

In this procedure, the spin Hamiltonian at the segment centre is diagonalised for estimating the error. If the segment is subdivided, the eigenpairs are already computed. If not, they are not wasted, since they can be included in the final segmentation (see Figure 2.4(a)).

Threshold   If $\tilde{\delta}_B$ falls below a certain threshold τ_B, the segment between B_1 and B_2 can be assumed to be reasonably modelled by the cubic spline. If $\tilde{\delta}_B > \tau_B$, then the segment has to be divided at the centre field B_3 into two segments, which are then separately modelled and checked.

It is possible to automatically estimate a value for the threshold τ_B. The resonance fields have to be correct to within the step size of the field axis. Given the field range $B_{\min}$ to $B_{\max}$ and the number n_B of field points to simulate, the accuracy of the field search procedure needed is

$$\tau_B \approx \frac{B_{\max} - B_{\min}}{n_B} . \quad (2.45)$$

Extensive numerical tests have shown that the real maximum error of the diagram is between $0.001\,\tilde{\delta}_B$ and $5\,\tilde{\delta}_B$. It is larger than the estimate for very sharp and

(a)

ag replacements

(b)
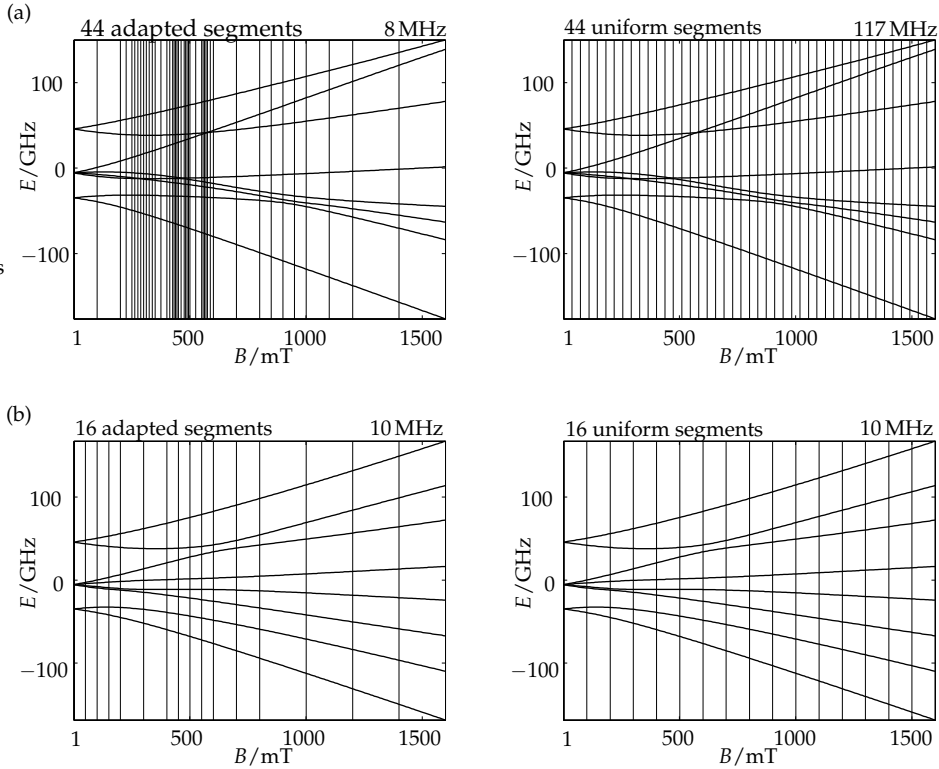
Figure 2.5: Adaptive segmentation for modelling the energy diagram of Tb^{4+} in ThO_2 (see [Abr86], p. 337, for spin Hamiltonian parameters) compared to equidistant segmentation with the same number of segments. (a) $(\phi, \theta) = (45°, 4°)$, (b) $(\phi, \theta) = (15°, 27°)$. The total maximum deviation δ_E is given on the top right of each diagram.

hence very badly modelled anticrossings, occurring mainly for magnetic field orientations near principal directions of an interaction tensor or matrix. However, this maximal error from the diagram will translate into the EPR spectrum only for certain spectrometer frequencies, that is, when the resonance fields are indeed very close to the anticrossings. Usually the error for field positions is much smaller.

We illustrate the method with a rather complex spin system. In Figure 2.5 the energy level diagrams for two different orientations are shown. The sharper anticrossings are, the more segments the bisection procedure will automatically generate. The real error compared to a uniform segmentation with the same number of segments is usually smaller. Whereas for equidistant segmentation *K* has to be optimised manually, the adaptive method automatically increases *K* as much as necessary. As can be seen in the figure, the adaptive *K* is orientation-dependent.

Adaptive vs. uniform

PSfrag replacements
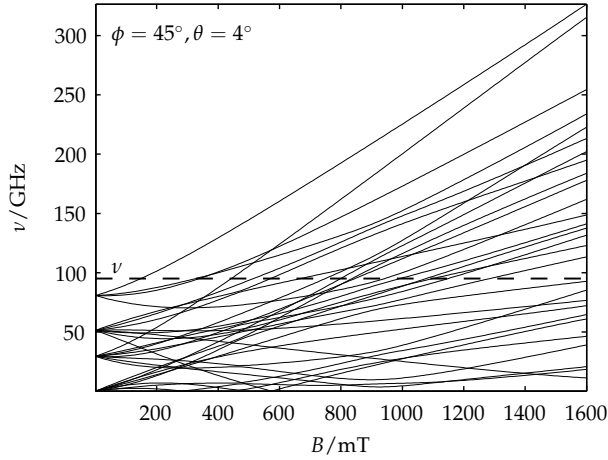
Figure 2.6: Energy difference between all energy levels of the Tb^{4+} system of Figure 2.5. The intersection with ν (here 95 GHz) gives the resonance fields.

The equidistant method uses one value for all orientations, leading to larger errors along principal axis directions.

The Tb^{4+} system is quite unusual. For more commonplace situations, like cw EPR of d transition metal ions between X band and W band, much fewer segments are needed. Any Cu^{2+} or VO^{2+} spectrum with $\nu \geq 2\,\text{GHz}$ can be simulated with 2 segments. Spectra of high-spin Fe^{3+} need between 2 segments if $D \gg \nu$ and up to 40 segments if $D \approx \nu$.

Polynomial roots   Once the energy levels have been modelled in the field range of interest, in the second step the resonance fields at the spectrometer frequency ν can be located. For a given transition $|v\rangle \leftrightarrow |u\rangle$, the difference polynomials

$$\tilde{E}_v - \tilde{E}_u - \nu = t^T p - \nu$$
$$p = (p_3, p_2, p_1, p_0)^T = M(c_v - c_u) . \tag{2.46}$$

of all segments are checked (see Figure 2.6). Their roots t_0 give the resonance fields $B = B_1 + t_0(B_2 - B_1)$. If no looping transitions are possible, i.e. when ν is bigger than $E_N - E_1$ at *zero* field [Bel73], at most one root will lie in the segment and Newton-Raphson

$$t_0 = \frac{1}{2} \quad \text{(or some other value)}$$
$$t_{n+1} = t_n - \frac{p_3 t^3 + p_2 t^2 + p_1 t + p_0 - \nu}{3p_3 t^2 + 2p_2 t + p_1} \tag{2.47}$$

or Muller's method can be used to locate it. If looping transitions are possible, first compute $\Delta_p = p_2^2 - 3p_3 p_1$. If $\Delta_p \leq 0$, the polynomial is monotonic, has only

one root and the above root-finding methods can be used. If $\Delta_p > 0$, up to 3 roots are possible and can be obtained as the eigenvalues of the companion matrix

$$\begin{pmatrix} -\frac{p_2}{p_3} & -\frac{p_1}{p_3} & -\frac{p_0-\nu}{p_3} \\ 1 & 0 & 0 \\ 0 & 1 & 0 \end{pmatrix} . \tag{2.48}$$

Very often $p_3 \ll p_0, p_1, p_2$, and the cubic polynomial can be reduced to a quadratic one.

With the resonance B found, the eigenvectors can be computed by linear or cubic interpolation between the eigenvectors of the two adjacent knots. For cubic interpolation, $\partial|u\rangle/\partial B$ has to be evaluated according to Eq. (2.26). In general, linear interpolation is accurate enough.

The modelling method can also use the information about the spectrometer frequency. Any segment with $E_N - E_1 < \nu$ at both borders will not contain any resonance and can be neglected. $\quad\nu$ cut-off

With this new adaptive bisection procedure, resonance field searches are auto-tuning to the difficulty of the problem, specified by the spin system, its orientation, $B_{\min}$, $B_{\max}$, n_B and ν. Accuracy is guaranteed and no additional user parameters are required.

2.2.3 Intensities

Although a full quantum mechanical re-examination of the field-modulated cw EPR experiment has revealed that in reality the experiment is a multi-photon single-quantum spectroscopy [Käl03], we stick to the established picture that treats it as an absorption experiment, adding the field modulation as an electronic effect that causes the "derivative" observed in experiment (see p. 60).

Once the eigenvectors and the resonance field of a particular transition are found, we can compute the transition intensity (absorption rate) due to the incident microwave radiation $\quad$ Fermi's Golden Rule

$$H_1(\boldsymbol{B}_1) = 2B_1 G_{\mathrm{xL}} \cos(2\pi\nu t) = B_1 \left(e^{i2\pi\nu t} + e^{-i2\pi\nu t} \right) G_{\mathrm{xL}} \tag{2.49}$$

(for perpendicular excitation). It is common to make the approximation $|\boldsymbol{B}_1| \ll |\boldsymbol{B}_0|$, which holds in almost all cases. Time-dependent perturbation theory then gives for the intensity

$$A_{vu} = \frac{2\pi}{\hbar} B_1^2 |\langle v|G_{\mathrm{xL}}|u\rangle|^2 = \frac{2\pi}{\hbar} B_1^2 |\mathrm{tr}\left(G_{\mathrm{xL}}|u\rangle\langle v|\right)|^2 \tag{2.50}$$

(Fermi's Golden Rule[1]). Experience shows that this formula is sufficient to account for all intensity variations in cw EPR spectra, when the additional $1/g$

---

[1] The formula is actually from Dirac's original work on time-dependent perturbation theory (1926,1927), but Fermi termed it Golden Rule in his 1949 course on nuclear physics at the University of Chicago ([Fer50], p. 142). It is valid only for populations. Coherence effects are not included. In addition, detection and excitation fields have to be parallel.
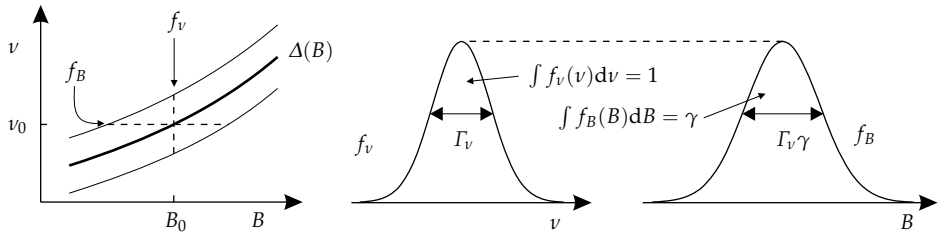
Figure 2.7: Relation between field and frequency swept spectra of a single line. γ is defined in Eq. (2.52).

factor [Aas75] is included.

1/g factor

This factor is due to the fact that in cw EPR the field and not the frequency is swept. In a two-dimensional spectrum (see Figure 2.7) the line width Γ_B in a cross-section along B (field sweep) is in a linear approximation proportional to the line width Γ_ν in a cross-section along ν (frequency sweep), if the line width Γ and the first derivative of the transition frequency $\Delta(B)$ are approximately constant within the spread of the resonance line

$$\Gamma_B \approx \Gamma_\nu \gamma \ . \tag{2.51}$$

The factor is the inverse of the partial derivative of the energy separation with respect to the field

$$\gamma = \left[\frac{\partial (E_v - E_u)}{\partial B} \right]^{-1} = \frac{1}{\langle v | G_{zL} | v \rangle - \langle u | G_{zL} | u \rangle} \ . \tag{2.52}$$

For high magnetic fields $|v\rangle$ and $|u\rangle$ are Electron Zeeman eigenstates, and γ is proportional to $1/g$.

Width and intensity

Since the line widths of the two shapes in Figure 2.7 are different, but have the same amplitude, their integrals differ by a factor γ. Therefore, the $1/g$ factor has to be included in the line width *and* in the line intensity, if normalized line shape functions (as in Appendix B) are used. Close to coalescence points of looping transitions the approximation in Eq. (2.51) is too coarse and the frequency-to-field conversion leads to a distortion of the line shape due to the nonlinearity of the transition energy $\Delta(B)$. In this case, cubic polynomials can be used to model the line shape in field domain [Gaf98].

Integral over χ

The intensity depends not only on the orientation of B_0, but on B_1 as well. For a powder spectrum and a given B_0 direction, the intensity of Eq. (2.50) has to be integrated over all B_1 orientations, i.e. the plane perpendicular to B_0. This is an integral over the third Euler angle χ and can be solved analytically in a

30

straightforward manner[1]

$$\int\limits_{\boldsymbol{B}_1 \perp \boldsymbol{B}_0} |\langle v|\boldsymbol{B}_1^{\mathrm{T}} \boldsymbol{G}|u\rangle|^2 \, \mathrm{d}\boldsymbol{B}_1 = B_1^2 \int_0^{2\pi} |\langle v|G_{\mathrm{xL}} \cos \chi + G_{\mathrm{yL}} \sin \chi)|u\rangle|^2 \, \mathrm{d}\chi$$

$$= \pi B_1^2 \left[|\langle v|G_{\mathrm{xL}}|u\rangle|^2 + |\langle v|G_{\mathrm{yL}}|u\rangle|^2 \right] . \qquad (2.53)$$

Consequently, the integrated intensity is proportional to the sum of the intensities of two perpendicular $\boldsymbol{B}_1$ orientations. Eq. (2.53) cannot be simplified further.

If the temperature is such that it does not satisfy the high-temperature criterion[2]

$$\left| \frac{\hbar H}{k_{\mathrm{B}} T} \right| \ll 1 , \qquad (2.54)$$

a factor proportional to the Boltzmann population difference of the two states of a transition has to be included, giving the total peak intensity

$$A = \gamma A_{vu} (\beta_v - \beta_u) \quad \text{with} \quad \beta_v = \frac{\mathrm{e}^{-\frac{h}{k_{\mathrm{B}} T} E_v}}{\sum_m \mathrm{e}^{-\frac{h}{k_{\mathrm{B}} T} E_m}} . \qquad (2.55)$$

Population effects

2.3 Line widths

In practice, the one-Hamiltonian model giving a stick spectrum is not applicable for a sample containing around 10^{10} spin systems. Resonance lines are broadened by one or both of two different broadening mechanisms, homogeneous or inhomogeneous.

2.3.1 Homogeneous broadening

Any resonance is associated with the generation of non-equilibrium populations or coherences in the spin system. These excited states are not stable and decay stochastically to the ground state by exchanging[3] energy with the surroundings (the so-called lattice). Due to Heisenberg's uncertainty principle, this uncertain lifetime implies an uncertainty in the state energies of the two levels involved, i.e. the transition frequency is not exactly ν_p, but distributed around it. Hence the resonance line will have a shape of finite width, usually a Lorentzian (see Appendix B). If an excited state has a decay constant τ, the width of the associated resonance line is $2/\tau$. Decay (relaxation) constants for populations are termed T_1, those for coherences T_2. They depend on the presence of external radiation fields.

Homogeneous broadening is mostly negligible in solid-state EPR powder spec-

Decay times

Convolution

---

[1] This was shown as early as 1964 [Was64, vV78], but even in 1987 [Kei87] numerical integration was used.

[2] As a norm, one can use the largest eigenvalue difference.

[3] Spontaneous emissions are extremely improbable at EPR frequencies between 200 MHz and 1 THz.

tra. If it is included it is usually assumed to be identical for all transitions. In this case, the broadening is added to the stick spectrum by convolution (see Section 3.3) with a Lorentzian.

2.3.2 Inhomogeneous broadening

EE terms The assumption that all spin systems in a sample can be modelled by the same set of spin Hamiltonian parameters is hardly ever applicable to solid-state powder EPR spectra. There are three effects responsible. First, spin systems interact through space, since they are not infinitely apart from each other. System A feels the presence of system B via the EE term in the Hamiltonian. Since the neighbouring spin systems are not identically placed for all systems, the interaction parameter is distributed. All resonance lines in the spectrum broaden.

HF terms Second, hyperfine couplings in and around a single spin system are too small and too many to be resolvable. The total effect is a broadening of the spectral line shape.

Strains Third, even if more or less magnetically remote from other spin systems, a spin system might encounter slightly different molecular environments depending on structural strains acting on the molecule from the host lattice (solvent). These strains induce distributions in the spin Hamiltonian parameters which are usually modelled as symmetric Gaussian distributions (see Section 1.3).

Linear approximation If the distribution is small—as it usually is—, the broadening can be linearly approximated. The spread Γ_p of the transition frequency $E_v - E_u$ due to parameter p is proportional to the width σ_p of the parameter distribution

$$\Gamma_p(\Delta_{vu}) = \sigma_p \frac{\partial \Delta_{vu}}{\partial p} = \sigma_p \left[\langle v| \frac{\partial H}{\partial p}|v\rangle - \langle u|\frac{\partial H}{\partial p}|u\rangle \right] \ . \tag{2.56}$$

To obtain the width of the resonance *field* distribution, the $1/g$ factor from Eq. (2.52) has to be included

$$\Gamma_p(B_{vu}) = \frac{\Gamma_p(\Delta_{vu})}{\partial \Delta_{vu}/\partial B} = \sigma_p \frac{\langle v|\partial H/\partial p|v\rangle - \langle u|\partial H/\partial p|u\rangle}{\langle v|G_{zL}|v\rangle - \langle u|G_{zL}|u\rangle} \ . \tag{2.57}$$

Limits If $\Delta_{vu}(B)$ is not linear, this approximation breaks down and a numerical integration has to be performed. Line shapes will be asymmetric in field domain, if they are symmetric in frequency domain, as has been pointed out repeatedly [Pil90, Poo99]. However, if the distribution in p is large, then the assumption of a symmetric distribution in frequency domain is not valid either. If strains originate from structural variations, the correlation of the distributions in different spin Hamiltonian parameters has to be taken into account [Hag85b].

Strains Most commonly, strain distributions of g and A principal values are used in simulations. For high-spin systems, distributions in D and E (see Eq. (1.16)) or alternatively in D and E/D are used.

2.4 ENDOR peaks

2.4.1 Resonance positions

From the computational point of view, the cw ENDOR experiment is the simplest of all EPR experiments. At a constant static field B_0 (along z_L), two frequencies are simultaneously applied to the sample, a microwave frequency ν with field $B_1(t)$ along x_L, exciting EPR transitions, and a radio frequency ν_{rf} with field $B_2(t)$ along y_L, inducing transitions between nuclear levels; ν_{rf} is swept. Resonances occur when ν_{rf} hits the energy difference of two states

$$\nu_{rf} = \Delta_{vu} = E_v - E_u \ . \tag{2.58}$$

Hence, only one diagonalisation is necessary for the computation of all peak positions of an ENDOR spectrum for a given orientation of the paramagnetic centre.

2.4.2 Transition intensities

ENDOR transition intensities are more complicated than their cw EPR counterparts. The cw ENDOR experiment is a steady-state experiment, and the Liouville-von Neumann equation (Eq. (2.65)) ought to be solved for that case. The approaches used are much simpler, though. Usually the effect of the balance of relaxation rates is neglected. Instrumental effects arising from the properties of the rf excitation circuit are neglected as well.

With these simplifications, the intensity of an ENDOR transition is proportional to the matrix element of the radio-frequency excitation Hamiltonian $H_2 = B_2 G_{xL}$ describing the interaction with the excitation field B_2 *NMR intensity*

$$M_{vu} = \frac{2\pi}{\hbar} B_2^2 |\langle v|G_{xL}|u\rangle|^2 \ . \tag{2.59}$$

Note that G_{xL} contains both the nuclear and the electron Zeeman interaction. The first describes the pure NMR transition rate, the latter is responsible for the so-called hyperfine enhancement: Since the unpaired electron is also effected by B_2, its magnetic moment gives rise to an additional oscillating field acting on the nucleus.   *Hyperfine enhancement*

An ENDOR peak has only non-zero intensity when the microwave frequency ν hits an EPR transition connected with one of the two nuclear states $|u\rangle$ and $|v\rangle$. The ENDOR intensity is hence also proportional to the sum over all EPR transition moments weighted by the excitation bandwidth Γ_{mw} of the *microwave*   *EP excitation*

$$\alpha_{vu}(\Gamma_{mw}) = \sum_q \left[f(\Delta_{qu} - \nu_{mw}, \Gamma_{mw})\langle q|G_{xL}|u\rangle^2 + f(\Delta_{qv} - \nu_{mw}, \Gamma_{mw})\langle q|G_{xL}|v\rangle^2 \right] . \tag{2.60}$$

f indicates a Gaussian line shape. In numerical simulations, Eq. (2.60) was first used in the program MAGRES [Kei87].

Orientation
selection

In a powder sample, α_{vu} can be strongly orientation dependent, if there are large anisotropic interactions affecting EPR transitions. This is the source of strong orientation selection in ENDOR spectra of many paramagnetic centres. The resulting complications for numerical simulations are dealt with in Section 4.5.

EPR
broadening

The above formula is valid for stick EPR spectra. If inhomogeneous broadening is present, it effectively enlarges the excitation bandwidth. Instead of Γ_{mw},

$$\Gamma_{\mathrm{tot}} = \sqrt{\Gamma_{\mathrm{mw}}^2 + \Gamma_{\mathrm{inhom}}^2} \tag{2.61}$$

is used. The excitation range of the incident radio frequency is assumed to be zero at this stage and is later added in the form of a Gaussian convolution of the ENDOR spectrum.

Pulse ENDOR

In pulse ENDOR, line intensities depend on experimental settings. The Mims ENDOR experiment is hyperfine selective, since the signal from a nucleus depends on the time τ between the first two pulses in the sequence, adding an additional factor [Sch01]

$$F = \frac{1}{4}[1 - \cos(a_{\mathrm{iso}}\tau)] \ . \tag{2.62}$$

This causes blind spots in the ENDOR spectrum. In the Davies ENDOR experiment signals due to nuclei with small hyperfine couplings are suppressed depending on the length t_1 of the first pulse

$$F = \frac{\sqrt{2}\,\eta_{\mathrm{S}}}{\eta_{\mathrm{S}}^2 + 1/2} \quad \text{with} \quad \eta_{\mathrm{S}} = \frac{a_{\mathrm{iso}}t_1}{2\pi} \ . \tag{2.63}$$

In experiments the pulse sequences usually are set up to give approximately constant F for the ENDOR spectral region of interest, so that Eq. (2.62) and Eq. (2.63) can be neglected.

Total

If necessary, temperature effects are included according to Eq. (2.55), so that the overall intensity is

$$A_{vu} = (\beta_v - \beta_u)F\alpha_{vu}M_{vu} \ . \tag{2.64}$$

2.5 Pulse EPR peaks

In this and the next subsection, the computation of pulse EPR peak positions and amplitudes is discussed. This section is concerned with the basic theory, whereas the next one discusses topics relevant for an implementation.

Current
state

Pulse EPR simulations are substantially more complicated than simulations of cw EPR or ENDOR spectra. Many computations are based on the original formulas derived by Mims and others [Sch01]. Their applicability is limited to special experiments (two-pulse and three-pulse ESEEM, HYSCORE) and to special

systems (isotropic g, $S = 1/2$). Recently there have been efforts to improve performance [Sha98, Szo98] and to extend their scope [Mád02]. But pure numerical pulse EPR simulations are still too limited and too slow to be routinely usable for fitting experimental spectra. All ESEEM simulations are currently limited to spin systems with $S = 1/2$, although work on $S \geq 1$ computations is under way [Nob02a] and the underlying theory is being worked out [Ast02, Ben02].

Most pulse EPR and NMR simulations in general have been performed in time domain so far [Hoh99, Nic00]. Frequency domain methods have the potential of being much faster [Szo98, Bak00], but general formulas for arbitrary pulse sequences have not been derived. In the following we introduce a very general and efficient frequency-domain technique, yielding pulse EPR peak positions and amplitudes.

TD vs. FD

2.5.1 Basic theory

Any pulse EPR spectrum computation method starts from the basic quantum dynamics (Liouville-von Neumann) equation[1]

Master equation

$$\dot{\sigma}(t) = -\mathrm{i}[H(t), \sigma(t)] \qquad (2.65)$$

and its solution

$$\sigma(t) = U(t, t_0)\sigma(t_0)U^\dagger(t, t_0) \quad \text{with} \quad \mathrm{i}\dot{U}(t, t_0) = H(t)U(t, t_0) \qquad (2.66)$$

with the spin density operator $\sigma(t)$ and a possibly time-dependent spin Hamilton operator $H(t)$. If the Hamiltonian H is time-independent, the equation can be integrated easily with

$$U(t, t_0) = \mathrm{e}^{-\mathrm{i}H(t-t_0)} \ . \qquad (2.67)$$

$\sigma(t_0)$ in Eq. (2.66) denotes the density operator at the beginning of the experiment. There the spin system is usually in thermal equilibrium $\sigma(t_0) = \sigma_{\mathrm{eq}}$, and the density operator is given by the Boltzmann distribution

Boltzmann distribution

$$\sigma_{\mathrm{eq}} = \frac{\exp(-\hbar H/k_\mathrm{B}T)}{\mathrm{tr}[\exp(-\hbar H/k_\mathrm{B}T)]} \qquad (2.68)$$

with temperature T, the Boltzmann constant k_B and the static Hamiltonian H. There are no coherences at thermal equilibrium, i.e. the phases of different spins are uncorrelated. The trace expression in Eq. (2.68) is slightly larger than the state space dimension N.

Assuming $|\hbar H/k_\mathrm{B}T| \ll 1$ and using the polynomial expansion $\exp(X) = \sum_{k=0}^{\infty} X^k/k!$ we can approximate σ_{eq} by

Linear term

$$\sigma_{\mathrm{eq}} \approx \frac{\mathbb{1}_N - \hbar H/k_\mathrm{B}T}{\mathrm{tr}(\mathbb{1}_N - \hbar H/k_\mathrm{B}T)} \ , \qquad (2.69)$$

---

[1] In this and the following section we will use H in *angular* units, see p. 5.

since higher-order terms in X are too small to contribute significantly. This is the so-called high-temperature approximation.

Polarisation only
The trace expression in the denominator of Eq. (2.69) is N, since $\text{tr}(H) = 0$ for the usual spin Hamiltonians in EPR. The constant in the enumerator is irrelevant to any EPR experiment. So we need only the linear part

$$\sigma_{\text{eq}}^{\text{pol}} \approx -\frac{1}{N}\frac{\hbar H}{k_{\text{B}}T} \; . \tag{2.70}$$

The error of this approximation increases with higher field, lower temperature and higher spins.

Exceptions
There are some cases for which $\sigma(t_0) \neq \sigma_{\text{eq}}$. If the repetition rate of the experiment is very high, some coherences or polarisations might not have decayed after the end of the previous pulse sequence, and the density operator might not have reached thermal equilibrium. For example, these effects have to taken into account when simulating pulse ENDOR spectra at high fields and low temperatures (e.g. W band at $T \leq 5\,\text{K}$), where non-equilibrium polarizations on nuclear transitions can invert spectral lines [Epe01]. Other situations include spin-correlated radical pairs and excited triplet states.

Pulse sequence
A pulse EPR experiment consists of a sequence of mw or rf pulses separated by free evolution periods. After the last pulse and an additional time delay there appears an echo (see Figure 2.8). Its amplitude is a function of the position, the length, the power and the phase of the pulses. Several pulse or interpulse delays are usually incremented or decremented in a pulse EPR experiment. The echo amplitude as a function of these delay times then constitutes the pulse EPR signal.

Propagators
The free evolution periods are described by the propagator

$$U_{\text{free}} = \exp(-\text{i}H_{\text{free}}t) \; , \tag{2.71}$$

with the mw-free static spin Hamiltonian H_{free}. The pulse propagators are

$$U_{\text{pulse}} = \exp(-\text{i}(H_{\text{free}} + H_{\text{mw}})t) \; . \tag{2.72}$$

with the additional mw excitation Hamiltonian H_{mw} in an appropriate frame that removes the time dependence of H_{mw} in the laboratory frame (see next section). If the time-dependence cannot be removed, U_{pulse} has to be calculated by numerical integration as detailed in Section 2.6.3.

Block propagators
If all propagators representing pulses and interpulse delays which remain constant during the experiment are collected into pulse blocks represented by single propagators P [Sha98], a pulse sequence can be generally described by the total propagator

$$Q(\boldsymbol{t}) = P^{(M+1)} \prod_{k=M}^{1} \exp(-\text{i}H^{(k)}t_k)P^{(k)} \; , \tag{2.73}$$
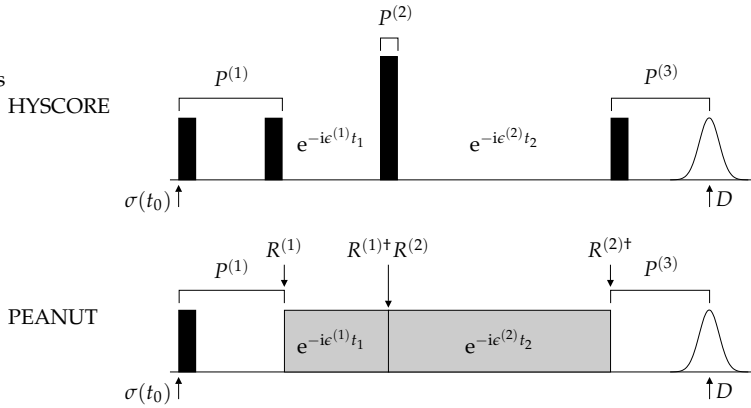
Figure 2.8: Propagators and basis transforms for two 2D pulse EPR experiments. Identity operators ($R^{(1)}$ and $R^{(2)}$ in HYSCORE and $P^{(2)}$ in PEANUT) are not shown.

evoluting the density operator according to

$$\sigma(t) = Q(t)\sigma(t_0)Q^{\dagger}(t) \; . \tag{2.74}$$

The vector $t = (t_1, \ldots, t_M)^{\mathrm{T}}$ collects all evolution time variables. The start and end indices for the sum indicate a time-ordered product, which is essential, since propagators for different periods usually do not commute.

In most pulse EPR experiments the variable evolution periods are governed by the mw-free static Hamiltonian, but sometimes pulse durations are incremented as well, as in decoupling and nutation experiments [Sch01]. The way in which t is varied in an experiment is determined by its incrementation scheme. Either all M components of t are changed independently, or some of them are related. For a given pulse sequence, different incrementation schemes yield different spectra [Hub96]. Hence, the pulse sequence and the incrementation scheme are two quite separate characteristics of a pulse EPR experiment [Pon97].

Incremen-tation

The density operator fully describes the state of the ensemble of spin systems at any time, and at the end of the pulse sequence the expectation value of an observable D (usually the magnetisation along x_{L}) can be obtained from

Observables

$$s(t) = \langle D \rangle(t) = \mathrm{tr}\left[\sigma(t)D\right] = \mathrm{tr}\left[Q(t)\sigma(t_0)Q^{\dagger}(t)D\right] \; . \tag{2.75}$$

2.5.2 FD formulas

Starting from the basic equations above we can now derive general formulas for pulse EPR peaks. In Eq. (2.73) all variable evolution period operators are transformed to their respective eigenbases by replacing the propagator exponentials by their diagonal decompositions

Propagator eigenbases

$$\exp(-iH^{(k)}t_k) = R^{(k)}\exp(-i\epsilon^{(k)}t_k)R^{(k)\dagger} \; , \tag{2.76}$$

where ϵ is the Hamiltonian H in its diagonal representation, still in angular frequency units. The unitary transformation matrices R are joint with the adjacent pulse block matrices in Eq. (2.73) so that $\tilde{P}^{(k)} = R^{(k)\dagger} P^{(k)} R^{(k-1)}$ (for $2 \leq k \leq M$), $\tilde{P}^{(1)} = R^{(1)} P^{(1)}$ and $\tilde{P}^{(M+1)} = P^{(M+1)} R^{(M)\dagger}$, giving

$$
Q(t) = P^{(M+1)} \prod_{k=M}^{1} R^{(k)} \exp(-i\epsilon^{(k)} t_k) R^{(k)\dagger} P^{(k)}
$$

$$
= \tilde{P}^{(M+1)} \prod_{k=M}^{1} \exp(-i\epsilon^{(k)} t_k) \tilde{P}^{(k)} \; . \tag{2.77}
$$

(see illustrative examples in Figure 2.8). This full propagator eigenbasis representation has the advantage that all variable propagator exponentials are diagonal. The number of scalar multiplications needed to compute Q for any given t is thus minimised in this representation.

Scalar level   Inserting the new expression for $Q(t)$ into Eq. (2.75) and going to a matrix representation, the equation reads on a scalar level

$$
s(t) = \sum_{\xi} \left[Z_{\xi} \prod_{k=1}^{M} \exp\left(i\omega_{\xi}^{(k)} t_k \right) \right] \tag{2.78}
$$

with the complex amplitudes

$$
Z_{\xi} = \Delta_{j_M i_M} \left(\prod_{k=M-1}^{1} T_{i_k i_{k-1}}^{(k)} \right) \Sigma_{i_1 j_1} \left(\prod_{k=1}^{M-1} T_{j_{k-1} j_k}^{(k)\dagger} \right) \tag{2.79}
$$

and the abbreviated matrices

$$
\Sigma = \tilde{P}^{(1)} \sigma(t_0) \tilde{P}^{(1)\dagger} \qquad \Delta = \tilde{P}^{(M+1)\dagger} D \tilde{P}^{(M+1)} \qquad T^{(k)} = \tilde{P}^{(k+1)} \; . \tag{2.80}
$$

Σ is the density matrix at the start of the first incrementation period, Δ denotes the detection operator back-evoluted to the end of the last incrementation period M, and $T^{(k)}$ is the propagator between periods k and $k+1$. $T^{(k)}$ transfers and mixes coherence and polarisation amplitudes between the evolution periods k and $k+1$. ξ is an index for the magnetisation transfer pathway specified by $(i_1, j_1; \ldots; i_M, j_M)$, and the angular frequencies ω are differences of propagator Hamiltonian eigenvalues

$$
\omega_{\xi}^{(k)} = 2\pi \nu_{\xi}^{(k)} = \epsilon_{j_k j_k}^{(k)} - \epsilon_{i_k i_k}^{(k)} \; . \tag{2.81}
$$

Fourier   Using the vector $\boldsymbol{\omega}_{\xi} = (\omega_{\xi}^{(1)}, \ldots, \omega_{\xi}^{(M)})^{\mathsf{T}}$, Eq. (2.78) can be compactly written
transform   as a sum of exponentials

$$
s(t) = \sum_{\xi} Z_{\xi} \exp\left(i\boldsymbol{\omega}_{\xi}^{\mathsf{T}} t \right) \; . \tag{2.82}
$$

Table 2.2: Amplitude expressions for pulse EPR pulse sequences

Periods	Amplitude[a] Z_ξ
1	$\Sigma\Delta$
2	$\Sigma\Delta T^{(1)}T^{(1)\dagger}$
3	$\Sigma\Delta T^{(1)}T^{(1)\dagger}T^{(2)}T^{(2)\dagger}$
4	$\Sigma\Delta T^{(1)}T^{(1)\dagger}T^{(2)}T^{(2)\dagger}T^{(3)}T^{(3)\dagger}$
m	$\Sigma\Delta\prod_{k=1}^{m-1}T^{(k)}T^{(k)\dagger}$

[a] Indices have been omitted and are understood to be as in Eq. (2.79).

The M-dimensional Fourier transform of this signal is

$$\mathcal{FT}[s(\boldsymbol{t})] = S(\boldsymbol{\omega}) = \sum_\xi Z_\xi \delta\left(\boldsymbol{\omega} - \boldsymbol{\omega}_\xi\right) \ . \tag{2.83}$$

Eq. (2.83) describes a collection of peaks with positions $\boldsymbol{\omega}_\xi$ and amplitudes Z_ξ.

Whereas in conventional TD methods Eq. (2.74) and Eq. (2.75) are evaluated for each $\boldsymbol{t}$ separately, the essence of the FD approach is the direct calculation of the Fourier transform of $s(t)$ in the form of a list of spectral peak positions $\boldsymbol{\omega}_\xi$ and amplitudes Z_ξ using Eq. (2.79) and Eq. (2.81). Explicit expressions for Z_ξ are listed in Table 2.2. For an M-dimensional experiment, the peak amplitude consists of a product of $2M$ complex numbers.

FD approach

The evaluation of Eq. (2.79) and Eq. (2.81) can be performed by a recursive function, which starts with a certain element $Z^{(1)} = \Sigma_{i_1 j_1}$ and adds the first transfer amplitudes $T^{(1)}$ to give $Z^{(2)} = T^{(1)}_{i_2 i_1} Z^{(1)} T^{(1)\dagger}_{i_2 i_1}$. Then it calls itself recursively with $Z^{(2)}$ instead of $Z^{(1)}$ and so on, until Δ is reached and the final amplitude can be computed. For a given $Z^{(k-1)}$, the routine loops over all new indices i_k and j_k in $Z^{(k)}$. The peak positions are built up in the same way using the position components $\omega^{(k)}_{i_k j_k}$. The recursive nature of the computation results in much fewer multiplications compared to the separate evaluation of Z_ξ and $\boldsymbol{\omega}_\xi$ for all ξ. In addition, an elegant thresholding scheme can be implemented, as will be shown in Section 2.8.2.

Recursive computation

In a pseudocode notation the main loop calls the function `ComputePeak` for each element of the starting density matrix `Sigma0`

Functions

```
for i = 1 to N   // loop over rows
  for j = 1 to N // loop over columns
    ComputePeak(0,Sigma0(i,j),0,i,j)
  end
end
```

The recursive function is as follows

```
function ComputePeak(omega,Z,k,i0,j0)
omega += epsilon(k)(j0,j0) - epsilon(k)(i_0,i_0)
if k == M-1      // final Z can be computed
  Zfinal = Delta(j_0,i_0)*Z
  AddToList(omega,Zfinal)
else  // advance one period and call ComputePeak
  for i = 1 to N            // left index
    for j = 1 to N          // right index
      Znew = T(k)(i,i0)*Z*conj(T(k)(j,j0))
      ComputePeak(omega,Znew,k+1,i,j)
    end
  end
end
```

For experiments with one (two) variable evolution period(s), the recursive approach needs 1 (3) multiplication(s) per peak, just as the separate computation of all peaks. For three variable evolution periods, it needs $3 + 2/N^2$ instead of 5 multiplications per peak, thus saving between 37.5% and 40%. The major advantage of the recursive approach, however, is the possibility of adaptive thresholding, which is discussed in Section 2.8.2.

Hermitian detector

If the detection operator D is Hermitian, an additional symmetry in Eq. (2.78) can further simplify the computational task. The signal $s(t)$ will be real in this case, and there will be pairs of peaks with positions $\omega_{\xi_1} = -\omega_{\xi_2}$ with transfer pathways ξ_1 and ξ_2 having complex conjugate amplitudes $Z_{\xi_1} = Z_{\xi_2}^*$. For these two peaks only one amplitude has to be explicitly calculated. This reduces the number of amplitudes to compute by another factor of two.

2.5.3 Properties

The quite general formulas above clearly illustrate some properties of pulse EPR spectra. The peak amplitudes in Eq. (2.79) contain generation, transfer and detection efficiencies. If different $H^{(k)}$ govern the various variable evolution periods k, the transfer amplitudes contain the basis transforms, too. For a given set of variable evolution times, that is, for a given $Q(t)$, the expression for the peak amplitudes does not depend on the incrementation scheme. The number of different matrix elements entering a peak's amplitude expression increases with the number of incremented evolution times. So the amplitude expression for a two-pulse ESEEM signal is as complicated as that for a HYSCORE signal, because they contain the same number of variable propagators.

t constraints

Quite often different t_k are interdependent in a pulse EPR experiment, e.g. $t_1 = t_2$ in two-pulse ESEEM, so that one final spectral dimension results from the simultaneous evolution of more than one propagator. The dimension of the spectrum d is then lower than the number of variable propagators M. In such cases, there appear combination frequencies. The two-pulse ESEEM experiment is the

Table 2.3: Pulse EPR incrementation schemes and peak positions

Type	d	N	t constraints	Peak position ω_ξ	Phase
(1a)	1	1	—	$\omega_\xi^{(1)}$	1
(1b)		2	$t_2 = t_1$	$\omega_\xi^{(1)} + \omega_\xi^{(2)}$	1
(1c)		2	$t_2 = T - t_1$	$\omega_\xi^{(1)} - \omega_\xi^{(2)}$	$e^{i\omega_\xi^{(2)}T}$
(2a)	2	2	—	$(\omega_\xi^{(1)}, \omega_\xi^{(2)})$	1
(2b)		3	$t_3 = t_1$	$(\omega_\xi^{(1)} + \omega_\xi^{(3)}, \omega_\xi^{(2)})$	1
(2c)		3	$t_3 = t_2$	$(\omega_\xi^{(1)}, \omega_\xi^{(2)} + \omega_\xi^{(3)})$	1
(2d)		4	$(t_4, t_3) = (t_1, t_2)$	$(\omega_\xi^{(1)} + \omega_\xi^{(4)}, \omega_\xi^{(2)} + \omega_\xi^{(3)})$	1
(2e)		4	$(t_4, t_2) = (t_3, t_1)$	$(\omega_\xi^{(1)} + \omega_\xi^{(2)}, \omega_\xi^{(3)} + \omega_\xi^{(4)})$	1

most prominent one. If the sum of two components of t is kept constant, the peak amplitude expressions acquire an additional phase factor, like in PEANUT. The most common incrementation schemes are summarised in Table 2.3. For a given M the peak positions depend on d and on the constraints, whereas the amplitude expressions are independent of d (Table 2.2). All common pulse EPR experiments fall into a handful of sequence and incrementation scheme categories as listed in Table 2.4.

As a concrete case, we examine the expressions for cross peaks in HYSCORE spectra. These cross peaks occur in pairs with positions

Cross peaks

$$\boldsymbol{\omega}_a = (\epsilon_{j_1 j_1} - \epsilon_{i_1 i_1}, \epsilon_{j_2 j_2} - \epsilon_{i_2 i_2})^{\mathrm{T}} \qquad \boldsymbol{\omega}_b = (\epsilon_{j_2 j_2} - \epsilon_{i_2 i_2}, \epsilon_{j_1 j_1} - \epsilon_{i_1 i_1})^{\mathrm{T}} \qquad (2.84)$$

and amplitudes

$$Z_a = \Delta_{j_2 i_2} T_{i_2 i_1} \Sigma_{i_1 j_1} T_{j_1 j_2}^\dagger \qquad Z_b = \Delta_{j_1 i_1} T_{i_1 i_2} \Sigma_{i_2 j_2} T_{j_2 j_1}^\dagger \; . \qquad (2.85)$$

This shows that the amplitudes are physically different even when relaxation is neglected. The resulting symmetry is significant in some experimental situations, but is still not fully understood.

Peak positions and amplitudes can be interpolated over any experimental parameter. This is discussed in Section 2.7.

Interpolation

The formulas given above are also applicable for pulse ENDOR experiments. The amplitudes of a Davies ENDOR experiment are equal to the coherence transfer amplitudes of an inversion recovery experiment for a certain t as a function of the frequency of the additional rf pulse. Mims ENDOR signals are obtained along the same lines from three-pulse coherence transfer amplitudes.

Pulse ENDOR

In most situations, the pulse EPR experiment is performed with a set of pulse sequences differing in the relative phases between pulses, but having the same pulse and interpulse delay times. The resulting signals have peaks at the same

Phase cycles

Table 2.4: Classification of common pulse EPR experiments

Type [a]	Experiments
(1a)	3-pulse ESEEM, inversion recovery
(1b)	2-pulse ESEEM, 1D CP
(1c)	PEANUT
(2a)	HYSCORE, DONUT-HYSCORE
(2b)	2D 3-pulse ESEEM
(2d)	2D CP
(2e)	SIFTER

[a] see Table 2.3.

positions, but with different amplitudes. By linearly combining the signals, unwanted components such as echo crossings can be removed from the signal. In the FD approach presented here, this linear combination can be performed at the level of Z_ξ. The signals $s(t)$ for the different cycles do not have to be constructed separately.

2.5.4 Inhomogeneities

Inhomo-geneities

The shape and the amplitude of an electron spin echo strongly depends on the spectrum within the excitation window of the first pulse in the sequence. In solid state EPR, small or unresolved hyperfine couplings and distributions in some spin Hamiltonian parameters are always present, so that the spectral line shape within the excitation range of the first pulse is more or less constant. In this case the echo has the form of a Gaussian with amplitudes modulated due to refocussed nuclear coherence transfer echoes.

Integration

In order to accurately simulate an echo signal, these distributions have to be integrated. Commonly an additional "offset" term

$$H_{\mathrm{inhom}} = \omega_{\mathrm{inhom}} S_{\mathrm{zL}} \tag{2.86}$$

is added to the spin Hamiltonian, and the signal is integrated over a Gaussian distribution of ω_{inhom} centred at $\omega_{\mathrm{inhom}} = 0$. For the computation of single-crystal pulse EPR signals this is essential. For powder signals it can be skipped, since the orientational distribution already serves the purpose. However, care must be taken to use the number of orientations sufficiently high to achieve proper amplitude integration.

Offset

In some cases like the three-pulse ESEEM experiment, pulses on the centre of the single-orientation EPR spectrum do not give an echo [Sch01]. Consequently, an offset integration has to be performed even for powder samples.
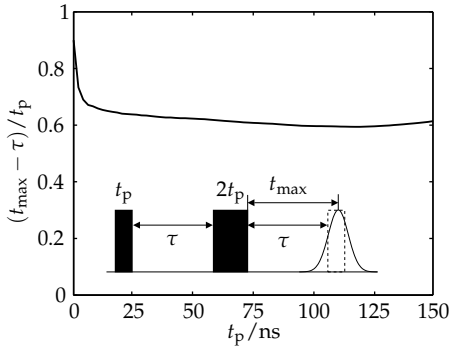
Figure 2.9: Position of the two-pulse echo maximum in dependence of the length of the first pulse. Parameters: $\tau = 300\,\text{ns}$, $\Gamma_{\text{FWHH}} = 10\,\text{MHz}$, pulse angles $\pi/2$ and π. The slight rise of the curve in the region $t_p > 125\,\text{ns}$ is due to the underlying FID of the second pulse.

2.5.5 Detection window

The echo position depends on the length of the first excitation pulse in the se- — Echo position
quence. As an example, we consider the two-pulse echo experiment. In the nar-
row line limit, i.e. when the EPR line width is much smaller than the excitation
range of the pulses, the echo maximum occurs at time τ after the last pulse. If
the line width is similar or larger than the pulse excitation width, then the echo
maximum is delayed in time by around $0.6t_p$ as illustrated in Figure 2.9. This was
first noticed in one of the early papers on ESEEM [Mim65], where the approxim-
ate value of $\frac{1}{2}t_p$ was given. If the static Hamiltonian is neglected during the pulse
periods, the echo will always peak exactly at time τ after the end for the second
pulse.

In simulations, the correct position has to be determined either from the exper- — Simulations
imental settings, by simulating the time trace of the magnetisation or by using
pre-computed numerical data like in Figure 2.9. Up to now, this effect has not
been taken into account [Szo98, Mád02] and a single-point detection at time τ
after the end of the last pulse was used, resulting in simulated spectra which
behave unexpectedly except in the simplest of all cases.

In experiments, the detection window covers a significant part of the echo — Detection
shape. It is centred at the echo maximum and its width is adjusted so as to max- window
imise the S/N ratio without loss of resolution in the modulation amplitude of the
signal. Sometimes an off-centre setting can enhance the resolution, since nuclear
coherence transfer echoes do no necessarily occur at the echo maximum.

2.6 Computing propagators

The method presented in the previous section is independent of the method the
different propagators are arrived at. In this section we discuss some techniques
to compute propagators.

For small hyperfine interactions and not too anisotropic $S = 1/2$ systems, the
rotating frame approach is the best choice (Section 2.6.1), since it effectively re-

43

moves the time-dependence of the pulse Hamiltonian. On the other hand, for electron spins $S \geq 1$ a treatment in the laboratory frame is mandatory (Section 2.6.2). In this frame, the computation of the propagators is more complicated, since the pulse Hamiltonians are time dependent. We will address this problem in Section 2.6.3.

In the laboratory frame, the frequency-domain approach outlined in Section 2.5 can only be applied if the increments in the pulse sequence are multiples of the detection frequency. Otherwise the phase of propagators and of the signal change with each increment.

2.6.1 The rotating frame and its limits

Most experiments can be described without gross errors in the rotating frame [Sch01]. This is valid for $S = 1/2$, isotropic g and A small compared to the electron Zeeman interaction. In this case the electron spin is almost entirely governed by Zeeman interaction, and the off-diagonal hyperfine coupling terms are very small. Then one can go to the eigenbasis of the electron, neglect these small terms and get rid of the time dependence of the excitation operator [Sch01].

General transformation
The rotating frame is a special case of an interaction frame. In general, one applies a time-dependent unitary transformation $U(t) = \exp(iH_{\mathrm{Tr}}t)$ based on some Hamiltonian H_{Tr} to the Liouville-von Neumann equation

$$U^\dagger \dot\sigma U = -iU^\dagger[H,\sigma]U = -i[U^\dagger HU, U^\dagger \sigma U] = -i[H_{\mathrm{R}}, \sigma_{\mathrm{R}}] \qquad (2.87)$$

with the transformed operators $\sigma_{\mathrm{R}} = U^\dagger \sigma U$ and $H_{\mathrm{R}} = U^\dagger HU$. The resulting transformed equation looks similar to the original one, but contains a different effective Hamiltonian

$$\dot\sigma_{\mathrm{R}} = -i[H_{\mathrm{R}}^{\mathrm{eff}}, \sigma_{\mathrm{R}}] \quad \text{with} \quad H_{\mathrm{R}}^{\mathrm{eff}} = U^\dagger HU - iU^\dagger \dot U . \qquad (2.88)$$

Expectation values are independent of the frame used for the representation of the operators

$$\langle D \rangle = \mathrm{tr}(\sigma D) = \mathrm{tr}(U^\dagger \sigma U U^\dagger DU) = \mathrm{tr}(\sigma_{\mathrm{R}} D_{\mathrm{R}}) . \qquad (2.89)$$

For the rotating frame transformation, $U(t) = \exp(i2\pi\nu_{\mathrm{mw}}S_{\mathrm{zL}}t)$, with the spectrometer frequency ν_{mw}. The detector is M_{x}, the magnetisation along the x axis of the rotating frame. For quadrature detection M_{y} has to be computed as well. The effect of phase-sensitive detection is already taken into account.

In the case of a significant zero-field splitting or hyperfine interactions (which cause a zero-field splitting as well), the transformation to the rotating frame gives significant time-dependent terms, which cannot be neglected.

Ideal pulses
If the rotating frame approach is applicable, it removes the time dependence from the pulse Hamiltonians. Another simplifying concept makes used of "ideal pulses" where the static Hamiltonian is neglected during pulses. In NMR pulses

are often short compared to the largest interaction in the spin Hamiltonian, hence this can be a good approximation. In EPR, however, the applicability of this simplification is more restricted. Technically achievable pulse strengths (around 5 ns for a $\pi/2$ pulse on an $S = 1/2$ system with $g = 2$) are not orders of magnitude larger than hyperfine interactions, so that the ideal pulse approximation is only viable for the strongest pulses. As soon as softer ones are used (e.g. 50 ns for a $\pi/2$ pulse), as required in many pulse EPR experiments, the static Hamiltonian has significant influence.

If the ideal pulse approximation can be applied, it simplifies the computation of the matrix exponentials for the pulse propagators, especially for a electron-nuclear system with many nuclei. In this case the ideal pulse Hamiltonian contains only the mw excitation part

$$H_1 = 2\pi\nu_1 S_\mathrm{x} \otimes \mathbb{1}_\mathrm{n} \tag{2.90}$$

Factoring

with the pulse strength ν_1, an operator S_x acting only in the electron subspace and the identity operator $\mathbb{1}_\mathrm{n}$ in the full nuclear product space

$$\mathbb{1}_\mathrm{n} = \mathbb{1}_{2I_1+1} \otimes \mathbb{1}_{2I_2+1} \otimes \cdots . \tag{2.91}$$

It is easy to show[1] that the pulse propagator with the Hamiltonian H_P can be factored

$$\mathrm{e}^{-\mathrm{i}cS \otimes \mathbb{1}_\mathrm{n}} = \mathrm{e}^{-\mathrm{i}cS} \otimes \mathbb{1}_\mathrm{n} \tag{2.92}$$

independent of the basis in which the operators are represented.

The use of ideal pulses tremendously speeds up the computation of pulse propagator exponentials. There is, however, a major drawback. The most interesting peaks in many-nuclei systems where the factoring is particularly useful are combination peaks between frequencies of the same and of different nuclei. Unfortunately, the amplitudes of exactly these combination peaks are not well approximated by the ideal pulse approach. A full treatment with the inclusion of the static Hamiltonian during the pulses is mandatory.

Limits

2.6.2 The laboratory frame

If the time dependencies in the rotating frame cannot be neglected, the simulation has to be performed in the laboratory frame. It has been suggested to use an interaction frame [Oli96], but this does not reduce the computational cost. In the laboratory frame the pulse propagators are time dependent and have to be integrated numerically. This is discussed in Section 2.6.3.

The form of the detection operator in the laboratory frame deserves some attention. A spectrometer picks up the signal induced in a coil by the x component

Detection

---

[1] With $\mathbb{1}^k = \mathbb{1}$ the proof is as follows: $\mathrm{e}^{A \otimes \mathbb{1}} = \sum_k \frac{1}{k!} A^k \otimes \mathbb{1}^k = \left(\sum_k \frac{1}{k!} A^k \right) \otimes \mathbb{1} = \mathrm{e}^A \otimes \mathbb{1}$ $\quad \square$

of the precessing magnetisation, so in the laboratory frame it is proportional to $\mathrm{d}\langle M_{\mathrm{x}}\rangle/\mathrm{d}t$.

$$s_{\mathrm{mw}}(t) = \frac{\mathrm{d}\langle M_{\mathrm{x}}\rangle}{\mathrm{d}t} = \frac{\mathrm{d}}{\mathrm{d}t}\mathrm{tr}\left[M_{\mathrm{x}}\sigma(t)\right] . \tag{2.93}$$

In the detector this microwave signal is mixed with the reference signal at frequency ω_{r}, yielding

$$s(t) = 2\cos(\omega_{\mathrm{r}}t + \phi_{\mathrm{r}})s_{\mathrm{mw}}(t) . \tag{2.94}$$

For quadrature detection, the original signal $s_{\mathrm{mw}}(t)$ is split and mixed separately with the reference signal at orthogonal phases. The signal $s(t)$ in the rf range goes through a low-pass filter (usually around 50 MHz) before it is digitised.

Detection operator
Now we want to compute explicitly $s(t)$ at the detection time, assuming that around this time the governing Hamiltonian is time-independent. For convenience we set the origin of the time scale to the detection time, i.e. $t = 0$ at detection time. The entire pulse sequence is thus in the region $t < 0$. Using the Liouville-von Neumann equation, we get

$$\begin{aligned} s_{\mathrm{mw}}(t,\tau) &= \frac{\mathrm{d}}{\mathrm{d}t}\mathrm{tr}\left[M_{\mathrm{x}}\sigma(t,\tau)\right] = \mathrm{tr}\left[M_{\mathrm{x}}\dot{\sigma}(t,\tau)\right] = \mathrm{tr}\left[\mathrm{i}M_{\mathrm{x}}\sigma(t,\tau)H - \mathrm{i}M_{\mathrm{x}}H\sigma(t,\tau)\right] \\ &= \mathrm{tr}\left[\mathrm{i}HM_{\mathrm{x}}\sigma(t,\tau) - \mathrm{i}M_{\mathrm{x}}H\sigma(t,\tau)\right] = \mathrm{tr}\left\{\mathrm{i}[H,M_{\mathrm{x}}]\sigma(t,\tau)\right\} \\ &= \mathrm{tr}[D\sigma(t,\tau)] . \end{aligned} \tag{2.95}$$

In other words, the derivative in Eq. (2.93) implies that the detection operator is not M_{x}, but rather the commutator $\mathrm{i}[H,M_{\mathrm{x}}]$, which is Hermitian if M_{x} and H are Hermitian[1]

$$s_{\mathrm{mw}}(t,\tau) = \mathrm{tr}\left[D\sigma(t,\tau)\right] \quad \text{with} \quad D = \mathrm{i}[H,M_{\mathrm{x}}] . \tag{2.96}$$

If M_{x}, σ and H are expressed in the eigenbasis of H, the above equation is particularly simple on a scalar level. H itself is diagonal and the elements of the detection operator are then

$$D_{kl} = \mathrm{i}(M_{\mathrm{x}})_{kl}(H_{kk} - H_{ll}) = \mathrm{i}(M_{\mathrm{x}})_{kl}\omega_{kl} . \tag{2.97}$$

2.6.3 Integrating propagators

In this subsection we explain how the propagator for a system under influence of a periodic Hamiltonian can be computed numerically. We start with the periodic Hamiltonian

$$H(t) = \sum_k H_k\,\mathrm{e}^{\mathrm{i}k\omega t} \tag{2.98}$$

with period $T = 2\pi/\omega$. Under the influence of this Hamiltonian an initial state $\sigma(t_0)$ evolves to

$$\sigma(t) = U(t,t_0)\sigma(t_0)U^\dagger(t,t_0) , \tag{2.99}$$

---

[1] Proof: $D^{\mathrm{T}} = (\mathrm{i}[H,M_{\mathrm{x}}])^{\mathrm{T}} = \mathrm{i}[M_{\mathrm{x}}^{\mathrm{T}},H^{\mathrm{T}}] = \mathrm{i}[M_{\mathrm{x}}^*,H^*] = -\mathrm{i}[H^*,M_{\mathrm{x}}^*] = (\mathrm{i}[H,M_{\mathrm{x}}])^* = D^* \quad \square$
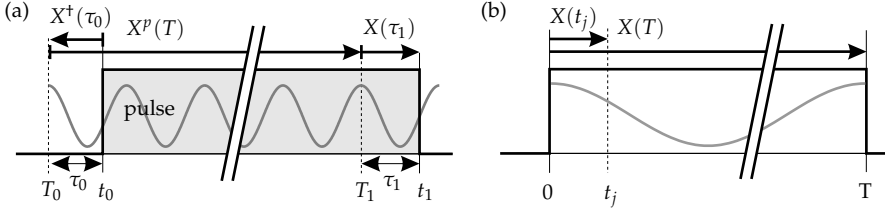
Figure 2.10: Integrating the propagator under a time-dependent Hamiltonian.

where the propagator satisfies (see Eq. (2.66))

$$i\dot{U}(t, t_0) = H(t)U(t, t_0) \ . \tag{2.100}$$

This implies $U(t_0, t_0) = \mathbb{1}_N$. The propagator can be decomposed into two propagators

$$U(t, t_0) = U(t, 0)U^\dagger(t_0, 0) = X(t)X^\dagger(t_0) \ , \tag{2.101}$$

which corresponds to a backward evolution from t_0 to time 0 and a forward evolution to t.

According to the Floquet theorem (see e.g. [Cha98] and references therein), $X(t)$ can be written as

Floquet theorem

$$X(t) = P(t)e^{-i\overline{H}t} \ , \tag{2.102}$$

where $P(t)$ is unitary ($P(t)^{-1} = P(t)^\dagger$) and periodic ($P(t) = P(t + T)$) and $\overline{H}$ is the average Hamiltonian, which is time-independent. For a general propagator this means

$$U(t, t_0) = P(t)e^{-i\overline{H}(t-t_0)}P^\dagger(t_0) = F(t)e^{-i\bar{\epsilon}(t-t_0)}F^\dagger(t_0) \tag{2.103}$$

where we transformed $\overline{H}$ to its eigenbasis without affecting U. $\bar{\epsilon}$ is the diagonal representation of the average Hamiltonian.

$F(t)$ defines a general time-dependent interaction frame where the time dependent periodic Hamiltonian $H(t)$ is reduced to the time-independent diagonal average Hamiltonian $\bar{\epsilon}$. One enters this frame at time t_0, evolves under the time-independent Hamiltonian $\bar{\epsilon}$, and then goes back to the initial frame at time t. In other words, the time dependence of the Hamiltonian is transferred to the frame.

Interaction frame

We now show how to numerically compute $U(t_1, t_0)$ using the equations given above. For an efficient numerical computation of the propagator, we decompose it into three parts

Period borders

$$U(t_1, t_0) = U(t_1, T_1)U(T_1, T_0)U^\dagger(t_0, T_0) \ , \tag{2.104}$$

where T_1 and T_0 defined as $T_k = T\lfloor t_k/T \rfloor = p_k T$ are the period borders before t_1 and t_0, respectively. They are multiples of T. Now

$$U(t_k, T_k) = F(t_k)e^{-i\bar{\epsilon}(t_k - T_k)}F^\dagger(T_1) = F(\tau_k)e^{-i\bar{\epsilon}\tau_k}F^\dagger(0) = X(\tau_k) \ , \tag{2.105}$$

where $\tau_k = t_k - T_k$ is always smaller than T. The central propagator in Eq. (2.104) becomes

$$U(T_1, T_0) = F(p_1 T)e^{-i\bar{\varepsilon}(p_1 - p_0)T}F^\dagger(p_0 T) = F(0)e^{-i\bar{\varepsilon}pT}F^\dagger(0) = X^p(T) \quad (2.106)$$

with the number of periods $p = p_1 - p_0$. Altogether, we now have

$$U(t_1, t_0) = X(\tau_1)X^p(T)X^\dagger(\tau_0) . \quad (2.107)$$

This is illustrated in Figure 2.10(a).

Segmentation   Next, a set of $X(t)$ with $0 \le t \le T$ is computed by dividing one period T into small segments separated by $t_j = jT/n$ ($0 \le j \le n$). The segments are $\Delta t = T/n$ wide. Over each segment $1 \le j \le n$, the Hamiltonian $H(t)$ is assumed to be time-independent and is approximated by $H_j = H(t_j - \Delta t/2)$. The iteration equation for the propagator is then

$$X(t_j) = e^{-iH_j\Delta t}X(t_{j-1}) \quad (2.108)$$

with $X(0) = \mathbb{1}_N$ (see Figure 2.10(b)). In this way, one obtains all three propagators needed for computing $U(t_1, t_0)$.

If all the $X(t_j)$ are stored, they can be re-used in Eq. (2.107) when multiple propagators under the same Hamiltonian have to be computed.

2.7 Interpolative refinement

Smoothness   In all types of experiments discussed so far peak positions y, amplitudes I and line widths Γ are generally continuous smooth functions of all spin Hamiltonian parameters. This means that peak data for the spin Hamiltonian parameter values p_1 and p_2 can be used to interpolatively calculate peak data for $p_1 < p < p_2$. The associated computational cost is significantly smaller than that for a direct quantum mechanical computation. Interpolative refinement is therefore always advisable when distributed systems are simulated. In the following we present some interpolation methods and discuss their application in EPR spectral simulations.

2.7.1 Methods

Interpolants   Most commonly[1] pieces of linear or cubic polynomials (splines) are used as interpolants between data points (knots). An interpolant is said to be C^k-continuous if all derivatives up to the kth are continuous at the data points. Simple linear interpolation gives C^0 lines, since the slopes of the interpolating lines jump at the knots. Hermite cubic splines as used in Section 2.2.2 are C^1-continuous, that is, the first derivative is continuous at the data points, but the second not. Polynomial interpolants can be easily integrated and differentiated.

PSfrag replacements
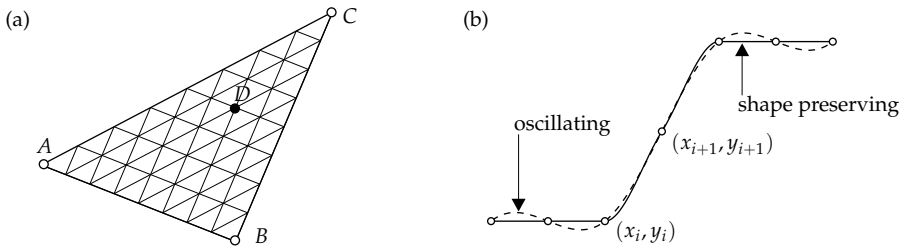
Figure 2.11: (a) Local linear interpolative refinement in a triangle of data *A*, *B*, and *C*. *D* is an interpolated point as given in Eq. (2.109). (b) Fritsch-Carlson shape-preserving spline interpolant (solid line) does not overshoot like a global spline (dashed).

There are two categories of interpolation procedures, global and local ones. With the former, the value at any given location depends on all the data values while the latter involves the use of only the nearest points. Global cubic splines are C^2-continuous, whereas local cubic (Hermite) splines are C^1. Linear interpolation is always a local method.

<div style="float:right">Global vs. local</div>

Interpolation methods depend also on whether correct derivatives are available as in Section 2.2.2 or have to be estimated. For peak data interpolation, derivatives are too expensive to calculate, so that either global interpolation with suitably chosen boundary conditions or a local method with an appropriate derivative estimate is used.

<div style="float:right">Derivatives</div>

For interpolation over a 2D parameter domain like the (ϕ, θ) space of spin system orientations, global or local cubic tensor-product splines can be used, if data are computed over a rectangular grid. If not, more general local methods can be applied. The simplest works on a triangle formed by three knots and interpolates linearly in between as illustrated in Figure 2.11(a), giving

<div style="float:right">2D</div>

$$y_D = \frac{k}{n}(y_B - y_A) + \frac{l}{n}(y_C - y_A) \qquad k = 1, \dots, n \quad l = 0, \dots, k \ . \qquad (2.109)$$

This method is very convenient for general interpolative refinement [Wan95].

A more sophisticated but still efficient local interpolation approach that generates very smooth surfaces for arbitrary knot distributions in 2D is the natural neighbour interpolation [Oka00]. It is widely used in computational geometry and geophysical sciences [Sam95], but too general for the interpolation problems occurring in EPR spectral simulations.

<div style="float:right">Natural neighbours</div>

There are situations where global or local cubic interpolation has to be applied with care. Standard interpolation methods do not respect the shape and monotonicity of the data and can create artifactual oscillations that are not consistent with the knot data. Fortunately, there exist a number of local cubic interpolation methods that conserve the monotonicity of the data. One of them, due to Fritsch

<div style="float:right">Preserving shape</div>

---

[1] Good overviews of interpolation are given in [Wat86, Kno99].

and Carlson [Fri80], is illustrated in Figure 2.11(b). For knots $x_{i-1} < x_i < x_{i+1}$ with data points y_{i-1}, y_i and y_{i+1} the slope estimate m_i at knot x_i for the interpolant between x_i and x_{i+1} is

$$m_i = \frac{1}{2} \left(\frac{y_i - y_{i-1}}{x_i - x_{i-1}} + \frac{y_{i+1} - y_i}{x_{i+1} - x_i} \right) \quad \text{if} \quad (y_{i+1} - y_i)(y_i - y_{i-1}) > 0$$
$$m_i = 0 \quad \text{otherwise.} \tag{2.110}$$

From this the cubic polynomial can be constructed

$$y(t) = \boldsymbol{t}^{\mathrm{T}} \boldsymbol{p}_i = (t^3 \ t^2 \ t \ 1)^{\mathrm{T}} \boldsymbol{M} \, (x_i \ x_{i+1} \ m_i \ m_{i+1})^{\mathrm{T}} \tag{2.111}$$

with $t = (x - x_i)/(x_{i+1} - x_i)$ and $\boldsymbol{M}$ as defined in Eq. (2.41) on p. 26. For more details see [Kno99, Kva00].

2.7.2 Use in EPR

In EPR simulations of distributed systems, the main use of interpolation is to refine peak data starting from computed values over a coarse grid of a spin Hamiltonian parameter distribution such as that of a principal value of the $\boldsymbol{g}$ matrix or a combination like E/D. Most prominent, though, is the orientational distribution in the angles ϕ, θ and χ.

Amplitudes
In contrast to peak positions, peak amplitudes usually depend on all three angles, so that a one-dimensional linear or cubic interpolation along χ followed by an analytical integration of the interpolant can be used to obtain a cumulative peak amplitude for a given orientation (ϕ, θ). In pulse EPR simulations such an interpolant integration reduces the computational effort considerably. In cw EPR and ENDOR, the χ integration is performed analytically (Eq. (2.53)).

The EPR and ENDOR amplitudes of Eq. (2.55) and Eq. (2.64) are real and straightforward to interpolate over ϕ and θ, whereas the real and the imaginary parts of the complex pulse EPR amplitude data have to be interpolated separately. Using magnitude and phase instead is not advisable, since the phase can change very abruptly with any spin Hamiltonian parameter, especially if the magnitude is small.

Amplitudes are not always very smooth. In systems with anisotropies much larger than the excitation bandwidth, only a small region of orientations takes part in the experiment, intensities are zero outside (see Section 4.5). This affects for example α_{vu} in Eq. (2.60). In such cases Fritsch-Carlson shape-preserving cubic splines have to be used.

Positions
Peak positions can be interpolated using tensor-product splines in the (ϕ, θ) domain. A rectangular grid[1] over these two angles allows easy interpolation, but even triangular grids can be handled efficiently by pre-interpolating them to a rectangular grid over ϕ and θ. The choice of the interpolation method strongly

---

[1] Orientational grids are discussed in detail in Chapter 4.

PSfrag replacements

linear
interpolation

local cubic
interpolation

global cubic
interpolation
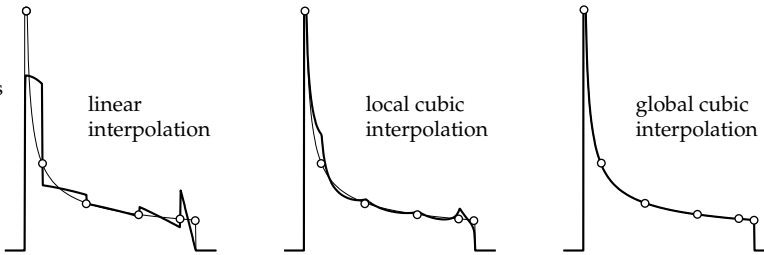
Figure 2.12: Quality of different interpolation schemes for an axial powder spectrum. Peak positions at a mere 6 orientations (indicated by circles) were quantum-mechanically computed and interpolated over a very fine grid.

Table 2.5: Methods used for interpolative refinement of peak data in various EPR experiments.

Experiment	Positions	Amplitudes	Level
cw EPR	global cubic	linear	B_{vu}, A_{vu}
ENDOR	global cubic	Fritsch-Carlson cubic	Δ_{vu}, A_{vu}
pulse EPR	linear	linear	$\epsilon^{(k)}, \Sigma, T^{(k)}, \Delta$

depends on the experiment being simulated. For direct spectral acquisition like in cw EPR and ENDOR, the interpolant must be C^2 (see illustration in Figure 2.12). Only in this case will the spectrum be continuous in its first derivative, as can be inferred from Eq. (1.24). A C^2 interpolant can only be obtained by global cubic interpolation. For time-domain acquired pulse EPR spectral peaks, a linear C^0 interpolation method is usually sufficient.

The interpolation can be carried out either on the eigenpairs of the diagonalised spin Hamiltonian prior to any peak computation or on the final peak positions and amplitudes. In cw EPR, the latter is preferable, since the computation of resonance fields and amplitudes is complicated. In ENDOR, the computation is simpler, but the interpolation on the peak list level is still faster. In pulse EPR, it is much more efficient to interpolate the matrices Σ, T, Δ and ϵ and not the final amplitudes and frequencies (see Eq. (2.79) and Eq. (2.81)). The choice of methods is summarised in Table 2.5.

Interpolation level

In pulse EPR, interpolation can be employed when signals have to be integrated over a range of values for certain delay times in the pulse sequence. Integrative boxcar detection can also be simulated by computing the echo intensity on a coarse grid within the detection window and subsequently integrating a linear interpolant.

More pulse EPR

Cubic interpolation was first applied to EPR spectral simulations by van Veen [vV78]. In [Gri90] bi-cubic interpolation was used. Mombourquette [Mom92] uses linear interpolation along a spiral of orientations (see Section 4.4). In 1995, Wang et al [Wan95] introduced a very fast orientational interpolation scheme

History
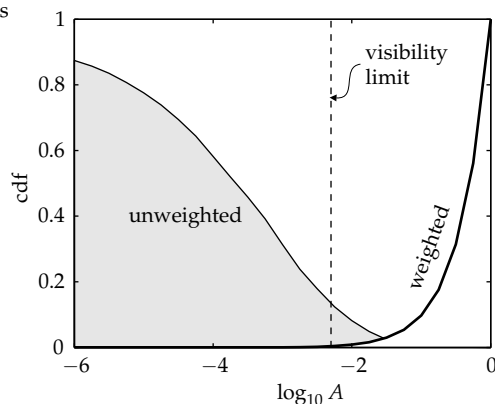
Figure 2.13: Normalised cumulative distribution (cdf) of peak amplitudes A for a HY-SCORE experiment on a typical $S = 1/2$, $I = 1$ system. The unweighted cdf indicates the fraction of peaks with amplitudes smaller than A. The weighted cdf is obtained by multiplying the unweighted cdf with the amplitudes.

combining 1D global cubic interpolation with 2D local linear interpolation within orientational triangles as in Figure 2.11(b). Cubic splines along the B_0 dimension, as used in Section 2.2.2, are known for some time [Mab92, Gaf98].

2.8 Peak number reduction

Peak list reduction

The peak list will contain peaks with amplitudes differing by orders of magnitude. Peaks that are too low in intensity compared to the strongest one can safely be neglected, since they will not have any visible influence on the final spectrum. Given a peak list, a relative rejection threshold η is defined and all peaks p with relative amplitudes $A_p/A_{\max}$ falling below this threshold are removed. η is usually in the range of 10^{-4} to 10^{-3}.

In a typical HYSCORE experiment for example, 90% of all peaks have intensities below the rejection threshold (see gray distribution in Figure 2.13). Their contribution to the final spectrum is negligible (white distribution in Figure 2.13). This approach shortens the peak list considerably and hence lightens the computational burden on the next step in the simulation, the construction of the spectrum (see next chapter).

More time savings

However, the time used for computing insignificant peaks has already been wasted, so the performance gain is only partial. It is preferable to avoid their computation in the first place. There are two ways to achieve this goal. One can either estimate peak intensities in advance and select a limited set of transitions (cw EPR, ENDOR) or adjust the absolute rejection level on the fly during the peak computation (pulse EPR). Both approaches not only save costs for spectrum construction, but also in the first spin dynamical part. In the following we will

consider these two methods in more detail.

2.8.1 Transition pre-selection

In cw EPR and ENDOR many transitions are irrelevant since either the spectro-
meter frequency is far off the transition frequency or the transition amplitude is
negligible. In the high-field limit, that is, when all internal interactions in the spin
system are much smaller than the Zeeman interaction, it is easy to select only the
significant allowed EPR and ENDOR transitions based on the quantum numbers
m_S and m_I of the associated states. Forbidden transitions can thus be excluded.
Even for single-crystal simulations this saves time.

$\quad$ In cases of strong mixing of the Zeeman states (e.g., the system of Figure 2.5 on
p. 27) m_S and m_I are not good quantum numbers anymore, and all the peaks have
to be computed. Savings are only possible if distributed systems are simulated
and more than a single spin Hamiltonian is given. In the case of powder spectra
where usually $N > 100$ Hamiltonians are evaluated, peak data at a couple of
orientations $n \leq 10$ are pre-computed. For each peak, the resulting amplitudes
are averaged and serve as an overall amplitude estimate. Peaks with an average
relative amplitude below η are excluded for the remaining $N - n$ orientations.
Care has to be exercised in the case of strong mixing, where amplitudes can be
strongly orientation dependent.

$\quad$ Many peaks can be excluded without evaluating their amplitudes. If a peak
position falls outside the field or frequency range of interest for all n orientations
chosen above, the peak can be neglected even if it has significant amplitude. In
a general pulse EPR simulation, this screening can throw out as much as 80% of
all peaks theoretically available from the pre-computed Σ, Δ and T.

(margin note: Quantum numbers)

(margin note: Estimates)

(margin note: Range filtering)

2.8.2 Adaptive thresholding

In pulse EPR, screening for significant amplitudes turns out to be more involved,
since amplitudes strongly depend on the orientation of the spin system, and ex-
perimental parameters such as interpulse delays can create narrow-ranged blind
spots where the amplitude drops to zero. A simple and rough estimate like for
cw EPR and ENDOR is not possible.

$\quad$ Threshold η is relative to the maximum peak intensity. In the case of a HY-
SCORE spectrum, this is

$$A_{\max} = \max_{i,j,k,l} T_{ij} \Sigma_{jk} T_{kl}^\dagger \Delta_{li} \ . \tag{2.112}$$

Since it is not possible to compute $A_{\max}$ without computing all the products, a
different road to thresholding has to be taken.

$\quad$ The procedure is as follows (see Figure 2.14). The first peak of the first spin
Hamiltonian is computed, no matter how strong it is. Its amplitude will be the
maximum *so far*, $\tilde{A}_{\max}$. If the amplitude of the next peak A is smaller than $\eta\,\tilde{A}_{\max}$,

(margin note: Adaptive method)
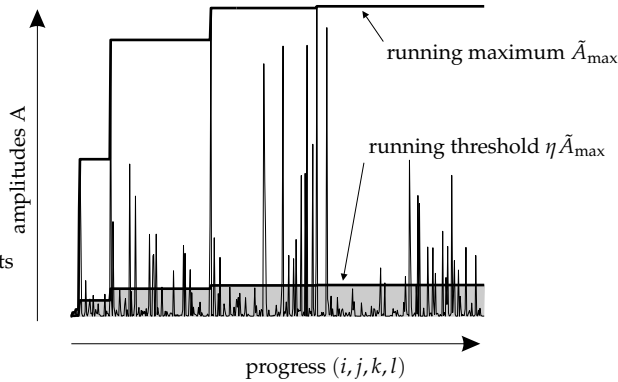
Figure 2.14: Adaptive thresholding. All peaks in the shaded area are ignored.

it is ignored, but if $A \geq \eta \tilde{A}_{\max}$, it is kept for spectrum construction. If, additionally, $A > \tilde{A}_{\max}$, then the current maximum $\tilde{A}_{\max}$ is adjusted. This continues until the last peak of the last spin Hamiltonian has been examined and possibly computed. In this adaptive procedure the maximum peak amplitude is computed on the fly, and the threshold is adjusted continuously. Only at the very beginning of the simulation amplitudes below the final absolute rejection threshold $\eta A_{\max}$ are computed.

Partial products The fact that pulse EPR amplitudes are products of matrix elements can be used to apply the above adaptive thresholding procedure already during the computation of the products. If Σ and Δ in Eq. (2.112) are normalised so that their maximum elements are 1, $A_{\max}$ will never be larger than 1. Consequently, if a product $T_{ij}\Sigma_{jk}$ is below the current threshold $\eta \tilde{A}_{\max}$, the total amplitude containing this product will be below $\eta \tilde{A}_{\max}$, independent of the matrix elements $T^{\dagger}_{kl}$ and Δ_{li}. Thus, the peak computation is aborted at the earliest moment possible, and the total recursive computation of all amplitudes containing the product $T_{ij}\Sigma_{jk}$ is avoided. In connection with range filtering, this method increases the speed of pulse EPR simulations tremendously. The combined approach is illustrated in Figure 2.15.

2.9 Performance issues

Workhorses The three numerical workhorses in any quantum-mechanical computation of peak data that does not rely on explicit formulas are matrix exponentiation, matrix diagonalisation and matrix-matrix multiplication. The objective of any algorithm is to keep the number of diagonalisations, exponentiations and multiplications at a minimum, and at the same time to perform these formidable tasks in a time as short as possible. Matrix multiplications are very elementary oper-
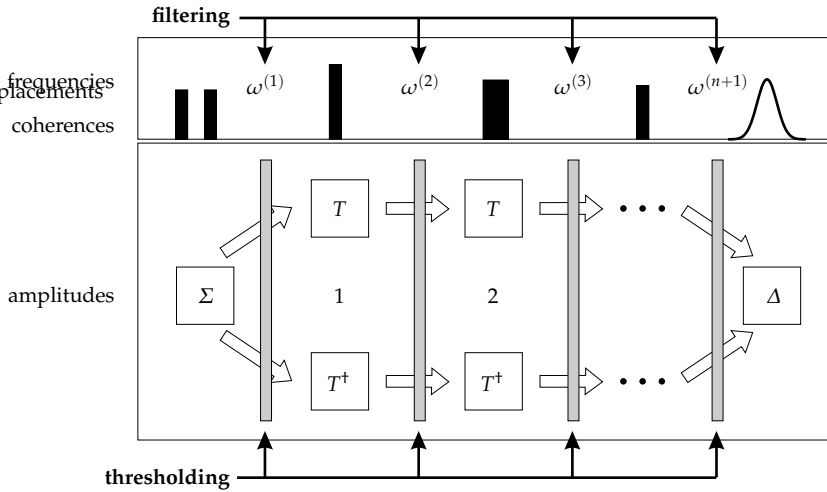
Figure 2.15: Filtering and adaptive thresholding in FD simulation of pulse EPR experiments.

ations. They are $O(N^3)$ and are nowadays available in optimised form for all computational platforms.

Algorithms for matrix diagonalisation are well established [Gol96] and work with an $O(N \log N)$ efficiency, where $N \times N$ is the size of the matrix. If only eigenvalues are needed, the diagonalisation is substantially faster. In EPR simulations all matrices are Hermitian, for which there are dedicated algorithms available in efficient implementations like the LAPACK library [And99]. Diagonalization

Exponentiation of a matrix A can be reduced to diagonalisation and a basis transform Exponentiation

$$\exp A = U \exp \Lambda\, U^\dagger \quad \text{with} \quad A = U \Lambda U^\dagger , \qquad (2.113)$$

where Λ is the diagonalised form of A and $\exp \Lambda$ a shorthand notation for taking the exponent the diagonal elements of Λ. U is the matrix of column eigenvectors of A and is always unitary if A is Hermitian. This eigenpair method is easiest to implement, but Padé approximations [Gol96] and Krylov subspace projection methods [Sid98] are used as well.

The larger a spin state space is in EPR, the sparser the Hamiltonian and other operator matrices are. There are special methods for handling sparse matrices, but they have not been applied in EPR spectral simulations so far except in the work of Freed [Sch89]. Sparse methods

Improvements in the algorithms for matrix diagonalisation and exponentiation will directly translate into improved performance of EPR simulation software. But such research is definitely beyond the realm of computational EPR.

3 Spectra

New in this chapter:

▷ Separate treatment of spectral construction and its classification in spectral and time domain acquisition
▷ Distinction between sampling and boxcar detection in simulations
▷ Simplified formulas for pseudomodulation (p. 61)
▷ Analytical projective formula for anisotropically broadened line shapes (p. 69)
▷ Concept of 2D projections
▷ A thorough analysis of construction methods for time-domain signals
▷ An excellent approximate method for time-domain signal construction from a list of peaks, based on convolution and deconvolution (Section 3.2.3)

In the last chapter we have explained how a list of peak positions and intensities can be efficiently computed from a set of given spin Hamiltonian parameters and the experimental settings. In this chapter we proceed to the second step of spectral simulations, that is, the construction of the experimental spectrum from its peak list representation.

The construction procedure depends on how the spectrum is acquired in the actual experiment. There are two types of acquisition, depending on which domain is swept. For both types, the sweep can be linear or stochastic.

Acquisition types

One type is the direct acquisition of the spectrum by sweeping the spectral domain variable. The most prominent example is cw EPR, where the static field is swept, but all field-swept pulse EPR experiments and most ENDOR experiments belong to this type as well.

The other type is the Fourier Transform type of acquisition. Spectra are acquired as a function of the abscissa variable in the inverse spectral domain. If the final spectrum is a function of frequencies, it is a time variable that is swept. All pulse EPR and some pulse ENDOR experiments belong to this category.

We dedicate one section to each type and present for both a variety of methods available for spectrum construction. Section 3.1 deals with the case of spectral domain acquisition, whereas Section 3.2 discusses time-domain experiments. Note that this distinction is based purely on computational considerations. In Section

3.3 we show an efficient method to quickly evaluate line shapes, a task central to both spectral and inverse domain conversions.

The choice of method also depends on whether anisotropic (homogeneous or inhomogeneous) broadenings in the form of strains are present. If not, a line shape can be simply added by convolution in the spectral domain after the stick spectrum has been constructed. This is the usual procedure in pulse EPR, where line width and line shape anisotropies are generally neglected. Broadenings are more or less isotropic, since they are determined by limited acquisition times, the excitation width of the pulses and broadening effects of the apodization window used. In cw EPR, anisotropies are much more common. They are mostly due to strains, making the line widths orientation dependent. Here we present methods for both isotropic and anisotropic broadenings.

3.1 Spectral domain acquisition

In this section, spectral construction methods for directly acquired spectra are discussed. When the spectral domain is swept directly, a given peak corresponds to a simple Kronecker delta peak in the theoretical spectrum with intensity I_p and position P_p

$$f(y) = I_p \delta(y - P_p) \, , \tag{3.1}$$

if we neglect for the moment the line width Γ_p and any effects of integrations, electronic filters and other manipulations on the signal pathway.

For computer acquisition, the continuous spectrum $f(y)$ is digitised along both abscissa and ordinate. Along the abscissa only a finite number of points y_i is sampled, usually separated by a constant distance $\Delta y = y_i - y_{i-1}$. Each measured analogue value $S(y_i) = S[i]$ is converted to a 8- to 20-bit integer number $S[i]$ using an analog-to-digital converter. This ordinate digitisation is always neglected in spectral simulations, where it is assumed that all experimental spectra are measured properly to avoid any ordinate quantisation effects. Spectral simulations commonly use floating point numbers to represent signals.

The values measured also depend on whether the spectral signal is integrated before digitisation or not, as illustrated in Figure 3.1. In both cw EPR and cw ENDOR signals are integrated between two sampling points y_{i-1} and y_i, so that the value sampled at y_i is proportional to

$$S[i] \propto A[i] = \int_{y_{i-1}}^{y_i} f(y) \, \mathrm{d}y \, . \tag{3.2}$$

Any spectral features between y_{i-1} and y_i are integrated and contained in $S[i]$, though only in a cumulative way.

In all other spectral-domain experiments (in pulse ENDOR and any 2D experiment with field or radio frequency along one dimension), the signal is sampled directly at the points y_i

$$S[i] \propto f(y_i) \tag{3.3}$$

PSfrag replacements
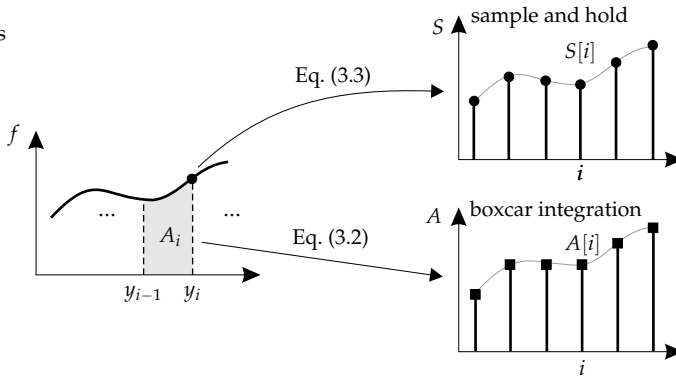
Figure 3.1: Two different detection modes for signals measured and sampled in the spectral domain.

Figure 3.2: Difference between the two detection methods for the same orthorhombic powder spectrum. The exact formulas from Section 3.1.1 were convoluted with a Gaussian with $\Gamma_{\text{FWHH}} = \Delta y$.
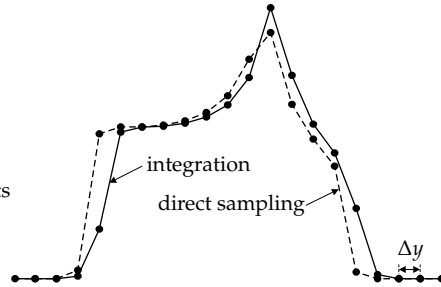
without integration, so that the final signal S does not contain any information on the behaviour of f between y_{i-1} and y_i.

Any careful spectrum construction algorithm must take this difference into account and use different methods for the two detection modes. A digitised integrated signal appears shifted and slightly distorted compared to the signal proper (see Figure 3.2). These distortions are only on the scale of one step increment on the abscissa, but they may harm accurate spectral fitting in the case of narrow, but anisotropic lines.

Not all spectrum construction methods presented in this chapter are able to produce both types of signals. The histogram method for example (3.1.2) performs a digitised integration (Eq. (3.2)) and cannot be adapted to accommodate direct sampling, unless the derivative of the spectral function can be computed. All projection methods (3.1.4) and line shape copying (3.3) can handle both types.

There are a number of additional effects in experimental spectra acquired in the spectral domain that can be modelled separately after the spectrum construction itself.

In swept experiments the finite sweep speed can give rise to disturbing arti- Transient facts. In cw EPR, sweeping the external magnetic field too quickly distorts the effects
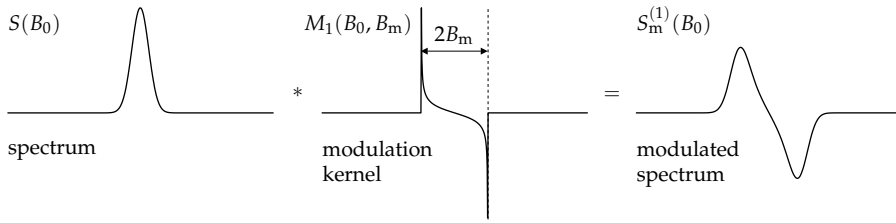
Figure 3.3: First harmonic pseudo-modulation by convolution of the absorption spectrum with a modulation kernel. $2B_m$ is the peak-to-peak modulation amplitude.

spectrum. The theory developed in Chapter 2 is valid only in the limit of infinitely slow scans. In ENDOR, the radio frequency sweep heats the sample and saturates nuclear transitions and thereby changes its spectral response, often resulting in a heavily distorted baseline. Measuring the values $S[i]$ with a random acquisition order of i rather than a linear incrementation strongly reduces these effects. Since transient sweep phenomena do not contain information about static spin Hamiltonian parameters, computer simulations do not include them, and it is up to the experimentalist to acquire distortion-free spectra.

RC filter   Electronic manipulations on the signal pathway can usually be modelled by applying digital filters to the digitised signal. E.g. the common electronic resistor-capacitor (RC) filter with the time constant $T_c = RC$ (resistance R and capacitance C) in cw EPR spectrometers is equivalent to the application of a single-pole recursive filter to the signal $S[n]$, giving

$$T[n] = \sum_{k=0}^{n} a_k S[n-k] + \sum_{k=1}^{n} b_k T[n-k] \tag{3.4}$$

with the only non-zero coefficients

$$a_0 = 1 - e^{-t_{\text{sampl}}/T_c} \quad \text{and} \quad b_1 = e^{-t_{\text{sampl}}/T_c} , \tag{3.5}$$

where t_{sampl} is the sampling time. Bandwidth filters in pulse EPR are also easy to apply to the spectrum in a separate step.

Field modulation   In cw EPR experiments, the static magnetic field along z_L is usually modulated

$$B(t) = B_0 + B_m \sin(2\pi\nu_m t) \tag{3.6}$$

with frequency ν_m and amplitude B_m, and the signal is detected at the first or second harmonic of ν_m, yielding spectra resembling the first or second derivative of the absorption spectrum $S(B_0)$ for small B_m. In simulations, this modulation effect can be added in a separate step after the computation of the absorption spectrum. The so-called pseudo-modulation [Hyd90] consists of a convolution of the absorption spectrum with an appropriate modulation kernel function (see Figure 3.3)

$$S_m^{(n)}(B_0) = S(B_0) * M_n(B_0, B_m) \tag{3.7}$$

to give the modulated spectrum $S_{\mathrm{m}}^{(n)}$, where n indicates the detection harmonic.

M_n is the Fourier transform of a Bessel function of the first kind and order n, which can be expressed[1] in terms of a Chebyshev polynomial T_n of the first kind and order n

<div style="text-align:right">Modulation kernel</div>

$$M_n(B_0, B_{\mathrm{m}}) = \mathrm{i}^n \int_{-\infty}^{\infty} J_n(\beta B_{\mathrm{m}})\, \mathrm{e}^{\mathrm{i}\beta B_0}\, \mathrm{d}\beta = (-1)^n \frac{2 T_n(B_0/B_{\mathrm{m}})}{\sqrt{B_{\mathrm{m}}^2 - B_0^2}}\ . \tag{3.8}$$

For the first two harmonics, the kernels are explicitly

$$M_1(B_0, B_{\mathrm{m}}) = -\frac{2(B_0/B_{\mathrm{m}})}{\sqrt{B_{\mathrm{m}}^2 - B_0^2}} \qquad M_2(B_0, B_{\mathrm{m}}) = \frac{4(B_0/B_{\mathrm{m}})^2 - 2}{\sqrt{B_{\mathrm{m}}^2 - B_0^2}}\ . \tag{3.9}$$

The pseudo-modulation approach is valid as long as ν_{m} is much smaller than the line width in the spectrum. Otherwise the true multi-photon nature [Käl03] of the field-modulated cw EPR experiment unveils and leads to the appearance of sidebands which are not modelled by Eq. (3.7).

3.1.1 Exact solutions

As a reference against which numerical spectrum construction methods can be tested for accuracy, exact powder spectra have to be computed, at least for some basic situations. Analytical expressions are obtained by solving Eq. (1.24) for given y and A. For most spin systems this is impossible, but when A is assumed to be independent of Ω and set to 1, the spectrum of a two-level ($S = 1/2$) system can be computed.

For the field-swept spectrum of such a system with orthorhombic $\boldsymbol{g}$ matrix full analytical expressions have been derived by Kneubühl[2] [Kne60]. If the three principal g values are ordered $g_1 > g_2 > g_3$ and all three are different, we have (see Figure 3.4)

<div style="text-align:right">Field sweep</div>

$$B_1 \leq B \leq B_2 : \quad S(B) = \frac{2}{\pi} \frac{B_1 B_2 B_3 B^{-2}}{\sqrt{(B_1^2 - B_2^2)(B^2 - B_3^2)}} K(k) \tag{3.10}$$

$$B_2 \leq B \leq B_3 : \quad S(B) = \frac{2}{\pi} \frac{B_1 B_2 B_3 B^{-2}}{\sqrt{(B_1^2 - B^2)(B_2^2 - B_3^2)}} K(1/k) \tag{3.11}$$

with the principal resonance fields $B_i = h\nu_{\mathrm{mw}}/(\mu_{\mathrm{B}} g_i)$, the parameter

$$k = \sqrt{\frac{(B_1^2 - B^2)(B_2^2 - B_3^2)}{(B_1^2 - B_2^2)(B^2 - B_3^2)}} \tag{3.12}$$

---

[1] To the best of our knowledge, this is the first time these explicit expressions are reported.
[2] Beltrán-López has recently revived them [Bel96, Bel99].
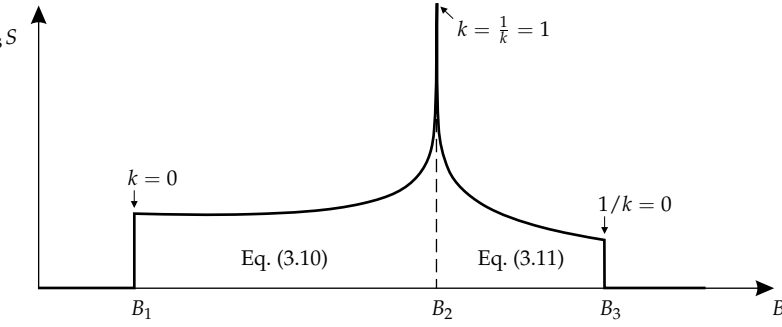
Figure 3.4: Exact powder line shape for an $S = 1/2$ system with rhombic g matrix. $B_i = h\nu_{\text{mw}}/(\mu_{\text{B}}g_i)$.

and the complete elliptic integral of the first kind

$$K(k) = \int_0^{\pi/2} \frac{\mathrm{d}\theta}{\sqrt{1 - k^2 \sin^2 \theta}} \qquad K(0) = \frac{\pi}{2} \qquad K(1) = \infty \ . \tag{3.13}$$

The resulting spectrum has a pole at B_2, but it is normalised

$$\int_{B_1}^{B_3} S(B)\mathrm{d}B = 1 \ . \tag{3.14}$$

Formulas for the axial cases $g_1 = g_2 > g_3$ and $g_1 > g_2 = g_3$ are only special cases of Eq. (3.10) and Eq. (3.11) with $K(0) = \pi/2$.

Frequency sweep   The expressions for a frequency-swept spectrum are similar. With the principal resonance frequencies $\nu_i = \mu_{\text{B}}B_0 g_i/h$ and a constant magnetic field B_0 they are

$$\nu_1 \leq \nu \leq \nu_2 : \quad S(\nu) = \frac{2}{\pi} \frac{\nu}{\sqrt{(\nu_1^2 - \nu_2^2)(\nu^2 - \nu_3^2)}} K(k) \tag{3.15}$$

$$\nu_2 \leq \nu \leq \nu_3 : \quad S(\nu) = \frac{2}{\pi} \frac{\nu}{\sqrt{(\nu_1^2 - \nu^2)(\nu_2^2 - \nu_3^2)}} K(1/k) \tag{3.16}$$

with

$$k = \sqrt{\frac{(\nu_1^2 - \nu^2)(\nu_2^2 - \nu_3^2)}{(\nu_1^2 - \nu_2^2)(\nu^2 - \nu_3^2)}} \ . \tag{3.17}$$

These expressions can be analytically convoluted with a smoothing line shape [Bel99], but since it is much easier to numerically convolute the spectrum after construction, the analytical approach is not of much use.

Starting from the above analytical formulas, both sorts of detection discussed above are possible. The formulas are directly applicable for sample-and-hold

detection, whereas for integrative detection the integrals of the above formulas have to be used. Closed-form expressions could not be found, but they are easy to evaluate in a series expansion.

To our best knowledge, no explicit expressions are known for any but this simple two-level system, so that numerical approximations are mandatory. Next we will discuss the latter in detail, keeping the exact equations as a reference. In one case, a sum of exactly computed axial powder line shapes has been used to approximatively construct orthorhombic spectra [Var96].

To assess the accuracy of an approximated spectrum $\tilde{S}$ constructed with a numerical method, we compare it to the correct reference spectrum S using the total deviation error

Spectral error

$$\epsilon = \sqrt{\sum_i \left(\tilde{S}[i] - S[i]\right)^2} \ . \tag{3.18}$$

The spectra must be normalised in the sense

$$\sum_i S[i] = \sum_i \tilde{S}[i] = 1 \ . \tag{3.19}$$

3.1.2 Histograms

Any numerical spectrum construction method starts from a list of peaks. The simplest way to compute the spectrum associated with this list is to take each peak in turn and plug its amplitude into the corresponding bin of the spectral domain vector, thereby constructing a weighted histogram of the peak positions.

The peak's amplitude A_p is added to the bin next to the peak's position y_p in the direction of the sweep of the spectral axis. For the 1D case and upward sweep this means

Binning

$$\tilde{S}[k] \leftarrow \tilde{S}[k] + w_p A_p \qquad k = \lceil y_p / \Delta y \rceil \tag{3.20}$$

($\lceil a \rceil$ indicates the smallest integer larger than or equal to a). w_p is the weight associated with peak p (see next chapter). $\tilde{S}[k]$ collects the amplitudes of all peaks with positions $y_{k-1} < y_p \leq y_k$. Thus it corresponds to an integrative acquisition. In the limit of an infinite number of peaks with proper weights the total approaches Eq. (3.2). Sampled acquisition cannot be modelled by this method.

For each peak the histogram method is exact and very quick. The big disadvantage is the large number of peaks needed to obtain a smooth powder pattern. If the number is too small, artifacts—so-called computational or simulation noise—distort the spectrum. For a given number of peaks N, the level of computational noise depends on the spread of the spectrum Δ_S, on the resolution of the spectral axis Δy and on the width Γ_{FWHH} of the line shape convoluted with the spectrum.

Noise

The error is determined by the number of peaks per bin in the spectrum, that is, by the peak density

Peak density

$$\rho = N\Delta y / \Delta_S \ . \tag{3.21}$$

PSfrag replacements

$\epsilon = 10^{-1}$
$\rho = 0.1591$

$\epsilon = 10^{-2}$
$\rho = 16.37$

$\epsilon = 10^{-3}$
$\rho = 1394$
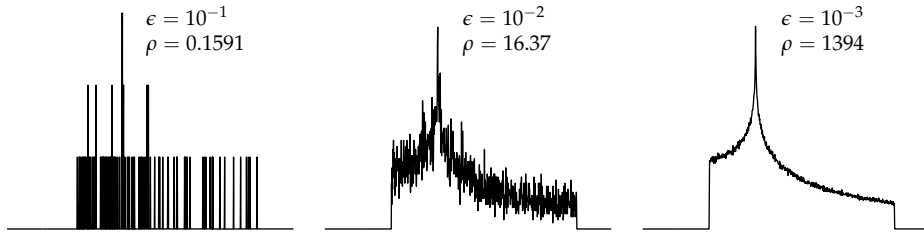
Figure 3.5: Errors ϵ of histogram approximations with different peak density ρ.

PSfrag replacements

1

3/10

1/10

3/100

1/100
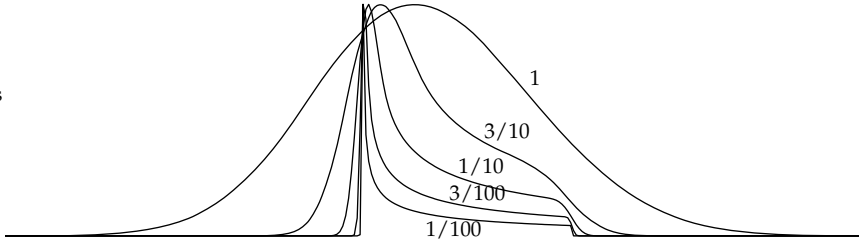
Figure 3.6: Broadening of an axial powder spectrum by convolution with a Gaussian line shape with different relative convolution widths λ (see Eq. (3.22)).

To avoid excessive noise, a value much larger than 1 is usually required. A few levels of error and the associated peak densities are illustrated in Figure 3.5. It is clear that $\epsilon \leq 10^{-3}$ is necessary to make the error visually acceptable.

Smoothing   The noise can be substantially reduced by convoluting the spectrum with a line shape of sufficiently large width, resulting in a broadened rather than a stick spectrum. If we look at the convolution line width Γ_{FWHH} relative to the spectral spread Δ_{S}

$$\lambda = \Gamma_{\mathrm{FWHH}}/\Delta_{\mathrm{S}} \, , \tag{3.22}$$

we see (Figure 3.6) that any spectrum with $\lambda < 1/100$ can be considered a stick spectrum, whereas for $\lambda \geq 1$ the anisotropic structure of the spectrum is completely lost and not discernible any more from the pure convolution line shape.

Figure 3.7 plots the error ϵ as a function of λ and ρ. An increase of an order of magnitude in ρ reduces the error by a factor of 10, whereas an increase of an order of magnitude in λ reduces it by approximately 5.

Although the histogram method is attractive due to its simplicity for both 1D and 2D spectra, it performs very badly compared to all other construction methods, which we will discuss in the next subsections.

3.1.3 Gradient-broadened accumulation

Since a peak list of finite length contains spectra for only a finite number of orientations, each computed orientation represents a set of neighbouring orientations,
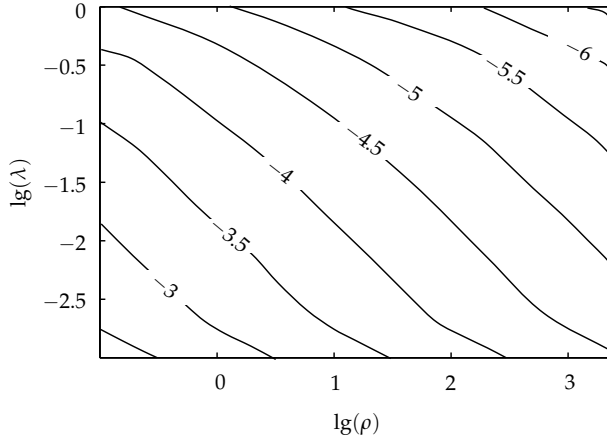
Figure 3.7: Dependence of the simulation error $\lg(\epsilon)$ for an orthorhombic spectrum on peak density ρ (Eq. (3.21) and relative line width λ (Eq. (3.22)) in the histogram method. Random orientations were used.

which vary slightly in their resonance positions and amplitudes. The actual spectrum represented by the peaks of a single computed orientation is thus not a stick spectrum, but a small broadened part of the powder spectrum. This effect can be approximated by estimating an orientational strain for each peak and by incorporating it in the manner of Section 2.3 into the convolution line width. The line due to a peak of a given orientation is thus broadened by an amount that bridges the empty spectral region between itself and its computed neighbour. In this way, a rather smooth powder spectrum with small spectral error can be constructed with a small number of orientations (around 20 for axial, 60 for orthorhombic and 200 for low-symmetry spectra). This method, termed the mosaic misorientation linewidth model, was introduced by Noble in the SOPHE software [Nob02b].

The orientational strain for all peaks at orientation $\boldsymbol{\Omega}$ is proportional to the magnitude of the orientational gradient of the peak positions y_p at this orientation

Position gradient

$$\sigma(\boldsymbol{\Omega}) \propto |\nabla y_p(\boldsymbol{\Omega})| \,. \tag{3.23}$$

For a frequency-swept spectrum this is (see Eq. (2.28))

$$|\nabla \nu_p| = \sqrt{(\langle v|G_{xL}|v\rangle - \langle u|G_{xL}|u\rangle)^2 + (\langle v|G_{yL}|v\rangle - \langle u|G_{yL}|u\rangle)^2} \,, \tag{3.24}$$

whereas for field-swept spectra the $1/g$ factor from Eq. (2.52) has to be included, yielding

$$|\nabla B_p| = \frac{\sqrt{(\langle v|G_{xL}|v\rangle - \langle u|G_{xL}|u\rangle)^2 + (\langle v|G_{yL}|v\rangle - \langle u|G_{yL}|u\rangle)^2}}{\langle v|G_{zL}|v\rangle - \langle u|G_{zL}|u\rangle} \,. \tag{3.25}$$

65
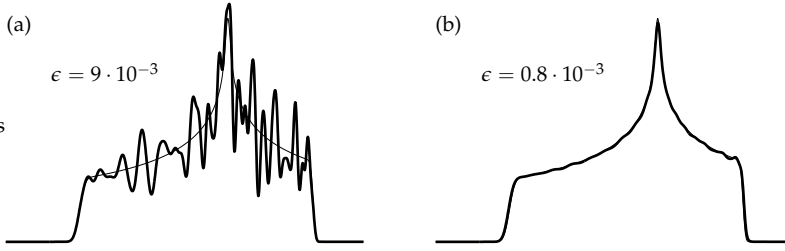
Figure 3.8: Spectrum accumulation using orientational strain broadened lines. (a) only
with g strain (b) including orientational strain. 105 computed peaks, peak density
$\rho = 0.16$.

Smoothing
line width

The effective line width used is

$$\Gamma_{\text{FWHH}} = \alpha d_p |\nabla y_p| \,, \tag{3.26}$$

where d_p is the angular distance to the orientation next to p and α is an additional smoothing factor usually set to 1. Larger values of α result in smoother but coarser spectra. For an axial spectrum with N evenly spaced orientations between $\theta = 0$ and $\theta = \pi/2$, the angular distance is $d\pi/2/(N-1)$, independent of p. For an orthorhombic spectrum and a sufficiently even distribution of N orientations over 1 octant, $d \approx 0.844/(\sqrt{N} - 2N^{0.2})$ is a p-independent average.

The gradient is zero for principal axis directions, so that sharp artifacts at the turning points of the spectrum can appear. They can be either excluded or avoided by not choosing orientations along such singular directions. If there are any additional line broadenings in the spectrum (g or A strain), the line widths at the principal axis directions are not zero, and the problem is not present.

Both sampled and integrative detection are possible, depending on whether an absorption line shape or the numerical derivative of its integral is used in constructing the spectrum.

The method is illustrated in Figure 3.8 with a finite g strain present. The fewer orientations are included in the spectrum, the broader it will be. Sharp spectra will require more orientations than broad ones. Stick spectra cannot be computed with this method.

The method requires the gradients to be computed, implying a longer computation time for a single orientation as compared to the histogram method. But this is offset by the enormous reduction in the peak density ρ needed to reach a certain level of ϵ.

The disadvantages of the orientational strain method can be circumvented and it can be outperformed with the projective method introduced in the next subsection.

3.1.4 Projections 1D

Peak positions (i.e. the resonance surfaces) and amplitudes change smoothly over orientations and can be interpolated. In Section 2.7 this property has been exploited to cheaply compute new peaks. But instead of constructing interpolative polynomials and evaluating them for many points to obtain more peaks, one can project each interpolating polynomial *analytically* onto the spectral domain. The resulting subspectra add up to the total stick powder spectrum. This projective approach was already introduced to magnetic resonance [Ebe83] and applied [Ald86] some time ago, but has since passed more or less [Pon99b] unnoticed. Originally it was limited to stick spectra. Here we present its principles and extend its scope to anisotropic line widths.

First we discuss the general non-axial case. Consider a triangular patch Q (see Figure 3.9(a)) of the resonance surface $y(\boldsymbol{\Omega})$ with positions and associated amplitudes $A(\boldsymbol{\Omega})$ computed on the three vertex orientations $\boldsymbol{\Omega}_1$, $\boldsymbol{\Omega}_2$ and $\boldsymbol{\Omega}_3$. Using Eq. (1.24), the spectrum of this patch is

Non-axial spectra

$$S(y) = \oint_{Q, y=y(\boldsymbol{\Omega})} \frac{A(\boldsymbol{\Omega})}{|\nabla y(\boldsymbol{\Omega})|} \mathrm{d}\boldsymbol{s} \ . \tag{3.27}$$

If the triangle is sufficiently small, two approximations can be made. First, the amplitude can be assumed to be constant over the triangle, equal to $A = (A_1 + A_2 + A_3)/3$. Second, the magnitude of the gradient $|\nabla y(\boldsymbol{\Omega})|$ can be set constant, that is, the resonance position depends linearly on the orientation within this triangle. This leaves a simple line integral

$$S(y) = \frac{A}{|\nabla y|} \oint_{y=y(\boldsymbol{\Omega})} \mathrm{d}\boldsymbol{s} \ . \tag{3.28}$$

If the resonances at the three edges are ordered $y_1 \leq y_2 \leq y_3$, we get

$$y_1 \leq y \leq y_2: \quad S(y) = aA \frac{y - y_1}{(y_2 - y_1)(y_3 - y_1)} \tag{3.29}$$

$$y_2 \leq y \leq y_3: \quad S(y) = aA \frac{y - y_2}{(y_3 - y_2)(y_3 - y_1)} \tag{3.30}$$

with the area a of the spherical triangle (see Eq. (4.9) on p. 94). These equations describe a triangular subspectrum as illustrated in Figure 3.9(a). Its shape is independent of the size and shape of the spherical triangle Q projected and depends only on the peak positions at the triangle vertices. By dividing the entire orientational sphere into such spherical triangles and adding up the resulting subspectra, an approximation of the powder stick spectrum is obtained (see Figure 3.10(a)). Its integral is 4π, if all amplitudes are 1.

In the case of an axially symmetric resonance function, the projection is also very simple. The resonance surface can be subdivided in spherical zones $\theta_i \leq \theta \leq$

Axial case
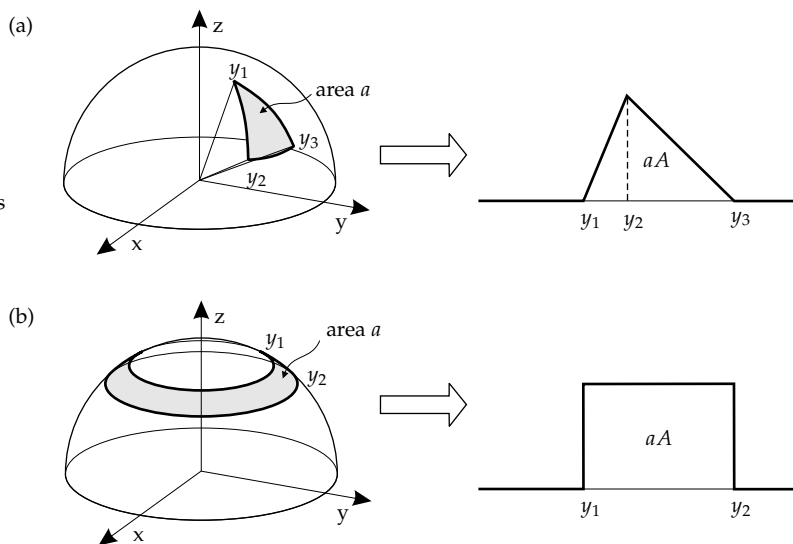
Figure 3.9: (a) The analytical spectral projection of a small triangular orientational region of a resonance surface gives a triangular spectrum. (b) The same projection for an axial spherical zone gives a rectangular spectrum.
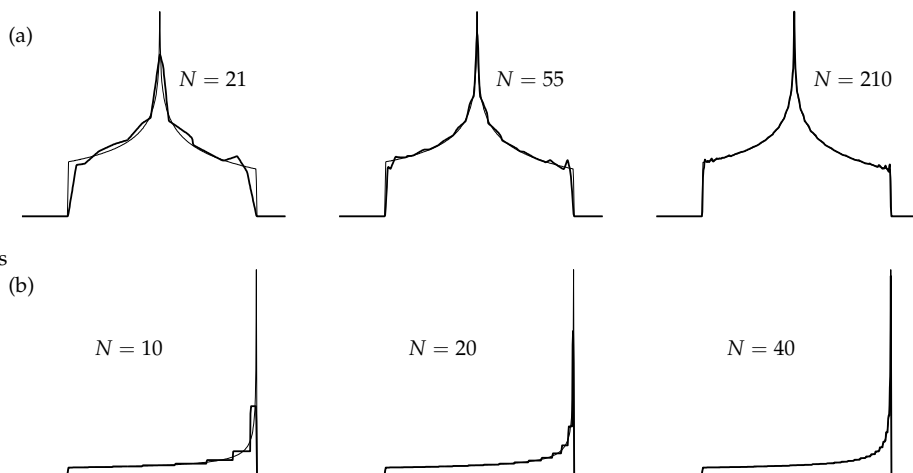
Figure 3.10: Stick spectra approximated by the projection method. (a) non-axial case, (b) axial case. N is the number of explicitly computed orientations.

θ_{i+1} with computed spectra at θ_i and θ_{i+1} (see Figure 3.9(b)). Each of these zones is projected separately. If the resonance and the intensity function are smooth enough over the interval $\theta_1 \leq \theta \leq \theta_2$, we can again assume the resonance gradient to be constant

$$|\nabla y(\mathbf{\Omega})| = \frac{y_2 - y_1}{\sin(\theta_1 - \theta_2)} \quad (3.31)$$

and approximate the amplitude by the mean $A = (A_1 + A_2)/2$. With a constant gradient, a certain value of resonance will occur only once within a zone, so that we finally obtain from Eq. (3.27)

$$y_1 \leq y \leq y_2 : \quad 2\pi A \frac{\cos\theta_1 - \cos\theta_2}{y_2 - y_1} \quad . \quad (3.32)$$

Hence, each interval projected into the spectral domain gives a rectangular spectrum.

The projected axial spectrum (Figure 3.10(b)) contains steps between the different projected zones. According to Eq. (3.28), they could be made continuous with quadratic splines and C^1 continuous with cubic splines, but their analytical projection in the style of Eq. (3.29) and Eq. (3.32) is not possible. A stepwise interpolation is possible, as was shown in Figure 2.12 on p. 51.

Eq. (3.29) and Eq. (3.32) describe the spectral function itself. For sample-and-hold detection they are evaluated directly. For boxcar detection, their integrals are used according to Eq. (3.2). These are straightforward to obtain.

Anisotropic line widths

Up to now, the projection method has only been designed for computing stick spectra. But in the case of anisotropic line widths, it is still possible to use an analytical projection approach, since convolutions of the basic projected spectral building blocks in Eq. (3.29) and Eq. (3.32) are readily obtained.

In the axial case the rectangular subspectrum becomes the sum of two line shape integrals (see Appendix A). If the shape is Gaussian with line width Γ, the resulting function is *Axial case*

$$S(y) = \frac{1}{2(y_2 - y_1)} \left[\mathrm{erf}\left(\sqrt{2}\frac{y - y_1}{\Gamma}\right) + \mathrm{erf}\left(\sqrt{2}\frac{y_2 - y}{\Gamma}\right) \right] \quad . \quad (3.33)$$

For the non-axial case, the convolution of the triangular subspectrum is more complicated. With the convolution function *Non-axial case*

$$F(x) = \frac{1}{\sqrt{2\pi}} e^{-2\left(\frac{x}{\Gamma}\right)^2} + \frac{x}{\Gamma}\left[1 + \mathrm{erf}\left(\sqrt{2}\frac{x}{\Gamma}\right)\right] \quad (3.34)$$

the resulting elementary spectrum is

$$S(y) = \frac{\Gamma}{y_3 - y_1} \left[\frac{F(y - y_1) - F(y - y_2)}{y_2 - y_1} + \frac{F(y_3 - y) - F(y_2 - y)}{y_3 - y_2} - \frac{2}{\Gamma} \right]. \quad (3.35)$$
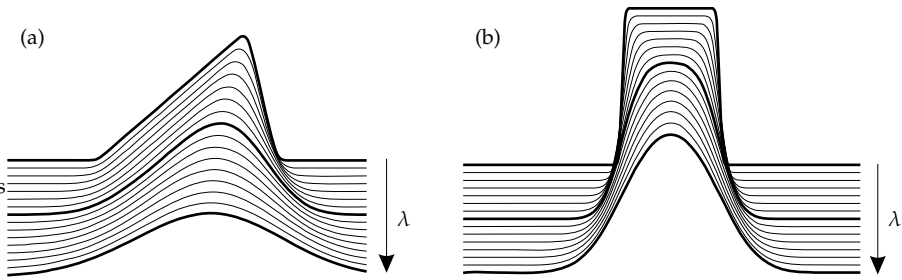
Figure 3.11: Convolution of projected elementary spectra with Gaussians of varying width. (a) non-axial case (b) axial case. Spectra with relative line width $\lambda = 0.05$, 0.4 and 0.7 are highlighted.
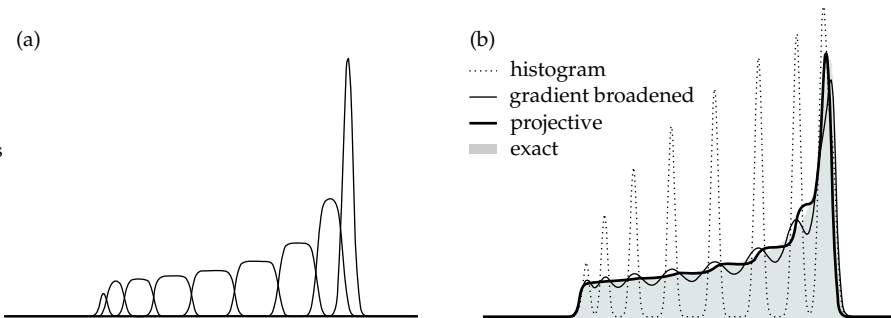
Figure 3.12: (a) Convoluted elementary spectra in the projective method for anisotropic line widths. (b) Comparison of different construction methods for an axial spectrum with anisotropic line width. 10 explicit orientations are used.

Anisotropic line broadening is commonly modelled by Gaussians, so we have not derived the equations for Lorentzian broadening. The above expressions are only valid for sample-and-hold detection, for boxcar detection they have to be integrated.

Comparison
Using the algorithm from Section 3.3.2, these equations can be evaluated quite quickly. The convoluted elementary spectra for both axial and non-axial cases are illustrated in Figure 3.11 for different relative line width. Figure 3.12 illustrates the application of the analytical projection to the construction of an axial spectrum and compares all methods. In terms of spectral error ϵ, both gradient broadening and projection work similarly well. But the projective method produces less pronounced wiggles, which become more disturbing if first-derivative spectra are computed.

The difference between the gradient weighted line shape binning and the projections approach now becomes clear. With gradient broadening, each triangular or rectangular subspectrum or segment is approximated by a Gaussian with a line width to cover the spread of the subspectrum. For $\lambda \gg 1$ the two methods

(a) (b)

PSfrag replacements

ν_2 ν_2

ν_1 ν_1
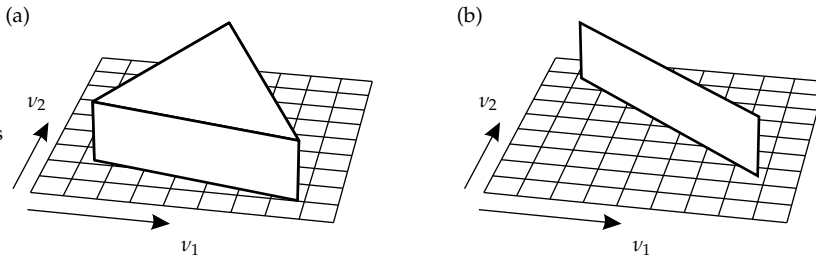
Figure 3.13: Projection of simplices for 2D spectra. (a) non-axial symmetry (b) axial symmetry.

(a) (b)

PSfrag replacements
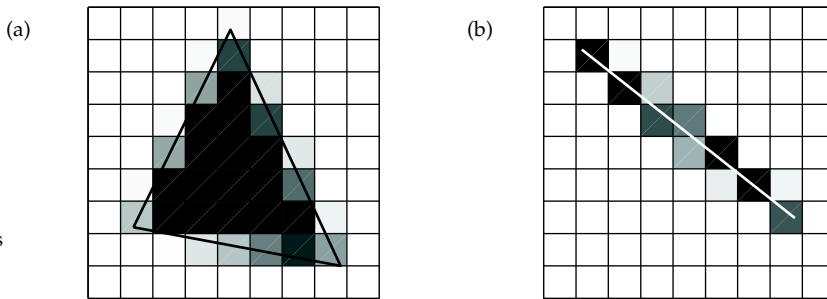
Figure 3.14: Discretisation for 2D spectra, (a) non-axial and (b) axial symmetry. The projections are the same as in Figure 3.13. The spectral amplitude in the square bins is color-coded.

converge.

A very different but basically also projective method has been proposed by Ponti [Pon99b]. The spectrum between the abscissa points y_i and y_{i+1} is equal to the area of the part of resonance surface falling between the two contour lines $y = y_i$ and $y = y_{i+1}$. This requires the computation of contour lines for all y_i in the spectral domain abscissa vector. Extension to spectra with transition intensity anisotropy is possible, but computationally unfeasible. The contouring method is without any practical relevance.

Contouring

3.1.5 Projections 2D

The projective method of the previous subsection can be generalised to two dimensions. It is, however, substantially more complex than for 1D spectra and can only be done for stick spectra. We only outline the basic concepts.

It can be shown that the spectrum of a set of orientations contained in a spherical triangle produces a cake-slice-like pattern (see Figure 3.13). It has linear edges if the resonance function is assumed to be linear in both sweep variables. And it has constant height, if the peak amplitude is approximated by its average

over the three vertices. In the axial case, a wall-like ridge is obtained.

Discretisation of these patterns into a finite-length 2D matrix is not straightforward (see Figure 3.14). Algorithmic concepts can be borrowed from computer graphics (Bresenham line drawing algorithm, sweep line rasterisation of polygons, anti-aliasing for fonts). 2D experiments with direct spectral acquisition of both domains are, however, quite rare (e.g. the recently introduced 2D TRIPLE [Epe00]), so we have neither implemented nor studied these 2D projections in greater detail.

3.2 Time domain acquisition

All pulse EPR data are acquired by varying a time interval in the pulse sequence of the experiment. A peak in these experiments corresponds to a harmonic (sin or exponential) evolving along this time variable

$$s_p(t) = A_p \, \mathrm{e}^{\mathrm{i}2\pi\nu_p t} \, \mathrm{e}^{-\lambda_p t} \; . \tag{3.36}$$

For the moment, we neglect the anisotropy of the relaxational broadening λ_p and assume that the last factor in the above expression can be added to the final spectrum by a simple convolution. The N-point Discrete Fourier Transform (DFT) of s_p will not be a delta peak, unless its frequency falls exactly on a DFT frequency. Therefore, the spectral domain methods of the previous section are not applicable. In the following we discuss various methods for constructing such time-domain signals.

TD vs. FD signals   TD and FD signals of a single peak with amplitude 1 differ greatly in their character. The TD signal is distributed over the entire domain, and its magnitude is always 1. It seems not to be possible to devise any method that allows reconstruction of the TD signal with less computational cost than the direct evaluation of the exponential according to Eq. (3.43). On the other hand, most of the FD signal is concentrated around the frequency ν of the exponential. This compactness of the FD signal makes it possible to save computation time by constructing only the important central part around ν and neglecting the small wings. Such approximate methods sacrifice accuracy for the sake of computational efficiency. There is only one FD approximation method used in the literature. It is identical to the histogram method of Section 3.1.2.

Error measures   To assess the quality of an approximation, we define error measures for both TD and FD[1]. An appropriate error function in TD is

$$\mu_{\mathrm{TD}}(\nu) = \max_{0 \leq n \leq N-1} |s_{\mathrm{approx}}^{(\nu)}[n] - s^{(\nu)}[n]| \; , \tag{3.37}$$

which describes the maximum of the magnitude difference between the approximate and the exact TD signal of a single exponential with amplitude 1 and fre-

---

[1] These error measures are different from Eq. (3.18).

quency ν. For FD the corresponding error measure is given by

$$\mu_{\text{FD}}(\nu) = \max_{0 \le m \le N-1} |S_{\text{approx}}^{(\nu)}[m] - S^{(\nu)}[m]| . \tag{3.38}$$

The average of μ over all possible frequencies ν is a frequency-independent overall error measure. It turns out that for all cases studied μ in the above formulas is periodic in ν with period $\Delta\nu = (N\Delta t)^{-1}$, so that the average can be limited to one period

Averages

$$\epsilon_{\text{TD}} = N\Delta t \int_0^{1/(N\Delta t)} \mu_{\text{TD}}(\nu)\text{d}\nu . \tag{3.39}$$

In FD, the corresponding error function

$$\epsilon_{\text{FD}} = N\Delta t \int_0^{1/(N\Delta t)} \mu_{\text{FD}}(\nu)\text{d}\nu \tag{3.40}$$

can be used. In practical computations, the integrals in the error functions have to be approximated by sums. In this work we integrate over 801 test frequencies uniformly distributed between two neighbouring DFT frequencies. The error function varies slightly with N. It is minimal in the region $100 < N < 300$, at $N = 1024$ it is about 10% larger. We use a 128-point signal as standard.

The errors are visually noticeable if they are above 0.005. We thus can tolerate errors below a significance limit of $\epsilon_0 = 0.005$.

3.2.1 Brute force

The overall TD signal is a linear combination of exponentials, and since the Fourier transform is linear as well, it is sufficient to consider only a single exponential with frequency ν and amplitude 1. Here we restrict ourselves to the 1D situation, where ν is a scalar. Extension to 2D is straightforward, but would unnecessarily complicate the notation.

The TD exponential with the frequency ν is given by

TD formula

$$s(t) = e^{\text{i}2\pi\nu t} . \tag{3.41}$$

In an experiment, this signal is sampled at N points in time $n\Delta t$ with $0 \le n \le N-1$ and the dwell time Δt, giving

$$s[n] = s(n\Delta t) = e^{\text{i}2\pi\nu n\Delta t} . \tag{3.42}$$

The TD signal can be constructed by explicitly evaluating this formula for all n. However, it is faster to compute $s[n]$ by $N-1$ consecutive multiplications

$$s[n] = s[n-1]\,e^{\text{i}2\pi\nu\Delta t} \qquad 1 \le n \le N-1 \tag{3.43}$$

with $s[0] = 1$.

The FT of the TD signal in Eq. (3.42) defined by

$$S(f) = \frac{1}{N} \sum_{n=0}^{N-1} s[n] e^{-i2\pi f n \Delta t} \tag{3.44}$$

is a periodic sinc function with a complex phase factor [Opp01]

$$S(f) = \frac{1}{N} e^{-i\pi(f-\nu)\Delta t(N-1)} \frac{\sin\left[\pi(f-\nu)N\Delta t\right]}{\sin\left[\pi(f-\nu)\Delta t\right]} \ . \tag{3.45}$$

It can be looked upon as a back-folded aperiodic sinc function. When this function is sampled at the frequencies $m\Delta f$ with the increment $\Delta f = (N\Delta t)^{-1}$ and $0 \le m \le N-1$, the DFT of the original signal

$$S[m] = S(m\Delta f) = \frac{1}{N} e^{-i\pi(m-\kappa)\frac{N-1}{N}} \frac{\sin\left[\pi(m-\kappa)\right]}{\sin\left[\pi(m-\kappa)/N\right]} \tag{3.46}$$

is obtained, with the scaled frequency $\kappa = \nu/\Delta f$. Though feasible, evaluation of this expression for the impulse response is impractical due to its complexity compared to TD.

The direct method (computation of the exponential in TD) needs one exponential computation and $N-1$ multiplications/peak. In the 2D case of an $N \times N$ signal, $(N-1)^2$ multiplications/peak are needed. The performance of Eq. (3.46) is even worse. The drawback of both methods lies in their slowness when many peaks have to be accumulated to construct a spectrum.

3.2.2 Histograms

One could tentatively apply the same procedure as for directly acquired spectra (Section 3.1.2). This speeds up the computation compared to the brute force method, but introduces quite some error.

This histogram method is to the best of our knowledge the only FD approximation method reported. This straightforward approach, which has not been studied in detail so far, takes a peak and rounds its frequency ν to the nearest DFT frequency, i.e. to the nearest multiple of Δf

$$k\Delta f = \lfloor \kappa + 1/2 \rfloor \Delta f = \lfloor \nu/\Delta f + 1/2 \rfloor \Delta f \ . \tag{3.47}$$

The peak is shifted by the frequency offset $\beta = \kappa - k$, which introduces a maximum rounding error of $\Delta f/2$. Then the value of the peak amplitude is added to bin k in the N-point FD vector. The periodic sinc is thus approximated by a slightly shifted periodic sinc, so that the discretisation of the latter gives a non-zero value only in one bin of the FD vector. Finally, an IDFT generates the approximate TD signal.
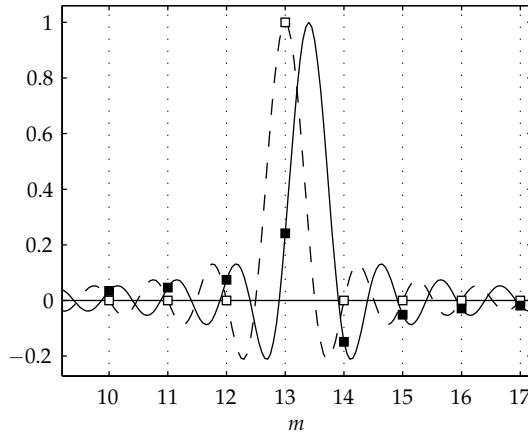
Figure 3.15: The histogram method. Solid: exact periodic sinc with $\nu = 13.4\Delta f$, dashed: shifted periodic sinc with $\nu = 13\Delta f$. ■: correct discretisation $S[m]$, □: $S_{\text{approx}}[m]$ in the histogram approximation. Only the real part is shown.

The big advantage of this method lies in the fact that for each peak only one rounding and one addition are needed. The speed-up compared to the direct evolution in TD is enormous. However, the small frequency error introduced by the rounding can cause significant errors in both TD and FD.

In FD, the distortion is obvious, as illustrated in Figure 3.15. The amplitude at   Distortions
the centre is far from being correct, and the wings on both sides are completely missing. In the figure the maximum magnitude error μ_{FD} is 1.04. In TD the phase error increases with increasing n (Figure 3.16). If the rounding error is $\Delta f/2$, the TD error μ_{TD} is 2.

In the case of multiple peaks, interference effects can make the errors very dis-   Interference
turbing. For example, two exponentials with opposite amplitudes 1 and -1 and frequencies $(k - 1/2)\Delta f$ and $(k + 1/2)\Delta f$ are shifted by the histogram method to $k\Delta f$ and $(k + 1)\Delta f$ respectively, and generate a purely real spectrum, whereas the correct spectrum should only have a non-zero imaginary part. In another un-favourable case, two peaks with amplitudes 1 and -1 and frequencies $(k - \alpha)\Delta f$ and $(k + \alpha)\Delta f$ with $0 \leq \alpha \leq 1/2$ are both rounded to $k\Delta f$ and accumulated into the same bin. As a consequence, they cancel completely, although they should give a single broadened peak around $k\Delta f$. This error is maximum at $\alpha = 0.372$ with $\mu_{\text{FD}} = 1.44$.

To remedy for these errors, the histogram method can be applied using an   FD expansion
extended FD vector of length eN ($e > 1$), where the DFT frequency spacing is $\Delta f/e$. Increasing the resolution of the frequency axis by a factor of e reduces the maximum rounding error to $\Delta f/(2e)$. The IDFT gives a TD signal of length eN, where the first N points are an approximation of the exact TD signal.
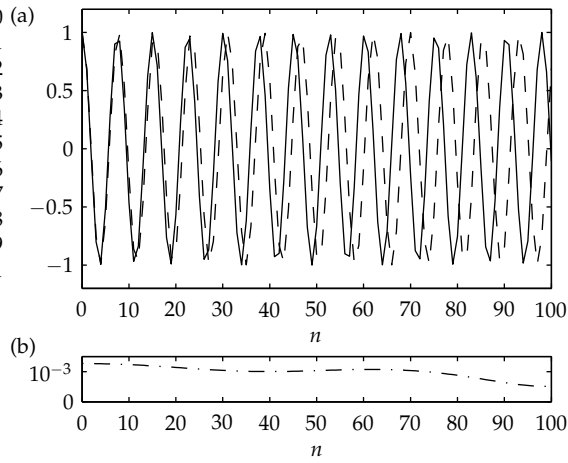
Figure 3.16: (a) Real part of the exact TD signal (solid) for $\kappa = 13.4$ and of the histogram approximation (dashed, $k = 13$). $N = 101$ points. (b) Magnitude difference between the exact TD signal and the convolution approximation.
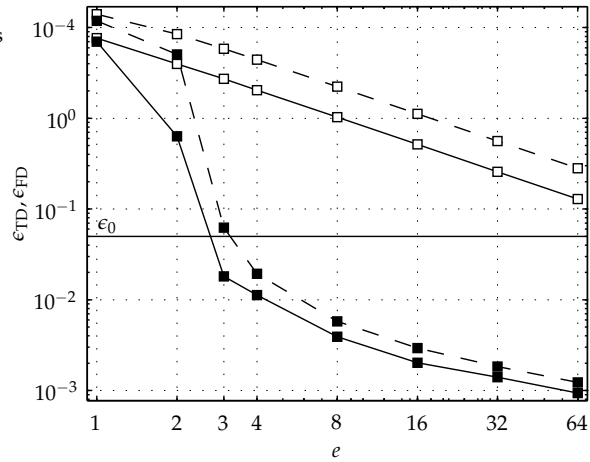
Figure 3.17: ϵ_{FD} (solid) and ϵ_{TD} (dashed) for histogram ($\square$) and the convolution method ($\blacksquare$, $M = 2$, α and γ optimised separately for each e) as a function of the expansion factor e.

Figure 3.17 shows the dependence of the average TD and FD errors on the expansion factor e. With increasing e the error decreases, but it is obvious that $e \geq 8$ is needed to reduce at least the mean FD error to an acceptable level. This is at the expense of a larger data array and a correspondingly slower IDFT, which might become prohibitive in 2D. A 256×256 TD signal would require the IDFT of at least a 2048×2048 FD array.

3.2.3 Convolution approximation

The approximation method we introduce here is based on convolution and de-convolution of the stick spectrum with a truncated and windowed sinc function (see the schematic illustration in Figure 3.18).

Truncating the full kernel function Eq. (3.46) to a region $2M\Delta f$ wide around its centre f speeds up the computation, but introduces truncation errors. With decreasing M, the computation gets faster, but the truncation errors increase. In the optimal case, M has to be chosen small enough to improve speed and large enough for the error to fall below a certain level of significance. The kernel function itself can also be varied to minimise the error. | Principles

The truncated kernel is best designed by apodising a sinc function with a window function. This is a standard technique for filter design in digital signal processing [Opp01]. The sinc function | Kernel design

$$\text{sinc}(\gamma x) = \frac{\sin(\pi \gamma x)}{\pi \gamma x} \qquad -1 \leq x \leq 1 \tag{3.48}$$

contains a width parameter γ. For apodization we use the Kaiser window,

$$K(\alpha, x) = \frac{I_0\left(\alpha\sqrt{1 - x^2}\right)}{I_0(\alpha)} \qquad -1 \leq x \leq 1 \tag{3.49}$$

with the zeroth-order modified Bessel function of the first kind I_0 and the width parameter α. K gives the best results among all classical windows. The resulting truncated kernel

$$R(y) = \text{sinc}\left(\gamma \frac{y}{M}\right) K\left(\alpha, \frac{y}{M}\right) \qquad -M \leq y \leq M \tag{3.50}$$

is zero outside the interval $[-M; M]$ and depends on α and γ and on the half-width M. In contrast to Eq. (3.45), this function is purely real, and its evaluation is therefore twice as efficient as that of a complex truncated periodic sinc.

For each peak the truncated kernel $R(y)$ is then sampled into the eN-point spectral vector $\tilde{S}$, centred at the position of the peak (see Figure 3.18) | Convolution

$$\tilde{S}[k_p + m] \leftarrow \tilde{S}[k_p + m] + R(m - \beta_p) \qquad \begin{cases} \beta_p \neq 0 & -M+1 \leq m \leq M \\ \beta_p = 0 & -M \leq m \leq M \end{cases} . \tag{3.51}$$
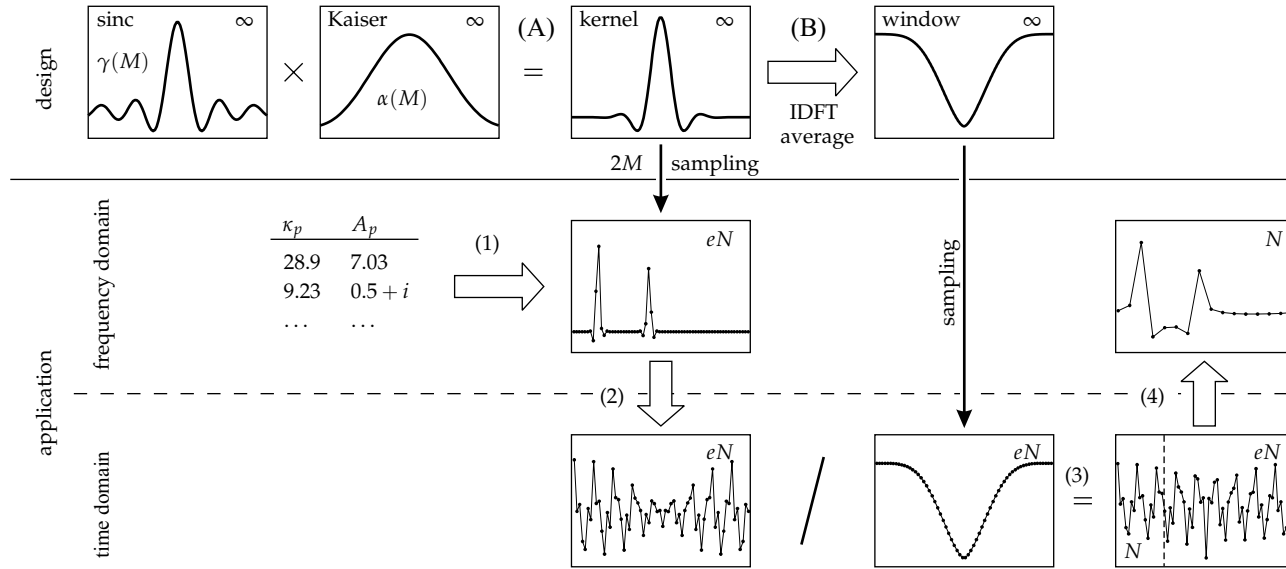
Figure 3.18: Design and application of the convolution method. Design steps: (A) kernel as a product of sinc function and Kaiser window, (B) correction window as average IDFT. Application steps: (1) continuous convolution of peak list and kernel, eN-point discretisation, (2) IDFT, (3) division by discretised correction window in TD (equivalent to circular convolution in FD), (4) DFT of the first N points.

0.6
0.7
0.8
0.9
1
−0.2

(a)

1.2

1.2

1.2
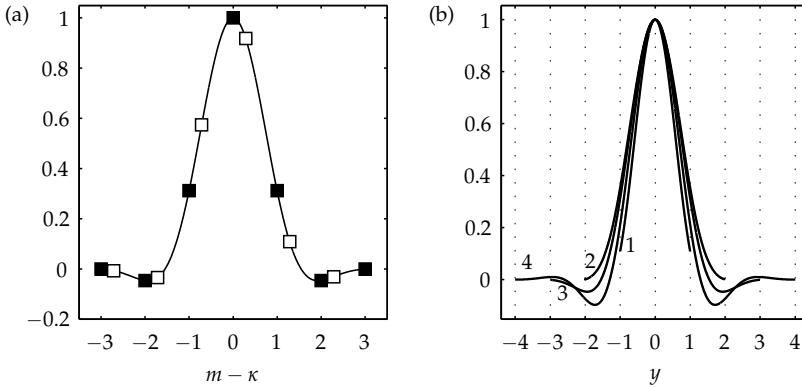
Figure 3.19: (a) Sampling a $2M + 1$ wide truncated kernel ($M = 3$). ■: $2M + 1$ values for frequency offset 0, □: $2M$ values for frequency offset $\neq 0$. (b) sinc/Kaiser kernels for different half-widths M.

In the case $\beta_p \neq 0$, i.e. when the peak frequency lies between two DFT frequencies, $2M$ points have to be evaluated per peak. If the peak frequency exactly coincides with a DFT frequency ($\beta_p = 0$), $2M + 1$ points have to be evaluated (see Figure 3.19(a)). If the peak lies on the edges of $\tilde{S}$, the sampled kernel has to be folded around. Similar to the histogram method, an expansion factor e (default value $e = 4$) is used. Its influence on the performance is analysed later. Mathematically, Eq. (3.51) corresponds to a continuous circular convolution of the stick spectrum T consisting of delta peaks at the given frequencies with the truncated kernel $R(y)$

$$\tilde{S} = T \circledast R . \tag{3.52}$$

The result $\tilde{S}$ is a pseudo-spectrum with peaks at the correct positions, but with distorted line shapes.

The distortion can almost completely be removed by deconvoluting the obtained pseudo-spectrum with the truncated kernel

Deconvolution

$$S = \tilde{S} \circledast^{-1} R . \tag{3.53}$$

This circular deconvolution can be performed in TD by dividing the IDFT of the pseudo-spectrum by a correction window W obtained by IDFT of the sampled kernel $R(y - \beta_p)$

$$W_\beta[n] = \sum_{m=-eN/2+1}^{eN/2} R(m - \beta) e^{i2\pi nm/eN} . \tag{3.54}$$

The correction window, however, is different for each peak and depends on its frequency offset β, since each β corresponds to a different set of $2M$ (or $2M + 1$)

M	γ_opt	α_opt	ϵ_TD	ϵ_FD
1	1.6695	4.7255	0.05456	0.03368
2	1.4889	10.9444	0.00185	0.00111
3	2.5878	11.3687	0.00094	0.00036
4	3.8593	12.7798	0.00066	0.00018
5	5.2596	13.4354	0.00030	0.00012

Table 3.1: Optimal parameters α and γ and the errors ϵ_TD and ϵ_FD for the convolution method depending on kernel half-width M.

values from the continuous kernel R, which in turn give different window functions in TD. If there is more than one peak in the pseudo-spectrum, the correction window cannot be optimal for all of them. But the mean error ϵ_TD can be minimised by using an average of the correction window W_β over all β

$$\overline{W}[n] = \int\limits_0^1 W_\beta[n]\,\mathrm{d}\beta \;. \tag{3.55}$$

If the continuous kernel is symmetric around its centre, this average window $\overline{W}$ is a real function.

The first N points of the TD signal obtained after application of $\overline{W}$ are an excellent approximation of the correct TD signal (see Figure 3.18).

Optimal parameters

The entire procedure above depends on M, α and γ. M is the parameter which determines the computational cost. For a given M, α and γ determine the quality of the approximation. α and γ are simultaneously optimised by a least-squares minimisation of the average maximum time-domain deviation ϵ_TD (Eq. (3.39)). The resulting filter kernels for $M = 1$ to 4 are shown in Figure 3.19(b). Table 3.1 lists optimal α and γ values for different values of M. Both α and γ strongly depend on M. The minima in the error function are very flat in the region $\alpha_\mathrm{opt} \pm 1/2$. On the other hand, the error function is more sensitive to γ.

Numerically, quasi-continuous representations with approx. $5000M$ points of the kernel R and the average window $\overline{W}$ can be pre-computed and re-used (see Figure 3.18, design steps). Instead of evaluating R in Eq. (3.51) anew for each peak, the values can be taken from its pre-computed representation (see Section 3.3.2). Peak frequencies are rounded to the next discrete frequency in this representation and are shifted by $\Delta f / 10^4$ at the most. The error introduced by this small shift does not contribute significantly to the overall error of the convolution method. To use the quasi-continuous correction window representation for the deconvolution of an eN-point signal, it has to be interpolated to eN points to obtain $\overline{W}[n]$.

PSfrag replacements
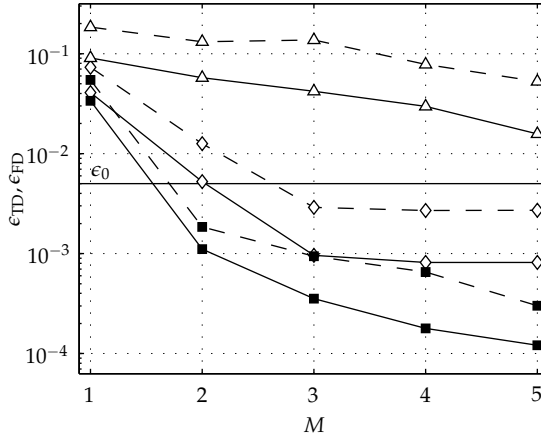
Figure 3.20: ϵ_{TD} (dashed) and ϵ_{FD} (solid) for different kernels ($e = 4$) as a function of the kernel half-width M. $\blacksquare$ sinc/Kaiser, $\lozenge$ Gaussian, $\triangle$ Lorentzian.

3.2.4 Performance and error analysis

Figure 3.20 shows the errors ϵ_{TD} and ϵ_{FD} of the convolution method based on the optimised sinc/Kaiser kernel. As expected, both errors decrease with increasing M. ϵ_{TD} is 2–3 times larger than ϵ_{FD}. By increasing M from 1 to 3, the error compared to the histogram method drops by almost two orders of magnitude in both TD and FD domain. The kernel with $M = 2$ gives already satisfactory results and is the one of our choice.

TD and FD errors

Figure 3.17 on p. 76 shows the error of the convolution method with the standard $M = 2$ sinc/Kaiser kernel as a function of the expansion factor e. For $e = 1$, the new method is not much better than the histogram approach, but it gains rapidly when increasing e to 4, where both TD and FD error levels are no longer significant.

Figure 3.21 shows the dependence of the errors μ_{TD} and μ_{FD} of the sinc/Kaiser kernel on the offset β of the peak from a DFT frequency. The TD error is periodic with period β/e and is most sensitive to the offset around $n\beta/e$. This means that the averaged window used is not the best choice for peaks close to DFT frequencies, but it is still the best choice to minimise the overall mean error. The FD error exhibits a more complex behaviour.

The error of the convolution method is different in character from the one of the histogram approach, which is a pure frequency error caused by the frequency shift (Figure 3.16(a)). In the convolution method only the amplitude is incorrect and becomes more accurate with increasing time (see the residuals in Figure 3.16(b)). Phase and frequency are exact within numerical accuracy.

Amplitude error

The origin of the error is not obvious. The fact that an average window is used

Error origin
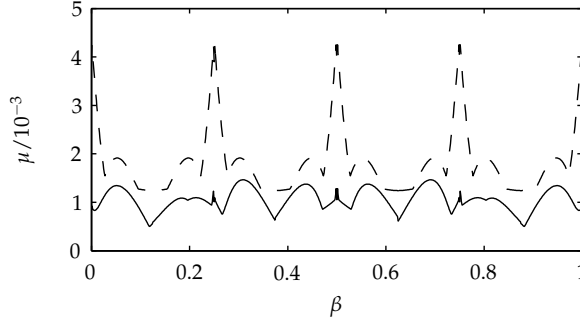
Figure 3.21: μ_{FD} (solid) and μ_{TD} (dashed) as a function of the frequency offset β for the sinc/Kaiser kernel with $M = 2$, $e = 4$.

explains only part of it. For a single peak there would still be an error, if the matching correction window were used. In the aperiodic case, a finite FD signal like the sinc/Kaiser kernel always has an infinite inverse FT. Hence the correct deconvolution window would have infinitely wide wings that asymptotically approach zero in both directions on the time axis. But since the window is only represented in a finite TD, the tails fold back, and the window is aliased. The shorter the kernel in FD, the wider is its associated window in the TD, and the stronger is the effect of back-folding. Thus it is the deconvolution of the pseudo-spectrum with an aliased version of the correct window that accounts for most of the error. The impact of this aliasing is already inherently minimised by the least-squares fit of α and γ to the TD error ϵ_{TD}.

The aliasing of the correction window also explains why the convolution method works well only for $e \geq 3$ (Figure 3.17). For $e < 3$, significant parts of the window lie outside the finite TD region and are folded back.

Physical kernels   Often physical line shape functions (either Lorentzians or Gaussians) with line widths γ are sampled into the FD, truncating the line shape function at some distance $k\gamma$ from its centre. Although this choice is obvious, it is not the best. We have examined these functions, using the kernels

$$R(y) = \left[1 + \frac{4}{3}\left(\frac{\gamma y}{M}\right)^2\right]^{-1} \qquad \text{and} \qquad (3.56)$$

$$R(y) = \exp\left[-2\left(\frac{\gamma y}{M}\right)^2\right] \qquad\qquad (3.57)$$

with $-M \leq y \leq M$ and optimising γ for each M exactly as in the sinc/Kaiser kernel design. It turned out that even with this γ optimisation Gaussians and especially Lorentzians perform significantly worse than the sinc/Kaiser design, as can be seen from Figure 3.20.

Relaxational anisotropy   If different oscillating components in an experimental signal decay at different

82
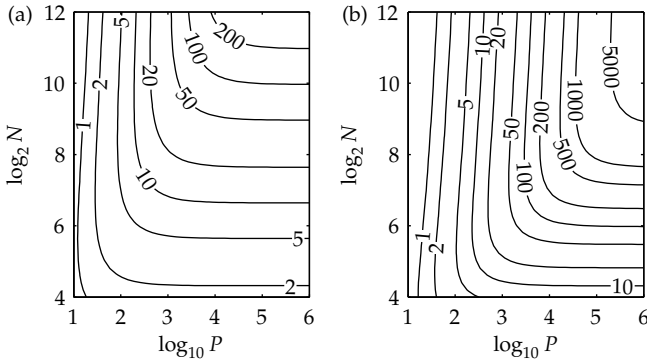
Figure 3.22: Speed-up of the convolution method ($M = 2$, $e = 4$) compared to the direct TD evolution. P: number of peaks, N: number of points along one dimension in TD (2D: total $N \times N$ points). (a) 1D, (b) 2D.

Method	1D	2D
TD evolution	$O(PN)$	$O(PN^2)$
FD histogram	$O(P)$	$O(P)$
FD convolution	$O(PM)$	$O(PM^2)$

Table 3.2: Asymptotic computational costs of TD construction in terms of arithmetic operations for various methods. P: number of peaks, N: number of points along one dimension in TD (2D: total $N \times N$ points).

rates, each peak in the spectrum will have a different line width. In this case, the explicit evaluation of a line shape function for each peak is mandatory, and neither the histogram nor the convolution approximation are applicable.

However, line shapes in pulse EPR spectra of disordered systems are not determined by these relaxational broadenings, but rather by unresolved couplings resulting in an additional almost isotropic inhomogeneous broadening. In all practical cases it is therefore sufficient to convolute the spectrum with a Lorentzian or Gaussian line shape after the powder spectrum has been constructed from the peak list.

The convolution method is much faster than the direct TD evolution according to Eq. (3.43). The asymptotic computational costs for all three methods are listed in Table 3.2. All costs scale linearly with P, but only the TD evolution depends directly on N. The dependence of the convolution method's performance on M and M^2 has little impact, since M is small. However, in the two FD methods, the additional cost for the IDFT [Pre92] may be significant. — Performance

Figure 3.22 illustrates the overall relative performance of the convolution method based on an analysis of the number of floating-point operations involved. For 1D experiments the convolution method is always faster than the TD evol- — Example
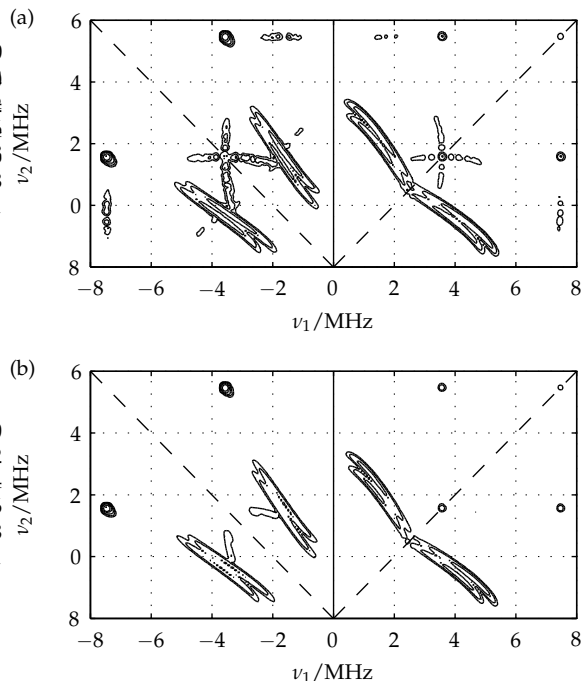
Figure 3.23: Simulated ^{14}N HYSCORE spectra, (a) histogram method, (b) convolution method. There is no visible difference between (b) and a spectrum accumulated with the exact TD evolution method. Spin system and experimental parameters as in Table 3.3. Logarithmic contour levels between 0.01 and 1 relative to the maximum intensity.

ution, and it performs exceedingly well in 2D experiments. The smallest gains are found in situations with $P < 10^2$, where the cost of the additional IDFT is significant, and in the case of $N < 2^5$, where the small value of N does not penalise the TD evolution too much. However, both situations are quite unusual. For pulse EPR simulations, $N \approx 2^8$ and $P \approx 10^5$ are common. In this case, 1D peak accumulations are 20 times and 2D accumulations are 1000 times faster. The error is below the significance level ϵ_0 and 200 times smaller than the error in the histogram method.

Example   As an illustrative example we apply the new method to the simulation of a typical HYSCORE spectrum (see Figure 3.23). HYSCORE is a basic 2D ESEEM experiment [Sch01] and the primary method for determining weak interactions between electron spins and nuclei such as hydrogens and remote nitrogens. The powder spectrum is computed as the sum of single crystal spectra from 4186 orientations. The computation of the resulting list of 489 544 peaks takes 13.27 s on a standard PC as summarised in Table 3.3. For the accumulation the convolu-

	computation time [s]		
Method	peak list generation	spectrum construction	total
TD evolution	13.27	2570.0	2583.3
histogram	13.27	0.74	14.01
convolution	13.27	3.05	16.32

Table 3.3: Computation times for a typical 2D HYSCORE spectrum for different spectrum construction methods. Spin system: $S = 1/2$, $g = 2$, one ^{14}N nucleus ($I = 1$, $g_n = 0.4038$), $A = 5$ MHz, $e^2qQ/h = 2.4$ MHz, $\eta = 0.5$. Experimental parameters: $\tau = 136$ ns, pulse lengths $10/10/20/10$ ns, $B_0 = 350$ mT, $\nu = 9.797369$ GHz. 256×256 points, $\Delta t = 50$ ns in both dimensions. 4186 orientations. Computed on a standard Linux PC (866 MHz Pentium III, 128 MB RAM).

tion method is only 4 times slower than the histogram method, but 840 times faster than direct TD evolution. In fact, with the latter approach the spectrum accumulation consumes 99.5 percent of the total computation time. As can be seen in Figure 3.23, all the artifacts from the histogram method are absent in the spectrum computed with the convolution method.

Combined with the frequency-domain formulas for pulse EPR of the previous Chapter, the convolution method greatly enhanced the speed of such simulations. When interpolation and thresholding are used additionally, the speed-up compared to a straightforward TD approach with simple, but expensive TD evolution can be beyond three orders of magnitudes for electron spin system with more than one coupled nucleus.

3.3 Spectral broadening

All methods presented above are valid only if all peaks have the same line width. In this case the corresponding line shape, usually a Gaussian or a Lorentzian (see Appendix A), is added by convolution to the final spectrum. This is discussed in Section 3.3.1. If peaks have different line widths, each of them has to be added to the spectrum separately. The methods from the previous sections are not well suited for such situations. We show a fast method of accumulating such spectral peaks with different line widths in Section 3.3.2. The performance of this step is absolutely crucial for the overall performance of simulation, especially for pulse EPR.
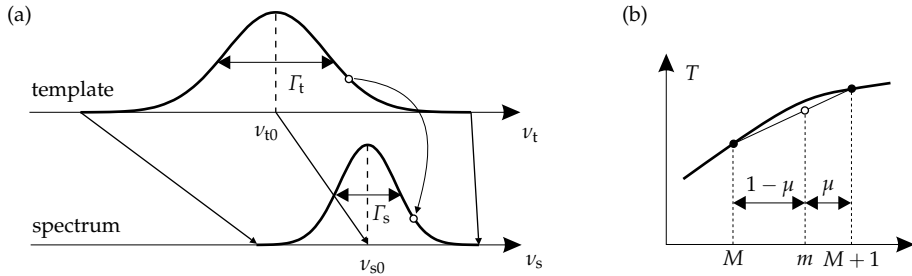
Figure 3.24: Scaled copying of line shapes. (a) Abscissa re-scaling, (b) linear interpolation in the template.

3.3.1 Fast convolution

The convolution of two discrete signals f and g is defined by

$$(f * g)[m] = \sum_{k=-\infty}^{+\infty} f[k]g[m-k] \; . \tag{3.58}$$

For numerical evaluation, one can either use this equation directly or resort to the IDFT/DFT approach

$$s * w = \text{IDFT}\left[\text{DFT}(s)\,\text{DFT}(w)\right] \; . \tag{3.59}$$

In the latter case, a spectral vector s of a certain length N has to be zero-filled to $2N + 1$ points to avoid folding-around of line shapes of peaks near the edges of the spectrum. w is a vector of the same length containing the line shape with its maximum at DFT frequency zero.

3.3.2 Scaled copying

If all the peaks comprising the spectrum have different line widths, there is no way around sampling the associated line shape into the spectral array for each peak separately. The straightforward evaluation of the line shape formula for each peak is simple, but quite time consuming. There is a much more elegant and efficient way to obtain the same result [Hag85a]. This scaled copying approach, as we term it, is illustrated in Figure 3.24.

Template   The method starts by preemptively evaluating the line shape function with an arbitrary line width Γ_t and centre ν_{t0} over a very fine grid (in practice between 10^3 and 10^5 points), thus creating a quasi-continuous template T. The template shape is cut off at points where the function values fall below significance. A Gaussian for example falls below 10^{-3} relative to its maximum at $1.58\,\Gamma_{\text{FWHH}}$ from the centre, a Lorentzian at $15.9\,\Gamma_{\text{FWHH}}$ (see Appendix B).

Copying   This template is then used to construct the line shape in the actual spectrum.

For a peak with amplitude A_p, centre ν_{p0} and line width Γ_p, the abscissa is shifted by the peak offset and re-scaled by the line width ratio using

$$S\left(\nu_p\right) \leftarrow S\left(\nu_p\right) + A_p T\left(\nu_t\right)$$
$$\nu_t = \nu_{t0} + \frac{\Gamma_t}{\Gamma_p}(\nu_p - \nu_{p0}) \ . \tag{3.60}$$

Stepping k by 1 in the discretised spectrum corresponds a step of

$$\alpha = \frac{\Gamma_t/\Delta\nu_t}{\Gamma_p/\Delta\nu} \tag{3.61}$$

in the template. Using this abscissa scaling factor α and starting from the left in the template, a simple iteration adds the correct line shape to the spectrum

$$\begin{aligned}
k &\leftarrow k+1 \\
m &\leftarrow m+\alpha \\
M &\leftarrow \lfloor m \rfloor \\
\mu &\leftarrow m - M \\
S[k] &\leftarrow S[k] + A_p\left((1-\mu)T[M] + \mu T[M+1]\right) \ .
\end{aligned} \tag{3.62}$$

In this way, two adjacent values in T are linearly interpolated to obtain the point needed in S, as shown in Figure 3.24.

The line shape function is evaluated only once to obtain the template and can be even stored and re-used. Only a few multiplications and one rounding are necessary for each point. The speed-up compared to brute-force repeated evaluation is between two and three orders of magnitude. The accuracy of this approach can be increased by increasing the resolution of the template function and by extending its cut-off. Note that the resolution of T does not influence the performance of the method, but the cut-off does. Generalisation to 2D is straightforward. *Performance*

The procedure outlined above corresponds to the sample-and-hold detection (see Figure 3.1). To achieve a boxcar integration, instead of the template its integral has to be used, and differences of template function values have to be added to the spectrum. The iteration procedure has to be modified accordingly. *Detection mode*

The boxcar integration does not lose peaks with line widths smaller than $\Delta\nu$, whereas the sample-and-hold procedure does.

4 Orientations

New in this chapter:

▷ The first correct computation of weighting factors for orientational grids (Section 4.2)

▷ A thorough analysis of homogeneous grid based on correct weighting factors and general merit figures (Section 4.3)

▷ A new homogeneous grid with cubic symmetry superior to all others (Section 4.4.2)

▷ Adaptive grids advantageous for looping transitions, strong orientation selection and anticrossings (Section 4.5)

In this chapter we take a close look at the orientational integral and its numerical approximation by a finite sum over a distribution of orientations. In the first section we describe how integration over all orientations can be limited to certain regions of the sphere and must be numerically approximated by a weighted finite sum. In the second we present a procedure to correctly compute the weighting factors for this sum. Before analysing various published homogeneous grids and a new one in Section 4.4, we take a close look at how to assess the quality of orientational sets. In the last section we introduce a new class of orientational distributions which adapt to the spectral functions being modelled. $\quad$ Outline

4.1 Symmetry

Recall that a powder spectrum is an integral function of single orientation spectra over all possible relative orientations between the molecular and the laboratory frame $\quad$ Powder integral

$$S(y) = \oint s(y, \boldsymbol{\Omega}) \, \mathrm{d}\boldsymbol{\Omega} = \int_0^{2\pi} \int_0^{\pi} \int_0^{2\pi} s(y, \phi, \theta, \chi) \, \mathrm{d}\phi \, \sin\theta \, \mathrm{d}\theta \, \mathrm{d}\chi \; . \qquad (4.1)$$

The integration range is a three-dimensional manifold in 4D space and has the form of a hypersphere with a volume of $8\pi^2$.

This integral cannot be solved except for the few cases shown in Section 3.1.1. In the vast majority of cases, the integral can only be numerically evaluated. It is $\quad$ Approximation

approximated by a weighted sum of a finite number N of orientations

$$S(y) \approx \sum_{k=1}^{N} w_k s(y, \boldsymbol{\Omega}_k) = \sum_{k=1}^{N} w_k s(y, \phi_k, \theta_k, \chi_k) \quad \text{with} \quad \sum_{k=1}^{N} w_k = 8\pi^2, \quad (4.2)$$

where w_k are weighting factors. The set of orientations together with the weights is called orientational *grid*, orientational *mesh* or spherical *code*. Each numerically computed orientation (grid or mesh point, knot) represents some range of nearby orientations in the full integral. The hypersphere is thus subdivided into a number of regions with the points $\boldsymbol{\Omega}_k$ at the centres.

For the multiple integral of Eq. (4.1) there are a host of general methods available from numerical mathematics, but since in magnetic resonance the integrand has some special properties, integration methods can be more specific.

χ integration   In nutation and decoupling experiments, peak positions and amplitudes depend on all three angles, and Eq. (4.2) has to be applied. But for all other experiments (cw EPR, ENDOR and most pulse EPR experiments), peak positions depend only on the first two angles ϕ and θ, so that the integration over the third affects only the amplitudes. The integral over χ can be factored out. For cw EPR and ENDOR it is even possible to solve this integral analytically (see Eq. (2.53) on p. 31). Otherwise, symmetry along this angle can be exploited. It is usually sufficient to integrate from 0 to π. The remaining two-angle surface integral is now much simpler and runs over the unit sphere in intuitive 3D space. Its numerical approximation reads[1]

$$\int_0^\pi \int_0^{2\pi} s(y, \phi, \theta) \, \mathrm{d}\phi \, \sin\theta \, \mathrm{d}\theta \approx \sum_{k=1}^{N} w_k s(y, \phi_k, \theta_k) \quad \text{with} \quad \sum_{k=1}^{N} w_k = 4\pi . \quad (4.3)$$

Inversion symmetry   There exist some symmetry properties allowing the simplification of Eq. (4.3). The symmetry group of a Hamiltonian is defined as the set of symmetry operations which leave the set of eigenvalues of the Hamiltonian invariant. Any EPR spectrum described by the standard spin Hamiltonian is at least invariant under inversion of the external magnetic field[2]

$$H(\boldsymbol{B})|u\rangle = E_u|u\rangle \quad \Longleftrightarrow \quad H(-\boldsymbol{B})|u'\rangle = E_u|u'\rangle . \quad (4.4)$$

Both Hamiltonians have the same eigenvalues, but different eigenvectors. Since eigenvalues determine resonance frequencies and fields, they remain unchanged as well. Transition amplitudes do not change either if $\boldsymbol{B}_1$ is replaced by $-\boldsymbol{B}_1$, since

---

[1] From now on, $\boldsymbol{\Omega}$ denotes just the orientation with angles $(\phi, \theta) = (\phi, \theta, 0)$.

[2] If the interaction operator F is (as usual) invariant under rotation, then F commutes with all components of the sum of all spin operators $\boldsymbol{T} = \sum_m \boldsymbol{S}_m + \sum_k \boldsymbol{I}_k$. A unitary transform with $U = \exp(\mathrm{i}\pi T_z)$ leaves F invariant and transforms $B_0 G_z$ to $-B_0 G_z$. Hence $F + B_0 G_z$ and $F - B_0 G_z$ are unitary equivalent.
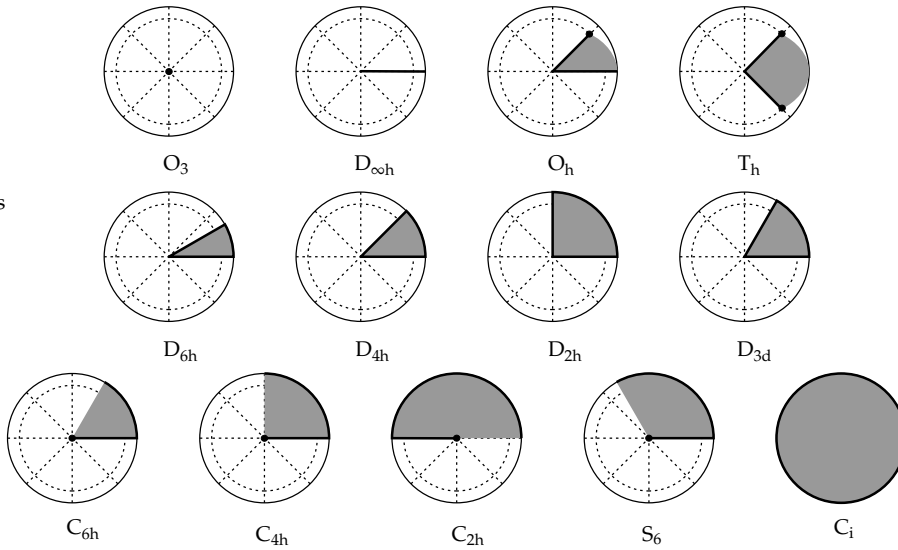
Figure 4.1: Stereographic projection onto the xy plane of unique spherical regions (shaded areas) for all symmetry groups from Table 4.1. A solid border indicates a closed boundary, open boundaries have no border. A dot on the vertex between an open and a closed border of the region indicates that the vertex belongs to the region. The dashed circle corresponds to $\theta = \arctan\sqrt{2} \approx 54.73°$.

the corresponding matrix elements in Eq. (2.50) only change sign. The same result is obtained if *all* vectors are inverted. This is equivalent to time reversal, since both magnetic field and angular momentum vectors involved reverse their direction when time is reversed. The inversion symmetry implies that it is sufficient to integrate only one hemisphere in the (ϕ,θ) subspace, that is, θ runs from 0 to only $\pi/2$ (upper hemisphere).

Often systems exhibit higher symmetry than just the inversion symmetry, and the integration range can be restricted still further to two octants, one octant or even less. This symmetry depends on the symmetry of and the relative orientation between the various interaction tensors and matrices. The resulting unique regions are listed in Table 4.1 and illustrated in Figure 4.1. Conditio sine qua non is that the intensity is already integrated over χ.

Higher symmetry

4.2 Weighting factors

Although the importance of using correct weighting factors w_k in Eq. (4.3) has been emphasised by many workers, they are usually derived only from specific geometric considerations from the grid at hand. The design of grids has been constrained by the inability to generally and analytically compute correct weights.

region	vertices (ϕ, θ)	point groups
4 octants	$(0,0), (0,\pi/2), (2\pi,\pi/2)$	C_i
2 octants	$(0,0), (0,\pi/2), (\pi,\pi/2)$	C_{2h}
4/3 octants	$(0,0), (0,\pi/2), (2\pi/3,\pi/2)$	S_6
1 octant	$(0,0), (0,\pi/2), (\pi/2,\pi/2)$	D_{2h}, C_{4h}
2/3 octants	$(0,0), (0,\pi/2), (\pi/3,\pi/2)$	C_{6h}, D_{3d}
1/2 octant	$(0,0), (0,\pi/2), (\pi/4,\pi/2)$	D_{4h}
1/3 octant	$(0,0), (0,\pi/2), (\pi/4,\pi/4)$	D_{6h}
2/3 octants	$(0,0), (\epsilon,-\pi/4), (\epsilon,\pi/4)$	T_h
1/3 octant	$(0,0), (\epsilon,0), (\epsilon,\pi/4)$	O_h
1/4 meridian	$(0,0), (0,\pi/2)$	$D_{\infty h}$
1 point	$(0,0)$	O_3

Table 4.1: Unique spherical regions on the surface of the unit sphere for all magnetic symmetry groups. See Figure 4.1 for illustration. $\epsilon = \arctan\sqrt{2}$.
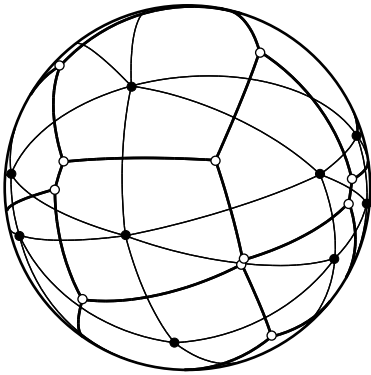
Figure 4.2: Delaunay triangulation (thin lines) and Voronoi tessellation (thick lines) of 15 randomly distributed points (black dots) on the sphere surface. White dots mark the circumcentres of the triangles.

Only recently [Wan95, Bak97] have they received a more general mathematical treatment.

Voronoi cells

Obviously the correct weighting factor w_k of an orientation Ω_k is the sphere surface region containing all points closer to Ω_k than to any other knot. This set of points is a known geometric entity called the *Voronoi cell* V_k of Ω_k. Ω_k is called the generator of the cell V_k. The distance d between two points is measured by the length of the circular arc connecting them, explicitly $d(x,y) = \arccos(x^\mathsf{T}y)$. Voronoi cells are convex spherical polygons. Their edges are arcs of greater circles and equidistant from two generator points, their vertices are equidistant from exactly three generator points. A set of N points generates a Voronoi mesh that divides the unit sphere surface in N Voronoi cells. For details on Voronoi tessellations see [Oka00], a very accessible textbook.

Weights are Voronoi areas

The point Ω_k in a way represents all points from its Voronoi cell in the numerical simulation, and the resulting spectrum has to be added to the total powder

spectrum using the area of the Voronoi cell as weighting factor. For the unit sphere, this area is equal to the solid angle covered by the cell.

A second concept is of importance. Given an arbitrary distribution of points, the computation of the convex hull[1] of this point set in 3D gives the *Delaunay triangulation* of the grid, where neighbouring points are connected by greater circle arcs. The Delaunay triangulation is a realisation of the dual graph of the Voronoi mesh, that is, the number of edges is equal, the number of faces in one graph corresponds to the number of vertices in the other. Edges of the Delaunay triangulation are perpendicular to edges of the Voronoi tessellation (see Figure 4.2).

The Delaunay triangulation on the sphere surface and the convex hull in 3D are only identical if there is no set of four points lying in one plane. In this case the convex hull contains a face with four vertices which, however, can be subdivided into two triangles.

The N-point Voronoi tessellation of the sphere surface is a simply connected graph, meaning that edges do not cross. For such a graph we can apply Euler's formula

$$V + F - E = 2 \,, \tag{4.5}$$

where V is the number of vertices, F the number of faces and E the number of edges. Now every vertex is the junction of three edges, and each edge has 2 vertices, so $2E = 3V$. With the number of faces (cells) $F = N$ we get the number of edges $E = 3N - 6$ and the number of vertices $V = 2N - 4$. From this the average number of edges per Voronoi cell is

$$\langle n \rangle = \frac{2(3N - 6)}{N} = 6 - \frac{12}{N} \,. \tag{4.6}$$

Thus a cell will have six edges on average, but some might have five. The above formula is only valid for a tessellation of the entire sphere surface. For smaller regions the number of points on the border have to be taken into account.

For a given point $\boldsymbol{\Omega}$, the Voronoi cell boundary is the polygon that connects all circumcentres of all triangles of which $\boldsymbol{\Omega}$ is a vertex [Aug85] (see Figure 4.2). The circumcentres of a triangle ABC is

$$\boldsymbol{x}_{\mathrm{cc}}(ABC) = \frac{[\boldsymbol{x}(B) - \boldsymbol{x}(A)] \otimes [\boldsymbol{x}(C) - \boldsymbol{x}(A)]}{|[\boldsymbol{x}(B) - \boldsymbol{x}(A)] \otimes [\boldsymbol{x}(C) - \boldsymbol{x}(A)]|} \tag{4.7}$$

if A, B and C are arranged in counterclockwise order as seen from outside the sphere.

It is relatively easy to compute these Voronoi weights. Bak's and Nielsen's approach [Bak97] is incorrect, since their procedure gives non-convex polygons rather than Voronoi cells. To obtain its area, one has to subdivide a Voronoi cell

---

[1] This is a standard algorithm in computational geometry [Bar96]. See any textbook for details, e.g. [dB97]

PSfrag replacements (a)

(b)
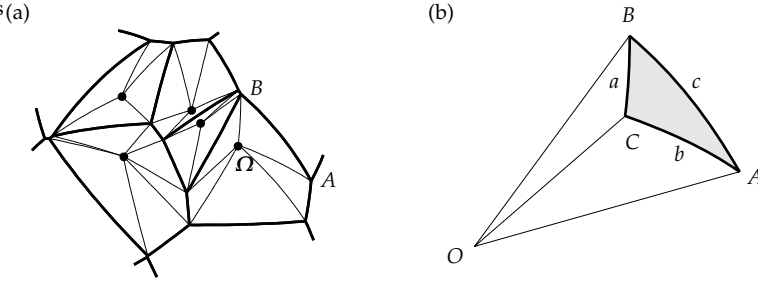
Figure 4.3: Voronoi cell areas. (a) A Voronoi cell consists of several spherical triangles each containing the generator point as vertex. (b) A spherical triangle confined by greater circle arcs.

PSfrag replacements
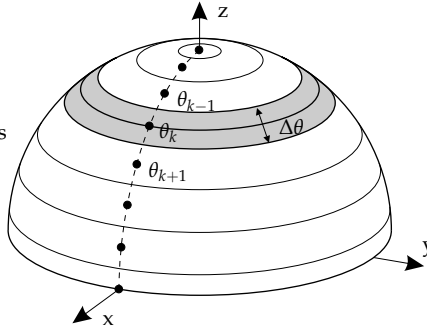
Figure 4.4: Voronoi zones for $D_{\infty h}$ symmetry.

into triangles ΩAB, where A and B are two adjacent cell vertices (see Figure 4.3), and add the areas of the triangles

$$w_k = \sum_{\substack{\text{triangle } r \text{ with} \\ \text{vertex } \Omega_k}} S_r \, . \tag{4.8}$$

A triangle with the edge lengths a, b and c has the area S (formula of l'Huilier [Sig77]) with

$$\tan\left(\frac{1}{4}S\right) = \sqrt{\tan\left(\frac{s}{2}\right)\tan\left(\frac{s-a}{2}\right)\tan\left(\frac{s-b}{2}\right)\tan\left(\frac{s-c}{2}\right)} \tag{4.9}$$

and the perimeter half $s = (a+b+c)/2$.

If less than the full sphere surface is used for the powder integration, the procedure for computing the weights is the same except that at the borders of the unique region (see Figure 4.1) Voronoi cells have to be truncated.

Axial case   The symmetry case $D_{\infty h}$ does not have to be handled by the general concepts

above, because the integration is limited to a quarter of a meridian line (see Figure 4.1). The spectrum of a given orientation $\Omega = (\phi, \theta)$ on this meridian segment is equal to the spectrum at $(0, \theta)$. Therefore the "Voronoi cell" of Ω_k is a spherical zone with the centre ring $\phi = 0 \ldots 2\pi$ and $\theta = \theta_k$. The boundaries of these zones halve the distances between Ω_k and its two neighbours Ω_{k-1} and Ω_{k+1}. The solid angle covered is

$$w_k = 2\pi \left(\cos \frac{\theta_{k-1} + \theta_k}{2} - \cos \frac{\theta_k + \theta_{k+1}}{2} \right) . \tag{4.10}$$

If the distance between the grid points is constant ($\theta_{k+1} - \theta_k = \Delta\theta$), this simplifies to

$$w_k = 4\pi \sin \frac{\Delta\theta}{2} \sin \theta_k . \tag{4.11}$$

The points at the end of the segment need special treatment. For them the weighting factors are

$$w(\theta = 0) = 2\pi \left(1 - \cos \frac{\Delta\theta}{2} \right) \quad \text{and} \quad w(\theta = \pi/2) = 2\pi \sin \frac{\Delta\theta}{2} . \tag{4.12}$$

Thus, the assumption used by many authors that the weighting factor is $\propto \sin \theta_k$ (deduced from the factor in Eq. (4.1)) is wrong for these two points.

4.3 Quality measures

There are many published orientation sets that claim to be efficient. There has been much research into which the optimal point distribution is. Obviously the ideal grid is the distribution of N points that generates the spectrum with the smallest simulation error. This will heavily depend on the spectrum simulated. Since, however, in a general simulation algorithm neither the spectral functions nor their symmetries are known in advance, such optimal grids might perform well for a certain class of spectra and very badly for another one. They cannot be designed in advance without knowledge of some properties of the system to be modelled.

Minimal simulation error

Consequently, a "one-fits-all" grid has to be used, being better for some spectra and suboptimal for others. There are several different criteria along which such grids are usually designed. Since spectral functions can have any orientation and any shape, all resulting grids are quite homogeneous.

One could take the convergence rate (with respect to N) to the theoretical spectrum as a quality measure, as has been done [Pon99a]. As error function Eq. (3.18) (p. 63) is used. As long as correct weighting factors are used, any summation will sooner or later converge. Different parts of a spectrum can converge at different rates. The main problem, however, is that any analysis will depend on some sample spectrum.

Convergence rate

Quadrature grids   There is a class of grids that are designed in a way that the average over all knots of the grid of a spherical harmonic or other polynomial up to a certain degree t is equal to its total integral over the sphere. All w_k are equal. Such quadrature grids have been used extensively for numerical integrations. Recently they have been applied in magnetic resonance as well [Edé98]. The approach assumes that any spectral function is reasonably approximated by a truncated series of spherical harmonics. This is not the case in EPR (e.g. for looping transitions), so the concept is of limited utility.

Rotational invariance   Another at first sight sensible criterion to define the quality of a grid is the rotational invariance of the simulation error [Bak97, Pon99a]. The invariance will however depend on the spectral functions and their symmetry. A rotationally invariant grid ideally gives a simulation error independent of the relative orientation between the M frame of the spin system and the grid. But if there is an alignment between grid and molecular frame that gives results better than an arbitrary alignment, why not use it? In EPR, best results are usually obtained by aligning the grid with the strongest interaction tensor or matrix. For this the grid must have at least a rotation axis and will not be rotationally invariant. In addition, rotational invariance can only be assessed by the study of a sample spectrum.

Homogeneity   All the criteria listed above boil down to the requirement that the grid should be "as homogeneous or uniform as possible", a quantity now independent of any simulated spectrum. A certain degree of homogeneity helps to avoid overdoing spectral features stemming from certain orientations compared to others. There have been some attempts to quantify this homogeneity. Ponti [Pon99a] has used approximate weighting factors, other workers have correctly realised the importance of Voronoi cells [Bak97], but have computed the areas in the wrong way.

After a detailed study, the following three measures have turned out most useful in quantifying the uniformness of an orientational grid.

(1) Voronoi area distribution   The first and most obvious one is the distribution of the areas A_k of the Voronoi cells. This distribution is characterised by a mean $\mu(A)$ and a standard deviation $\sigma(A)$. For a given number of knots N, $\mu(A)$ will be identical for all grids

$$\mu(A) = \langle A \rangle = \frac{1}{N} \sum_{k=1}^{N} A_k = \frac{4\pi}{N} \ . \tag{4.13}$$

On the other hand, the standard deviation

$$\sigma(A) = \sqrt{\langle A^2 \rangle - \langle A \rangle^2} = \sqrt{\frac{1}{N} \sum_k A_k^2 - \mu^2(A)} \tag{4.14}$$

depends on the particular arrangement of points, being zero at best. Thus we can use the relative standard deviation

$$\sigma_{\mathrm{r}}(A) = \frac{\sigma(A)}{\mu(A)} = \sqrt{\frac{N}{16\pi^2} \sum_{k=1}^{N} A_k^2 - 1} \tag{4.15}$$

as a figure of merit. The areas are computed with the formulas given in the previous section. The smaller σ_r, the more homogenous is the grid.

As a second optimality criterion we define a measure that describes the deviation of a Voronoi cell's shape from the spherical cap with the same surface area. For a spherical cap the perimeter $U = 2\pi\sqrt{h(2-h)}$ can be expressed in terms of its surface area $A = 2\pi h$ by

$$U = \sqrt{A(4\pi - A)} \ . \tag{4.16}$$

From this it follows that the parameter

$$\alpha = \frac{U}{\sqrt{A(4\pi - A)}} - 1 \tag{4.17}$$

is zero for spherical caps of all sizes and can be used to quantify the shape distortion. For a Voronoi cell, α is always larger than zero. U is the sum of the arc lengths of the edges, and A is the area obtainable from Eq. (4.8). The mean over all Voronoi cells

$$\mu(\alpha) = \frac{1}{N} \sum_{k=1}^{N} \frac{U}{\sqrt{A(4\pi - A)}} - 1 \tag{4.18}$$

is now an appropriate measure of the average shape distortion. $\mu(\alpha)$ is always larger than zero, and the closer it is to zero, the more spherical the cells are.

Figure 4.5 illustrates the distribution of cell areas and shape parameters for two different grids.

The third figure of merit is often used as minimisation target. It is the electrostatic potential energy of the grid per point

$$E_a = \frac{2}{(N-1)^2} \sum_{k=1}^{N-1} \sum_{l=k+1}^{N} d_a^{-2}(\boldsymbol{\Omega}_k, \boldsymbol{\Omega}_l) \ . \tag{4.19}$$

It is not very critical whether the through-space Euclidean distance d_E or the arc length d_a is used in this formula, since they are monotonically related

$$d_E = 2(1 - \cos d_a) \ . \tag{4.20}$$

The numerical values will be different, but the minimum for one energy will be very close to the minimum for the other one.

The three criteria are independent in the sense that if grid A is better than grid B according to $\sigma_r(a)$, it is not necessarily so when ranked by $\mu(\alpha)$ or E_a. Nevertheless, the rankings of the grids in the next section are similar for the three measures.

There are several other measures in mathematical literature. They are used as error functions which are minimised. Spherical packings are point sets designed to maximise the minimal distance between two points. Spherical coverings are point sets with minimised maximal distance. Some spherical codes are designed to maximise the volume of the convex hull of the points.

(2) Cell shape distortion

(3) Energy

Other criteria
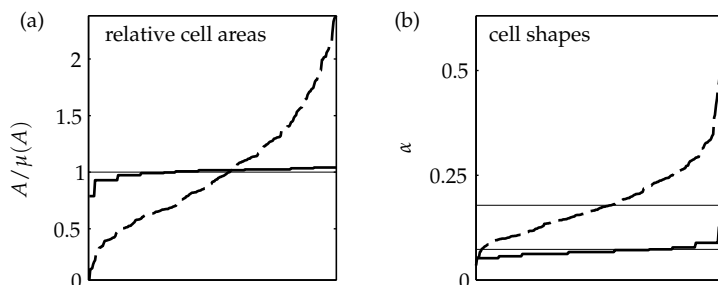
Figure 4.5: Sorted distributions for 258 randomly distributed points (dashed) and a 258-point EasySpin grid (see Section 4.4.2) on the entire sphere surface. (a) Voronoi cell areas relative to the mean (b) Voronoi cell shape parameters. The thin horizontal lines indicate mean values.

4.4 Homogeneous grids

4.4.1 Grids currently in use

There have been many suggestions of spherical grids in the last twenty years. For a rather complete list and for references see the articles by Ponti [Pon99a] and by Bak and Nielsen [Bak97]. Grids can be classified either by their construction method or by their symmetry group. Constructively, grids are grouped into analytical (both orthogonal and non-orthogonal), randomly generated and optimised grids. In the following we briefly describe the most commonly used ones.

Monte Carlo method

The uniform random (Monte Carlo) grid (see Figure 4.6) is the worst one can possibly think of. To obtain a uniform random distribution over the unit sphere, uniform random distributions in the interval $[-1, 1]$ for $\cos\theta$ and in the interval $[0, 2\pi)$ for ϕ are used. The resulting orientational distribution is uniform on the sphere surface, because the projection from the sphere surface to $(\cos\theta, \phi)$ is area-preserving. This means that the uniform knot density in the $(\cos\theta, \phi)$ maps to a uniform knot density on the sphere surface. Of course, the distribution will be uniform only in the limit of infinitely many knots ($N \to \infty$). All quality figures for random grids are very bad, no matter which. In essence, using a Monte Carlo grid is a waste of time. Monte Carlo simulations for orientational integration have indeed been reported rarely [Gal81], but are often taken as reference for the performance of other grids instead of the exact powder shape formulas from Section 3.1.1. The weighting factors are usually assumed to be identical for all points $w_i = 4\pi/N$, but since a distribution is uniform only in the infinite limit, inclusion of Voronoi area weights is recommended. It can reduce the error by up to a factor of 10.

Quasi-random grids

There are a number of grids based on quasi-random (deterministic) generators like the Sobol' algorithm [Pre92]. They are widely used in many fields except magnetic resonance. They are much better than the Monte-Carlo grid, but still
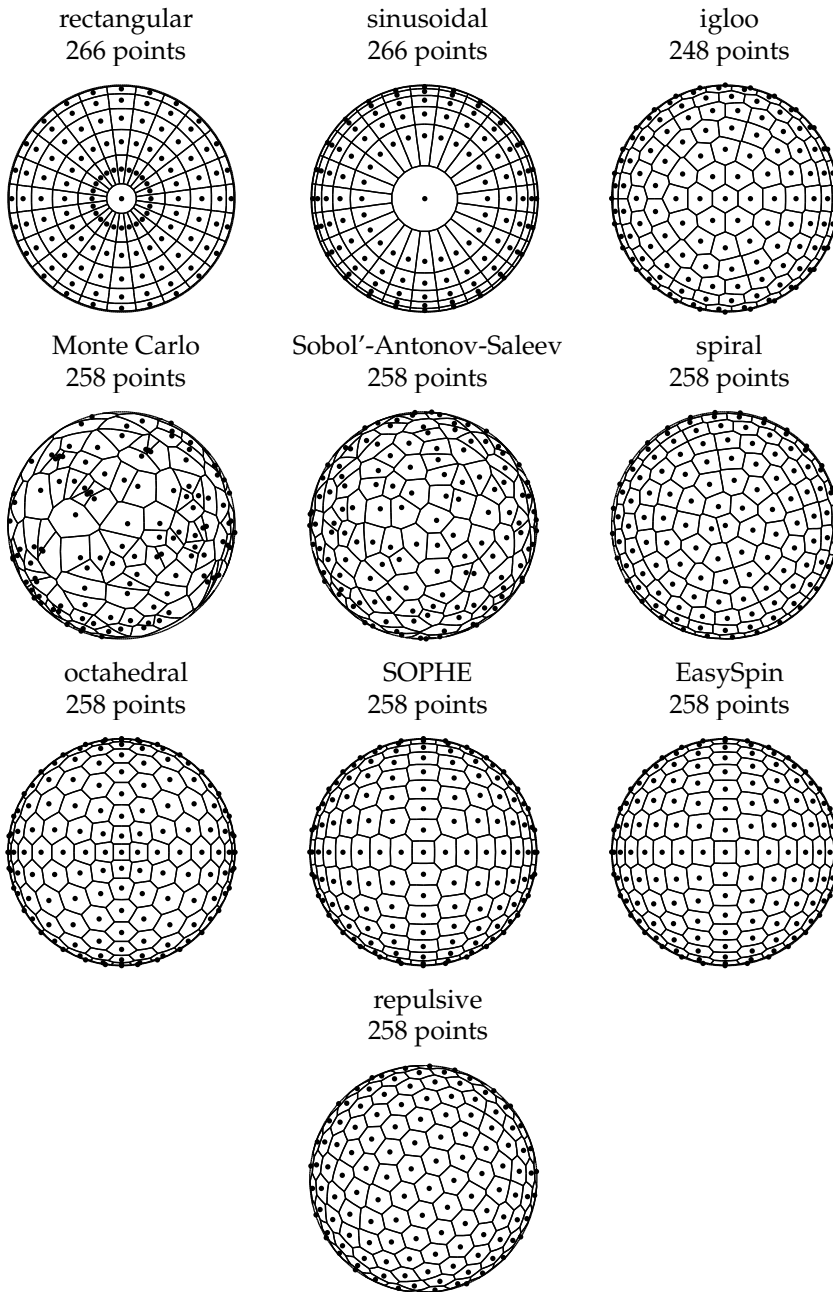
Figure 4.6: Spherical grids with knots and Voronoi cells over the upper hemisphere for approx. 258 points.

worse than any other systematic grid. They construct a uniform grid, which is refined in cycles. Their main advantage is that they can be used in simulations where the number of points is increased in successive steps of grid refinement without clustering effects as would appear using a Monte Carlo grid. For comparison we include here one of these methods by Sobol', Antonov and Saleev [Pon99a] (see Figure 4.6).

Orthogonal grids

Next in inefficiency comes the grid which is the easiest to implement. Distributions of points along θ and ϕ are used to construct a rectangular grid (see Figure 4.6). If linear distributions along θ and ϕ are used [vV78, Gri90], the resulting knot density on the sphere is far from uniform, since it crowds in the pole regions. The areas of Voronoi cells close to the poles are much smaller than those around the equator. Even if the correct weights are included in a simulation, much performance is lost due to the unbalanced emphasis of the poles. If linear distributions of $\cos\theta$ and ϕ are used instead [Ebe83] (sinusoidal grid), Voronoi cell areas are more narrowly distributed (note the outlier at the pole, see Figure 4.6), but their shapes are very far from spherical, so that this grid is already visually counterintuitive. Orthogonal grids have rotational symmetry around the z axis.

Igloo grid

The first analytically constructed non-orthogonal grid published [Nil79] steps θ in constant intervals and adjusts the number of points on the latitude circle $\theta = \text{const}$ to its length

$$\theta_i = \frac{i}{N-1}\pi \qquad 0 \le i \le N-1$$

$$\phi_{ij} = \frac{j}{M_i}2\pi \qquad 0 \le j \le M_i - 1 \quad M_i = \lfloor 4(N-1)\sin\theta_i \rfloor \ . \qquad (4.21)$$

With increasing distance from the pole, an increasing number of points is placed on the latitude circles (see Figure 4.6). This grid is commonly referred to as igloo grid [Nil79, Pil90], although igloos usually are constructed in a spiral form.

Octahedral dome

Alderman et al. [Ald86] have proposed a scheme where a triangulation of the faces of a octahedron is projected onto the sphere enclosing the octahedron. The triangle vertices define the knots of the grid. In geometry and architecture the resulting sphere triangulation is known as a geodesic dome[1]. Here the knot density is again inhomogeneous, now being inappropriately dense on all six poles, that is, where the x, y and z axes cut the sphere. The knots are confined to certain latitude circles, but they are not equidistant as in the igloo grid. The Alderman grid has octahedral symmetry.

SOPHE

A closely related triangular grid was introduced by Wang et al. [Wan95]. Its

---

[1] The concept (based on a icosahedron) was developed and patented by US architect R. Buckminster Fuller after WW II, but Walter Bauersfeld at Carl Zeiss optical works in Jena had already constructed a planetarium in 1922 using the same structure.

grid points are given in an explicit form (here defined for one octant)

$$\theta_{k,l} = \frac{k}{M}\frac{\pi}{2} \qquad\qquad\qquad 0 \leq k \leq M$$

$$\phi_{k,l} = \frac{l}{k}\frac{\pi}{2} \qquad\qquad\qquad 0 \leq l \leq k \qquad (4.22)$$

giving $N = M(M+1)/2$ knots (see Figure 4.6). This so-called SOPHE grid has D_{4h} symmetry. The weights can be computed analytically, and their distribution is much narrower than that of the Alderman grid. The SOPHE grid is particularly suited for interpolation.

The spiral or "apple peal" grid consists of a chain of N points spiralling up   Spiral grid
from the equator $\theta = \pi/2$ to the north pole $\theta = 0$ with constant distance from each other and constant distance to the adjacent turns of the spiral. When it was first introduced in EPR [Mom92], optimisation on a set of nonlinear equations was used to obtain the locations of the knot points. There is, however, a simple closed form for this grid [Pon99a]

$$t_n = \frac{n}{N-1} \quad \theta_n = \arccos t_n \quad \Delta = \sqrt{2\pi(N-1)} \quad \phi_n = \Delta\arcsin t_n \ , \qquad (4.23)$$

where n runs from 0 to $N-1$. The distance measure $(\theta_k - \theta_{k-1})/(\phi_k - \phi_{k-1})$ between two consecutive points k and $k-1$ is constant, whereas the distance on the sphere surface between them decreases slightly towards the pole (see Figure 4.6). The spiral grid is only applicable for C_i symmetry. A very similar grid with two spirals has recently been presented [Gra01].

The grid introduced by to Conroy and Wolfsberg [Koo95] is constructed with   Modulo grid
analytical expressions containing the modulo function. Graphically, it gives a point distribution where more than one spiral is winding up from one pole to the other. It depends not only on N, but on two more parameters. Their optimal values depend strongly on N and have to be tabulated for practical use. This makes the grid a bit unwieldy in simulations where N can be any number.

A class of spherical grids considered to be optimal are energy-minimising grids.   Repulsion
Their knot distributions are results of dynamic simulations trying to find local or   grid
better global energy minima of an electron distribution with the electrons placed at the knot positions on the sphere surface (see Eq. (4.19)). Fittings take quite some time, so that such grids are preferably pre-computed and stored for EPR simulations. For large numbers of knots, the convergence to a minimum is very slow, limiting their applicability to $N < 1000$. There has been extensive research into these kinds of grids. In magnetic resonance they first were applied by Bak [Bak97], with an upper limit of 999 for N. Repulsion grids have C_1 symmetry. They are not suited for interpolation.

Other minimisation grids have already been mentioned in Section 4.3. They have never been applied to spectral simulations in magnetic resonance. They have the same disadvantages as the minimal-energy grids.

PSfrag replacements
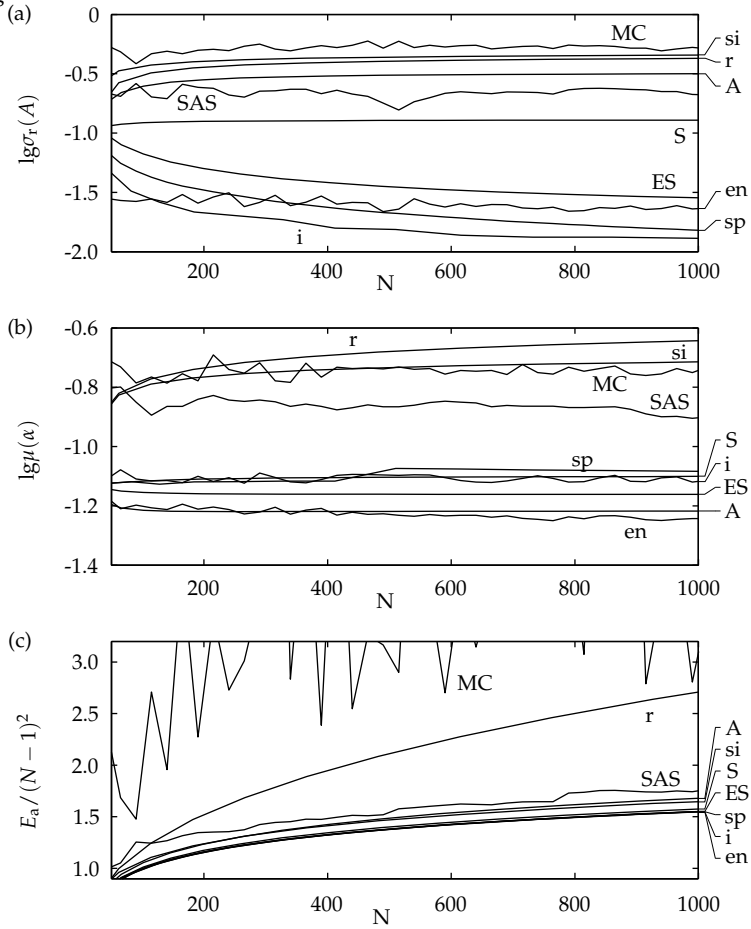
Figure 4.7: Merit figures for all grids. (a) Voronoi cell area distributions, (b) Delaunay triangle area distribution, (c) Coulomb energy. Abbreviations: r rectangular, si sinusoidal, i igloo, MC Monte-Carlo, SAS Sobol'-Antonov-Saleev, sp spiral, A octahedral dome, S SOPHE, ES EasySpin, en minimal energy.

Symmetry	Spherical grid
T_h	Alderman, EasySpin
D_{nh}	orthogonal, sinusoidal
D_{4h}	SOPHE
C_i	spiral, igloo
C_1	Monte Carlo, repulsion, Sobol'-Antonov-Saleev

Table 4.2: Spherical grids classified by their symmetry
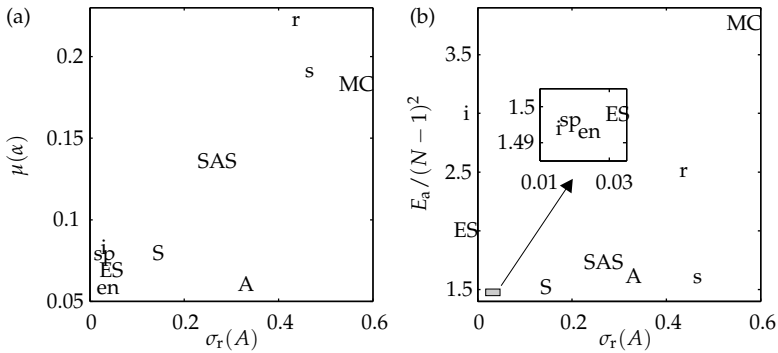
Figure 4.8: Merit figures for grids with $N = 500$. For grids which do not exist for this N, the value was interpolated. (a) $\mu(\alpha)$ vs $\sigma_r(A)$, (b) E_a vs $\sigma_r(A)$.
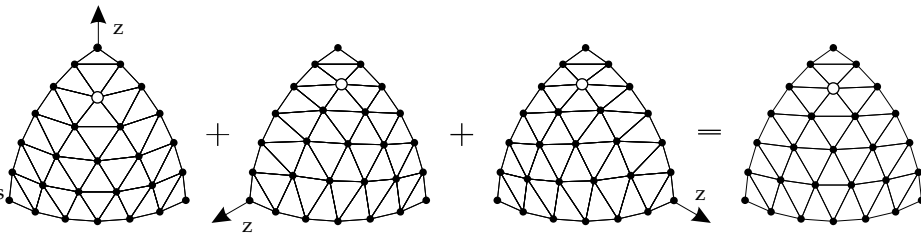
Figure 4.9: Construction of the mean triangular EasySpin grid with octahedral symmetry from three axial triangular grids with different orientations.

4.4.2 A new grid

The Alderman and the triangular SOPHE grid are the only non-orthogonal grids that have a symmetry higher than C_i. Points line up at the borders of the octants, i.e. in the xy, yz and xz planes. This makes them particularly suited for simulation of systems with symmetry planes falling on these octant borders. Since in EPR and ENDOR significant spectral features usually appear at the poles or/and equators of the associated symmetry group, both grids guarantee their inclusion into the spectrum. The Alderman grid is much more inhomogeneous than the SOPHE grid, therefore the latter is currently the best choice.

High symmetry grids

The SOPHE grid is, however, not optimal by the merit figures defined above. Points not falling on octant borders tend towards the equator, especially the point at $(\pi/4, 2\Delta\theta)$ (see Figure 4.6), causing a considerable deviation from the average of the Voronoi cell and triangle areas around the pole.

A new grid with cubic (T_h) symmetry can be constructed by averaging three SOPHE grids constructed around the x, the y and the z axis, respectively, as illustrated in Figure 4.9. The resulting point distribution is much more uniform, since a three-fold rotational axis along $(\pm1, \pm1, 1)^T$ passes through each octant.

EasySpin grid

103

Construction

Explicit formulas for the points of the new EasySpin[1] grid are too clumsy. The following compact procedure can be used instead. In one octant, the point with indices $A = (k, l)$ as defined for the SOPHE grid (Eq. (4.22)) is symmetrically related to the points $B = (M - l, k - l)$ and $C = (M - k + l, M - k)$. The point A' of the new grid is symmetrised using A, B rotated by $2\pi/3$, and C rotated by $-2\pi/3$ around the axis $(1, 1, 1)^{\mathrm{T}}$, which just means cycling the Cartesian coordinates

$$\begin{pmatrix} x_{A'} \\ y_{A'} \\ z_{A'} \end{pmatrix} \propto \begin{pmatrix} x_A \\ y_A \\ z_A \end{pmatrix} + \begin{pmatrix} y_B \\ z_B \\ x_B \end{pmatrix} + \begin{pmatrix} z_C \\ x_C \\ y_C \end{pmatrix} \quad \text{with} \quad \begin{pmatrix} x \\ y \\ z \end{pmatrix} = \begin{pmatrix} \sin\theta\cos\phi \\ \sin\theta\sin\phi \\ \cos\theta \end{pmatrix} . \quad (4.24)$$

The angles θ and ϕ for the three SOPHE points are explicitly

$$\theta_A = \frac{k}{M}\frac{\pi}{2} \qquad \theta_B = \frac{M-l}{M}\frac{\pi}{2} \qquad \theta_C = \frac{M-k+l}{M}\frac{\pi}{2}$$

$$\phi_A = \frac{l}{k}\frac{\pi}{2} \qquad \phi_B = \frac{k-l}{M-l}\frac{\pi}{2} \qquad \phi_C = \frac{M-l}{M-k+l}\frac{\pi}{2} . \quad (4.25)$$

k runs from 0 to M, and l runs from 0 to k. Practically one starts from a SOPHE grid and evaluates Eq. (4.24). The extension to more than one octant is trivial.

Advantages

The EasySpin grid combines the octahedral symmetry of Alderman's grid with the simplicity and homogeneity of the SOPHE grid. The new grid is very similar to an energy-optimised grid with the same number of points, where all points on octant borders are held constant. The maximum deviation of the grid points in Figure 4.9 from those of the corresponding constrained energy-minimal grid is a mere $0.2°$, whereas the SOPHE grid is $5.3°$ off.

4.4.3 Comparison

Two groups

In Figure 4.7 all grids are compared based on the three criteria defined in Section 4.3. The first league with respect to weight homogeneity is formed by the igloo, spiral, energy-minimal and EasySpin grids. The homogeneity of all other grids is significantly worse for $N > 200$, the SOPHE grid being the best among them. According to mean shape deviation, grids clearly fall into two categories, with the Alderman and the SOPHE grid joining the first league. The energies of the various grids are very similar, only the Monte-Carlo and the rectangular grid lie significantly higher than the average.

EasySpin is best

In a two-dimensional comparison (Figure 4.8) the quality difference between energy-minimal, EasySpin, spiral and igloo grids and all others becomes quite clear. Which of the four should now be preferred? The spiral grid is the only one which cannot be used on spherical regions less than one hemisphere (see Section 4.1). In contrast to the EasySpin grid, both energy-minimal and spiral grids are so irregular that interpolation is difficult. In addition, both have low symmetry,

---

[1] We name this new grid after the EPR software package written by the author, in which it was first implemented (see Chapter 5).
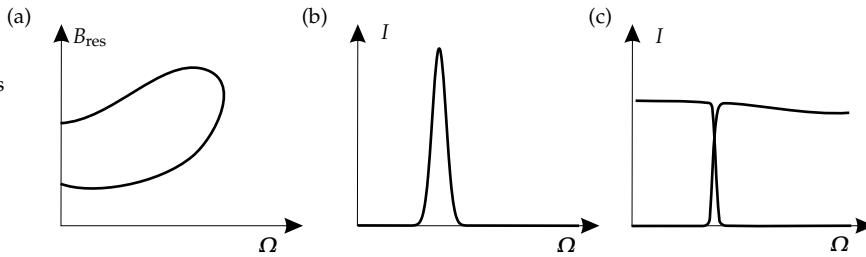
Figure 4.10: Pathological cases for homogeneous grids (schematic). (a) A looping transition, (b) amplitude in a strongly orientation-selective experiment, (c) steep transition amplitude dependence caused by an anticrossing.

whereas the EasySpin grid is cubic. Consequently, the EasySpin grid is the most suited for our purposes.

4.5 Adaptive grids

All the more or less uniform grids presented so far are designed to the basic dogma "equal size, equal shape". The best of them work generally very well, since most orientation-dependent quantities such as resonance fields, ENDOR and ESEEM frequencies, transition amplitudes, coherence transfer amplitudes and anisotropic line widths, are typically very smooth and do not change very much with Ω.

There are, however, situations where the schemes presented above fail to produce correct results or perform very badly. In three cases functions can be more involved (see Figure 4.10). In cw EPR, looping transitions result in resonance field surfaces defined only over a part of the orientational sphere. In spectroscopic methods where the excitation range is much narrower than the total spectral width due to anisotropic interactions, amplitude functions are nonzero for only small mostly banded regions. ENDOR and pulse EPR and indeed all fixed-field fixed-microwave experiments belong to this category. Last not least, anticrossings of states and their energies cause transition and coherence transfer amplitudes to become significantly nonzero only for a part of the orientational sphere, falling with rather steep roll-offs to zero for the rest of the sphere. Anticrossings are quite common.

Pathological cases

These three special situations are usually handled by increasing the grid density to model even the steepest occurring function change accurately. This guarantees that all features in the spectrum are correct, but eats into performance. A typical orientation-selective ENDOR experiment excites only about 10% of all orientations. Computing these at an acceptable accuracy with a homogeneous grid means that the time to compute the non-contributing 90% of the orientations is wasted. Demands on computer memory and speed are higher than necessary.

<div style="float:left; width:15%">Adaptive grids</div>

The obvious answer to the problem is along the lines of Section 2.2.2 and Section 2.8.2. Grids should be used that adapt to the strongly varying function, being as fine as necessary and as coarse as possible to model the function accurately. Such adaptive meshes are industry standard for solving differential equations in Euclidean space with FEM (finite element methods). In magnetic resonance simulations, adaptive grids have not been considered so far[1].

The closest the literature gets to them is in the form of a uniform binary refinement of the grid for an axial system. In each simulation cycle, the number of points is doubled and the spectrum for the new ones computed [Net85]. In this way, the resolution of the homogeneous grid is uniformly increased, until the resolution of the resulting spectrum is satisfactory. Sobol'-Antonov-Saleev grids were developed specifically for this purpose, but have not been applied in magnetic resonance [Pon99a].

4.5.1 Principles

When computing a powder spectrum over one of the homogeneous grids from the last section, peak positions and amplitudes are assumed to be smooth. It is impossible to know in advance whether one of the special situations discussed above will surface[2]. This can only be assessed by looking at already computed data. So the basic procedure needs to pre-compute peaks over a coarse orientational grid before it is possible to decide where and how to refine the grid.

<div style="float:left; width:15%">Keep old data</div>

Since the computation of peak amplitudes and peak positions for an orientation is a quite time-consuming step, peak data of already computed orientations are not discarded. These data are used to determine whether and where to place new knots *and* are included in the final spectrum. Thus the adaptive mesh method introduced here does not move mesh points and adapt a given number of them to the function so as to yield the spectrum with the smallest simulation error. It is adaptive in the sense that the resolution of the grid is locally adapted to the behaviour of the function, thus keeping the number of orientations needed for a certain accuracy at a minimum.

<div style="float:left; width:15%">Recursive subdivision</div>

As starting set a homogeneous grid (preferably the EasySpin grid) of acceptable resolution is needed. Once all its peak data are computed, it is easy to test for each Delaunay triangle whether it is resolved enough or not. If not, it is subdivided into four triangles by placing new knots on the midpoints of the edges (see Figure 4.11(a)). Spectral data are then computed for the three new points, and the four subtriangles are tested again for smoothness. This subdivision procedure is recursively repeated until the peak data are smooth enough over all triangles, a maximum number of orientations is exceeded or a certain number of subdivisions have been completed.

---

[1] The concept of adaptive interpolation presented in [Pon99b] is a somewhat unfortunate term, since the interpolation is linear and not adaptive.

[2] There is an exception: Looping transitions in cw EPR can be excluded if the spectrometer frequency is greater than the total zero splitting, see Eq. (2.33), p. 22.
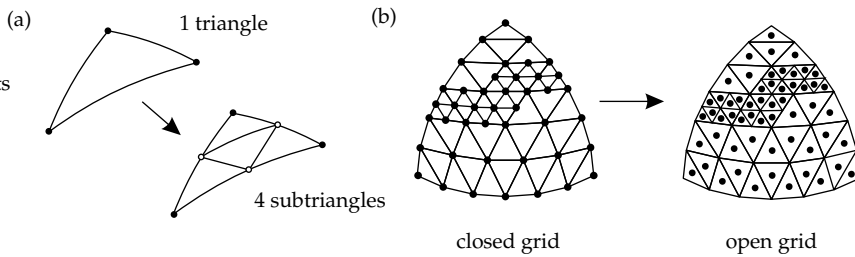
Figure 4.11: (a) Quadrisection of a spherical triangle by inserting three new knots. (b) Conversion of a refined grid from closed to open form.

Although triangle quadrisection halves the edges of a spherical triangle, the resulting four new triangles do not have equal area. In addition, the subdivided triangle is locally re-triangulated according to Figure 4.11(a), but its neighbours now have knots at their edge centres. Obviously, the new grid is not a Delaunay grid anymore. It would be possible to re-triangulate the entire grid, but this is not necessary, as we will see.

Mesh properties

The adapted grid will vary widely in local resolution. Correct weighting factors are now absolutely crucial to obtain reasonable results. Once again we have to distinguish between projective (Section 3.1.4) and additive (Section 3.2.3) spectrum construction methods. For projective methods the spectrum of a triangle is weighted by its area. Since we are still dealing with triangles, these techniques can be applied to adaptive grids without any modification.

Weighting factors

For additive methods the situation is more complicated. Voronoi cell areas are only obtainable from a re-triangulation of the mesh. But there is a much simpler procedure, as illustrated in Figure 4.11(b). For each triangle (for those that remained untouched by the refinement as well), take the average of the peak data over the three vertices and add the peak to the spectrum. As weight the area of the triangle can be used. The averaging of the peak data amounts to the conversion of a closed grid to an open grid, as classified by Ponti [Pon99a]. The principal direction of the g frame, along which the grid is aligned, are averaged away. In ESEEM this is of no relevance, since the corresponding peak amplitudes are very small. For cw EPR spectra with looping transitions and small line widths, this effect can slightly deteriorate accuracy at turning points. If looping transitions are present, the interactions are usually so complex that these turning points do not occur at g principal directions.

Triangle centres

Before we discuss the refinement criteria used to decide whether to subdivide triangles for the various situations, we look at the axial case. Two knots on the meridian define a spherical zone (see Figure 4.4 on p. 94). The refinement decision for the zone depends on the peak data of those two knots, and the zone is refined by placing a new knot at the centre of the corresponding meridian segment. For both projective and additive spectrum construction, Eq. (4.10) is used to compute the weights. For additive spectrum construction the grid is converted

Axial spectra
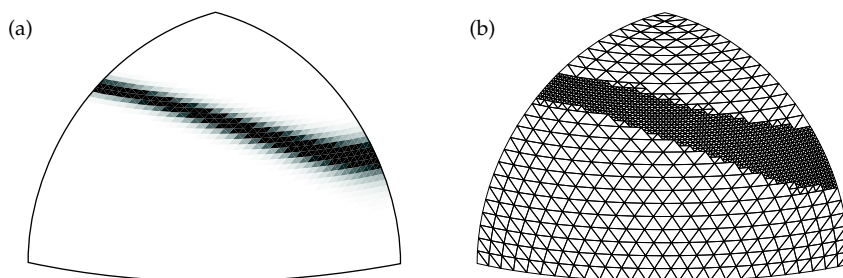
Figure 4.12: (a) Excitation profile for ENDOR or pulse EPR for an orthorhombic system and (b) the associated adapted grid. $\Sigma_{\mathrm{max}} = 15$.

to open form as in the orthorhombic case by averaging data of two neighbouring orientations.

4.5.2 Refinement criteria

Now let us have a look at the adequate tests for deciding on a possible triangle refinement. For a given orientation triangle, all transitions (or a cumulative function) have to be examined, and even if the test results positive for one peak only, the triangle has to be subdivided. So the division decision goes after the worst behaving peak.

Orientation selection

Selectivity

Strong orientation selection occurs if the experimental excitation bandwidth Δ_{exc} (usually Γ_{FWHH} or something similar) is much smaller than the spectral EPR spread $\Delta E_{\mathrm{epr}}(\boldsymbol{\Omega})$, that is, the difference between the highest and lowest EPR transition frequencies. We define the selectivity Σ as

$$\Sigma(\boldsymbol{\Omega}) = \frac{\Delta E_{\mathrm{epr}}(\boldsymbol{\Omega})}{\Delta_{\mathrm{exc}}} \ . \tag{4.26}$$

The EPR spectral spread and consequently the selectivity depends on the orientation of the spin system in the spectrometer. For a typical pulse ENDOR experiment on a Cu^{2+} complex this varies between 2 and 15. The selectivity depends on the magnetic field, so that at W-band the maximum selectivity is $\Sigma \approx 150$. The higher Σ, the less orientations are excited. For the adaptive grid we must assume the worst case and use the maximum selectivity Σ_{max}. It can be estimated by computing the EPR spectral spread at a few selected orientations.

Excitation intensity

Orientation selection occurs in ENDOR and pulse EPR experiments. In both experiments the intensity depends on how much EPR transitions are excited. The

PSfrag replacements
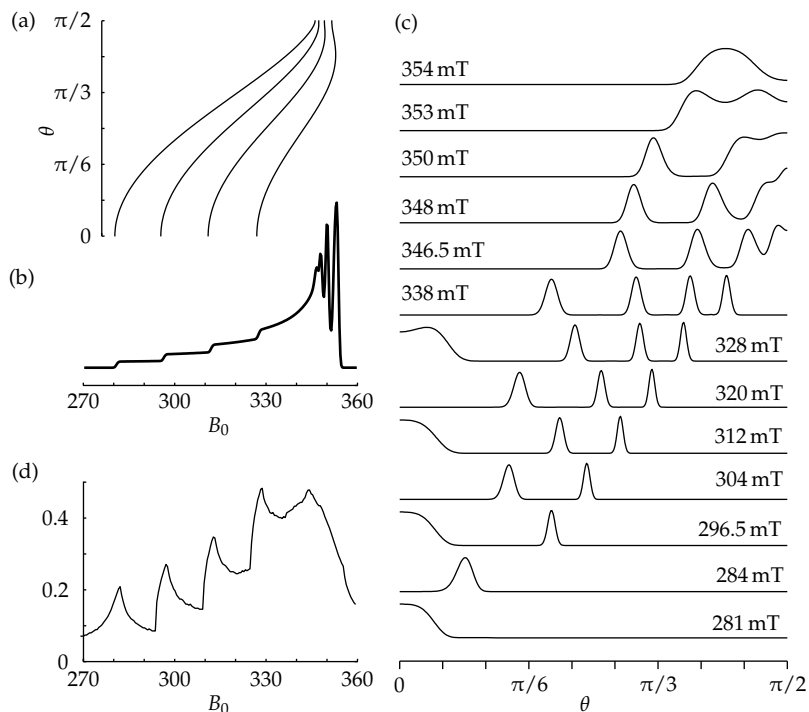
Figure 4.13: Orientation-selective experiment on a Cu^{2+} system (diag$g$ = $(2,2,2.3)$, diag$A$ = $(50,50,500)$ MHz) at X-band (9.797 GHz). Δ_{exc} = 50 MHz. (a) EPR resonance fields in dependence of θ, (b) EPR powder spectrum, (c) EPR excitation function in dependence of θ and the magnetic field, (d) fraction of orientations computed in the adaptive grid method compared to a full resolution homogeneous grid.

EPR excitation intensity function (see Eq. (2.60) on p. 33)

$$I = \sum_{u,v} \sum_q f_G(E_q - E_u, \nu, \Gamma_{mw}) \langle q | G_x | u \rangle \tag{4.27}$$

is thus appropriate as control parameter. For fully excited powder spectra and low selectivity it varies within a small range, but for $\Sigma > 100$ it may change by several orders of magnitude over the orientational sphere.

Procedure   Therefore the first step in the simulation is the computation of peak data over a homogeneous grid fine enough to hit at least once the small region of excitation. For this, knots must have a distance not more than $\frac{\pi}{2}/\Sigma_{max}$. If the EasySpin or SOPHE grid is used, $M = \lceil \frac{\pi}{2}/\Sigma_{max} \rceil$. Then the maximum I_{max} of I over all computed orientations is determined. A triangle with vertex intensities $I_3 \geq I_2 \geq I_1$ is subdivided if its maximum I_3 is above αI_{max} ($\alpha \approx 0.001$) and the relative intensity change over the triangle is larger than a certain threshold

$$\frac{I_3 - I_1}{I_{max}} > \beta \tag{4.28}$$

with $\beta \approx 0.05$. The EPR excitation function and the resulting adapted grid for a simple $S = 1/2$ orthorhombic system is shown in Figure 4.12. More details can be seen in an axial Cu^{2+} example in Figure 4.13. The reduction in computation time can be inferred from Figure 4.13(d).

Thresholds   The use of adaptive grid refinement already helps to avoid a large number of orientations which would be computed on a fine homogeneous grid, but do not significantly contribute to the final spectrum. But even in the adaptive procedure, many of the knots of the uniform starting grid might not contribute. And some of the subdivided triangles might as well have become insignificant during the grid refinement process according to Eq. (4.28), since I_{max} changes during the refinement. All these orientations can be removed before spectral construction by testing whether $A(I_1 + I_2 + I_3)$ (A is the triangle area) falls below a suitably chosen threshold.

Looping transitions

Number of eigenfields   In the case of looping transitions one first checks whether there are orientations with more than one resonance field per transition. If not, adaptive refinement is not necessary and can be either skipped or applied to all triangles. If yes, each triangle has to be tested whether it lies on the boundary of a looping transition. The test parameter is the number of resonance fields n_B for the triangle vertices. If all three vertices have the same number of resonance fields, no subdivision is necessary. If the numbers of resonance fields at the vertices are not all equal (e.g. 12 for two vertices and 10 for the third), a transition loops within the triangle area, and the triangle has to be subdivided. Hence

$$\text{divide} \quad \text{if not} \quad n_B(\Omega_1) = n_B(\Omega_2) = n_B(\Omega_3) \ . \tag{4.29}$$
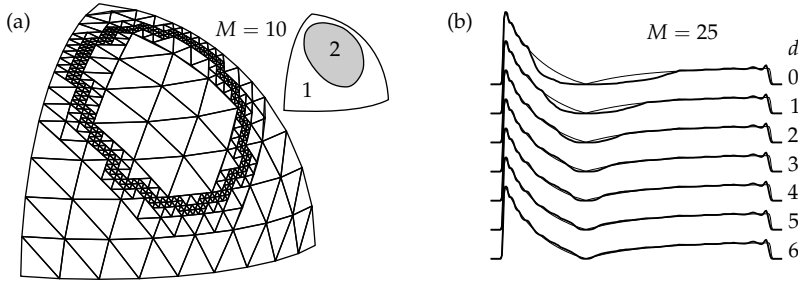
Figure 4.14: (a) An adaptively refined mesh for a looping transition (2 subdivisions). M is the resolution of the starting grid. Small insert: Regions with constant total number of transitions. (b) Effect of adaptive mesh refinement on the spectrum of the looping transition in (a), as a function of the number of subdivisions d. The exact spectrum is printed with a thin line for comparison.

n_B is the *total* number of resonance fields for Ω. It is not necessary to check each transition separately, since the triangle has to be subdivided even if only one transition loops in the triangle region.

Figure 4.14(a) illustrates the mesh refinement for a looping transition. Here the subdivisions were stopped after three iterations. The border of the looping transition is nicely modelled. A series of simulated spectra in Figure 4.14(b) shows that the attained improvement in the centre of the spectrum is significant for the first few subdivision iterations ($d = 1$ or 2), but flattens out as the quadrisections are continued. Convergence to the correct spectrum is very slow as d is increased. More crucial than a lot of subdivisions is the density of the starting grid. It not only should be dense enough to reproduce ordinary transitions, but should also model accurately looping transitions which sometimes occupy only a small fraction of the orientational sphere. For the adaptive refinement at the borders, two steps are then sufficient.

Example

Anticrossings

The steep intensity changes due to anticrossings as pictured in Figure 4.10 (p. 105) need only be closer modelled if interpolation is used. Interpolating on a too coarse grid leads to errors in the spectrum, since the steep roll-off is not reliably modelled. Monotony-conserving interpolation (see Section 2.7) has to be used. For the adaptive grid refinement, the criterion of Eq. (4.28) can be directly applied.

4.5.3 Outlook

The adaptive mesh refinement introduced here is still one step short of completely adaptive meshes, as applied in other areas of science and engineering. There, adaptive meshing is confined to geometric objects. The main obstacle for fully adaptive grid application in EPR is the cost of computation of peak data and the fact that for any orientation the grid must be reasonably adapted not only to *one* scalar function, but for the resonance surfaces *and* transition amplitudes of *many* transitions.

It may, however, be possible to elaborate on the rudimentary but very yielding ideas introduced here. New knots could not only be placed at the edge centres, but anywhere on the edges depending on the data at the vertices. Triangles might be subdivided into 9 or 16 triangles. Still, all these methods would need to adapt the mesh not to only one resonance surface, but on the worst-behaved of a sometimes rather inhomogeneous set.

5 EasySpin

New in this chapter:

▷ A software package for computation of powder cw EPR, ENDOR and
pulse EPR spectra

All concepts and algorithms presented in the previous chapters have been im-
plemented, tested and analysed using Matlab[1], a numerical mathematics pack-
age with its own programming language and visualisation facilities. The most
efficient methods from the previous chapters have been incorporated in a ready-
to-use Matlab function collection called EasySpin, which is freely available over
the Internet including extensive documentation.

EasySpin

The numerical functionality of Matlab covers vector and matrix arithmetics, ei-
genproblems, special functions, optimisation, interpolation and much more. Al-
though Matlab is an interpretative language and Matlab code consequently runs
not as fast as compiled programs from Fortran or C source code, it is convenient
because of its interactivity and consequently the best choice for the prototyping of
new algorithms. Another advantage of Matlab is the possibility to conveniently
integrate spectral simulations, data analysis, fitting and visualisation.

Matlab and C

On the other hand, finalised simulation algorithms are best implemented in a
compiled language such as C, where computations can run up to 50 times faster
due to reduced overheads. There exist special C libraries for spin physics, the
most extensive being the C class libraries Γ [Smi94] and BlochLib [Bla02]. But
much of their functionality is not needed in EPR. In addition, many algorithms
introduced in this PhD thesis operate on scalars or vectors and not on higher-level
objects such as operators and tensors. The only spin physical operations needed
are eigenproblem solutions and matrix exponentiation, which are readily avail-
able on any numerical platform. Although the C libraries mentioned provide an
easy and very convenient interface for performing time-domain pulse EPR simu-
lations [Sha98, Mád02], their classes are not suited for the implementation of the
frequency-domain approach described in Section 2.5.

The core algorithms of EPR spectral simulations are very simple (the projection
methods of Section 3.1.4, the scaled copying of Section 3.3.2, the convolution ap-
proximation of Section 3.2.3), but very time-consuming. Most of the time needed

Core in C

---

[1] Matlab is produced by The Mathworks, Inc., Natick, MA, USA, http://www.mathworks.com.
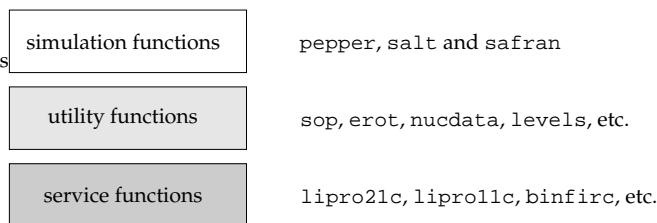
Figure 5.1: Three categories of functions in EasySpin.

for simulation of a powder EPR spectrum is spent on them. To improve performance, their final versions have been incorporated into EasySpin as library functions written in C (so-called mex files) to improve the overall performance.

Therefore, EasySpin is a Matlab toolbox with a very efficient C kernel. Powder simulations spend more than 90% of the time either in highly speed-optimised Matlab built-in functions or in the EasySpin kernel functions written in C. Converting the entire toolbox to C is not necessary, since the gain in performance would be marginal.

In the following we briefly describe the EasySpin toolbox. More details can be found in the manual, in the examples accompanying the software and in the source code documentation.

5.1 General concept

EasySpin is a collection of functions. They fall into three distinct categories, as illustrated in Figure 5.1.

Service functions

Most algorithms are implemented in private *service* functions not directly available to the user. They include `lipro21c` and `lipro11c` for non-axial and axial projections (Section 3.1.4), `lisum1c` for scaled copying (Section 3.3.2), `binidxc` for histogram binning (Section 3.2.2) and the function `binfirc` for the convolution method of Section 3.2.3. There are also several interpolation functions in this group.

Utility functions

For interactive use, more than 50 *utility* functions providing elementary spin physics functionality are included. `sop` computes spin operators for any set of spins. `erot` and `eulang` convert between Euler angles and the associated rotation matrices. `levels` computes energy levels for a given set of orientations and magnetic fields. `nucdata`, `nucgval` and `nucspin` contain a database of nuclear spin quantum numbers and g_n values. `pseumod` implements the procedure of pseudo-modulation discussed on p. 60. `lshape`, `gaussian` and `lorentzian` provide line shapes and their derivatives. `rcfilt` performs the RC filtering of Eq. (3.4). `eigfields`, `resfields` and `endorfrq` compute resonance fields, resonance frequencies and transition intensities for cw EPR and ENDOR. Various

utilities for data analysis such as `ctafft` for cross-term averaged FFT [Van99] are provided, as well as apodization windows and other filters.

The third layer of functionality is provided by the *simulation* functions `pepper`, `salt` and `safran`. They compute powder spectra for cw EPR, ENDOR and pulse EPR, respectively. They are built on service and on utility functions and are by far the most complex in the toolbox.

<div style="text-align: right">Simulation functions</div>

5.2 Spectral simulations

The powder spectrum computations performed by `pepper`, `salt` and `safran` work according to the scheme outlined in Section 1.1.2. The calling syntax for them is similar

<div style="text-align: right">Syntax</div>

```
[FieldAxis,Spectrum] = pepper(System,Params,Options) % cw EPR
[rfAxis,Spectrum]    = salt(System,Params,Options)   % ENDOR
[ftAxis,Spectrum]    = safran(System,Params,Options) % pulse EPR
```

The output contains the abscissa vector(s) and the spectral data vector or matrix. The input is organised in three structures. `System` collects all parameters of the spin system such as the number and quantum numbers of the spins and the parameters in Section 1.2. In addition, it contains strain values and line width parameters (Section 1.3 and Section 2.3). `Params` specifies the experimental parameters, such as the sweep range of the magnetic field or the radio frequency, the temperature, the detection mode ($B_1 \perp B_0$ or $B_1 \| B_0$), the excitation width (for ENDOR), and the pulse sequence in the case of pulse EPR. The `Options` structure collects parameters determining the behaviour of the simulation algorithm such as the resolution of the orientational grid, the interpolation factor and various rejection thresholds. Transitions can be selected via an explicit list or an intensity threshold.

<div style="text-align: right">Output and input</div>

With a given `System` structure, `pepper`, `salt` and `safran` first automatically determine the symmetry group and the symmetry frame of the spin system (see Section 4.1). The powder spectrum simulation is performed in the frame with the highest symmetry using the unique orientational regions according to Table 4.1. All interaction matrices and tensors are rotated into the symmetry frame, where the spin Hamiltonian is set up.

<div style="text-align: right">Symmetry</div>

Next, an orientational grid is set up in the symmetry frame. For axial symmetry, a quarter of a meridian is used as illustrated in Figure 4.4 on p. 94. For non-axial symmetries, the triangular EasySpin grid (Section 4.4.2) is used. For cw EPR and ENDOR spectra, a resolution with $M < 20$ (see Eq. (4.25) on p. 104) is sufficient. For pulse EPR, $60 < M < 120$ is needed to achieve a smooth powder line shape. The large resolution is necessary because in pulse EPR the grid serves as inhomogeneous distribution for the computation of correct amplitudes as discussed in Section 2.5.4.

<div style="text-align: right">Grid</div>

For a small subset of orientations, all spectral peaks are computed. Based on

<div style="text-align: right">Transition selection</div>

the orientational average of the resulting intensity data a list of transitions significantly contributing to the final spectrum is compiled (see Section 2.8.1). This automatic selection process can be configured by the user by specifying a relative intensity threshold or bypassed by supplying an explicit list of transitions.

Peaks
For the rest of the orientations, spectral data are computed only for the selected transitions. Peaks are calculated according to the formulas outlined in Chapter 2. For cw EPR, `pepper` uses the adaptive bisection approach of Section 2.2.2. For the ENDOR simulation function `salt`, the expressions from Section 2.4.1 and Section 2.4.2 are used. Pulse EPR peaks are computed by `safran` in frequency domain using the equations from Section 2.5 and Section 2.6 and the adaptive thresholding mechanism outlined in Section 2.8.2.

Interpolation
The peak list (see Eq. (1.1) and Eq. (1.2)) thus obtained is interpolated using global cubic splines for peak positions and linear interpolation for peak amplitudes (Section 2.7). If anisotropic widths due to strains were computed, the widths are interpolated linearly as well. For axial symmetry, the interpolation is trivial. For non-axial symmetry, it proceeds in three steps. First the triangular grid is interpolated to a rectangular one with the same number of knots on the equator $\theta = \pi/2$. Second a two-dimensional tensor-product spline representation of the surface is constructed using the information about orientational gradients at the borders of the unique region used (Table 4.1). Third, this surface is evaluated for the knots of a higher resolution triangular EasySpin grid. Using this procedure, the number of orientations is usually increased by a factor up to 100.

Spectrum construction
Starting from the interpolatively enlarged peak list, peaks with negligible amplitude are removed (Section 2.8) and the various spectrum construction methods from Chapter 3 are applied. For cw EPR and ENDOR, the choice depends on the presence of anisotropic line broadening. If it is absent, the projective methods from Section 3.1.4 are used, otherwise scaled copying (Section 3.3.2) and gradient-weighted accumulation (Section 3.1.3) are used. For pulse EPR spectra, the convolution method of Section 3.2.3 is applied.

Convolution
If selected by the user, a purely phenomenological line broadening in the spectral domain is added by convolution. The corresponding line width is specified in `System.lw` (for cw EPR, in mT), in `System.lwEndor` (for ENDOR, in MHz) and in `System.lwEseem` (for pulse EPR, in MHz). It is convoluted with the final stick spectrum.

5.3 Some examples

In the following some illustrative examples of the use of EasySpin utility and simulation functions are given.

Spin operators
Spin operators are computed using the function `sop` (see Appendix A for formulas). It takes as parameters the vector of the spin quantum numbers and a string specifying the components (one letter from the set `xyz+-e` for each spin).

A simple example is

```
SxIy = sop([1/2 1/2],'xy') % two spins-1/2

SxIy =

    0              0              0          0 - 0.25i
    0              0          0 + 0.25i      0
    0          0 - 0.25i          0          0
0 + 0.25i          0              0          0
```

Spin systems are specified via a structure collecting all spin Hamiltonian para- | Spin
meters. There are several functions for constructing the spin Hamiltonian or se- | Hamiltonians
lected parts of it. The following code defines the spin system from Figure 2.5 and
extracts the zero-field splitting part.

```
b = -2527.53/60; c = -24.84/1260; % in units of MHz
TbSys = struct('S',7/2,'g',[1 1 1]*2.0136,...
  'B40',b,'B44',[5*b 0],'B60',c,'B64',[-21*c 0]);
zfield(TbSys) % zero field splitting part

ans =

1.0e+04 *

-1.7718        0        0        0  -1.4512        0        0        0
     0   3.2982        0        0        0  -2.2190        0        0
     0        0   0.7359        0        0        0  -2.2190        0
     0        0        0  -2.2624        0        0        0  -1.4512
-1.4512        0        0        0  -2.2624        0        0        0
     0  -2.2190        0        0        0   0.7359        0        0
     0        0  -2.2190        0        0        0   3.2982        0
     0        0        0  -1.4512        0        0        0  -1.7718
```

The field-independent spin Hamiltonian components of Eq. (2.7) on p. 15 can be
obtained by calling sham

```
[F,GxM,GyM,GzM] = sham(TbSys);
```

The function erot computes the rotation matrix associated with a set of three | Euler angles
Euler angles as specified in Appendix C.

```
R = erot(pi./[3 4 5])

R =

  -0.2230    0.7893   -0.5721
  -0.9084    0.0446    0.4156
   0.3536    0.6124    0.7071
```

The inverse function eulang extracts the Euler angles from *R*

```
>> eulang(R)

ans =

   1.0472    0.7854    0.6283
```

Energy levels

With the function `levels` energy levels as a function of magnetic field orientation and magnitude can be computed. The following code produces the level diagram underlying Figure 2.5 on p. 27.

```
extB = linspace(0,2500,200); % mT
E = levels(TbSys,45*pi/180,4*pi/180,extB);
plot(extB,E);
xlabel('magnetic field [mT]');
ylabel('energy [GHz]');
```

Eigenfields

The function `eigfields` uses the eigenfield method of Section 2.2.1 (p. 21) to obtain resonance fields and amplitudes. The code

```
Params.mwFreq = 10; % in GHz
Orientations = [0;0]; % [phi;theta]
[ResFields,Amplitudes] = eigfields(ThSys,Params,Orientations);
line([ResFields ResFields]',[zeros(size(ResFields)) Amplitudes]');
```

directly produces a cw EPR stick spectrum with correct amplitudes.

cw EPR spectra

cw EPR spectra are computed by the function `pepper`. A simple example of an $S = 1/2$ system with *g* strain is given below. The effect of magnetic field modulation (see p. 60) is included by a call to the function `pseumod`

```
Sys = struct('S',1/2,'g',[2.1 2 1.9]);
Sys.gStrain = [.02 .005 .05];
Exp = struct('Range',[300,380],'mwFreq',9.5); % mT and GHz
Opt.nKnots = 6; Opt.nSpline = 4; % orientational grid resolution

[Fields,Spec] = pepper(Sys,Exp,Opt);
spectrum = pseumod(Fields,Spec,0.5); % modulation amplitude in mT

plot(Fields,Spec);
xlabel('magnetic field [mT]');
```

The fields `nKnots` and `nSpline` in the options structure specify the number of knots along a quarter of a meridian (*M* in Eq. (4.25) on p. 104) and the interpolation factor, respectively.

ENDOR spectra

The function `salt` computes ENDOR spectra. The input code for a simple example is

```
Sy = struct('S',1/2,'I',1,'g',[2.25 2.25 2],'gn',nucgval('14N'),...
  'A',48+4*[-1 -1 2],'Apa',[0 pi/4 0],'Q',-.84*[-1 -1 2],...
  'HStrain',[1 1 1],'lwEndor',.7);
Ex = struct('Range',[16,33],'Field',308.46,...
  'nPoints',512,'mwFreq',9.681,'ExciteWidth',200);
Op = struct('Threshold',1e-4,'nKnots',10);

[x,y] = salt(Sy,Ex,Op);
```

the field `Apa` in the system structure `Sy` specifies the Euler angles for the orientation of *A* in the *g* frame. In addition, there are more line width specifiers than in the cw EPR case. The field `HStrain` defines a general distribution of spin Hamiltonian eigenvalues due to unresolved hyperfine couplings. `lwEndor` is a pure convolutional line width which is added to the simulated stick spectrum.

`ExciteWidth` in the experiment structure gives the excitation width in units of MHz.

The function `safran` can compute the time-domain signal of any pulse EPR experiment. The most common experiments like two-pulse and three-pulse ES-EEM and HYSCORE are pre-defined, for the others the pulse sequence and the incrementation scheme (see Section 2.5.3) can be specified explicitly. For example, the HYSCORE spectrum in Figure 3.23(b) was computed using the code

```
eta = 0.5; P = 2.4/4;
System = struct('S',.5,'g',2,'I',1,'gn',nucgval('14N'),...
        'A',5,'Q',P*[-(1-eta) -(1+eta) 2],'HStrain',0.1);
dt = 0.05; % in microseconds
Params = struct('mwFreq',9.797369,'Field',350,'Sequence','HYSCORE',...
        'tau',.136,'nPoints',256,'dt',dt,'tp',.01);
Options = struct('nOffset',2,'nKnots',91,...
        'BinThreshold',5e-3,...
        'SimulationFrame','rot');

td = safran(System,Params,Options);
```

`td` now contains the pulse EPR time-domain signal. A few more lines of code produce the magnitude spectrum by base-line correction, apodization, zero-filling and Fast Fourier Transform.

```
w = apodize([],Params.nPoints,2*pi);
td = (td - mean(td(:))).*(w*w');
spec = fftshift(fft2(td,size(y,1)*2,size(y,2)*2));
spec = abs(spec(1:2:end,1:2:end));
```

A Spin operators

This appendix collects formulas for all spin operators necessary to set up the EPR spin Hamiltonian and perform spectral simulation. It is compiled mainly for the convenience of the reader.

Spin vectors are usually represented in terms of their Hermitian cartesian component operators S_x, S_y and S_z. Sometimes, the non-Hermitian operators $S_+ = S_x + iS_y$ and $S_- = S_x - iS_y$ are used Spin vectors

$$S = \begin{pmatrix} S_x \\ S_y \\ S_z \end{pmatrix} = \begin{pmatrix} (S_+ + S_-)/2 \\ (S_+ - S_-)/2i \\ S_z \end{pmatrix} . \tag{A.1}$$

For a spin S the component operators are matrices of dimension $2S + 1$. They are always represented in the Zeeman basis with states $|S, m\rangle$ ($m = -S, \ldots, S$) or in short $|m\rangle$ that satisfy Zeeman basis

$$\langle m'|S_x|m\rangle = (\delta_{m+1,m'} + \delta_{m,m'+1})\frac{1}{2}\sqrt{S(S+1) - m'm} \tag{A.2}$$

$$\langle m'|S_y|m\rangle = (\delta_{m'+1,m} - \delta_{m,m'+1})\frac{1}{2i}\sqrt{S(S+1) - m'm} \tag{A.3}$$

$$\langle m'|S_z|m\rangle = \delta_{m',m}m \tag{A.4}$$

$$\langle m'|S_+|m\rangle = \delta_{m+1,m'}\frac{1}{2}\sqrt{S(S+1) - m'm} \tag{A.5}$$

$$\langle m'|S_-|m\rangle = \delta_{m,m'+1}\frac{1}{2}\sqrt{S(S+1) - m'm} . \tag{A.6}$$

The basis states in the matrices are in descending m order $|S\rangle, |S-1\rangle, \ldots, |-S\rangle$. Spin operator matrices for single spins are easy to construct. S_z is a diagonal matrix with $S, S-1, \ldots, -S$ on its main diagonal. For the other four operators, all elements except the upper or lower diagonals are zero. Along these diagonals the values are Matrices

$$d_k = \sqrt{k(2S+1-k)} \qquad k = 1, 2, \ldots, 2S , \tag{A.7}$$

or in a more explicit form

$$
\begin{array}{ll}
S = 1/2 & \sqrt{1} \\
S = 1 & \sqrt{2} \quad \sqrt{2} \\
S = 3/2 & \sqrt{3} \quad \sqrt{4} \quad \sqrt{3} \\
S = 2 & \sqrt{4} \quad \sqrt{6} \quad \sqrt{6} \quad \sqrt{4} \\
S = 5/2 & \sqrt{5} \quad \sqrt{8} \quad \sqrt{9} \quad \sqrt{8} \quad \sqrt{5}
\end{array}
\tag{A.8}
$$
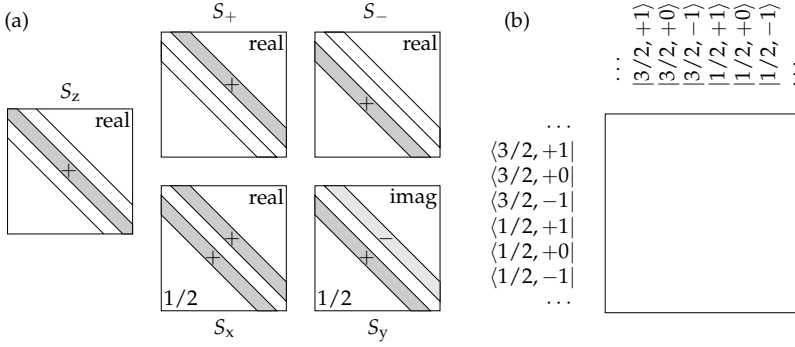
Figure A.1: Spin operator matrix representations in the Zeeman basis. (a) Matrices of the various operators. Only shaded areas are non-zero and contain the elements from Eq. (A.7). (b) State ordering in matrices for a two-spin system with $S_1 = 3/2$ and $S_2 = 1$.

For S_+ (S_-) only the upper (lower) diagonal is non-zero. S_x and S_y are the linear combinations of S_+ and S_- as given in Eq. (A.1). This is illustrated in Figure A.1.

The cartesian operators for $S = 1/2$, $S = 1$ and $S = 3/2$ are

$$S_x = \frac{1}{2}\begin{pmatrix} 0 & 1 \\ 1 & 0 \end{pmatrix} \quad S_y = \frac{i}{2}\begin{pmatrix} 0 & -1 \\ 1 & 0 \end{pmatrix} \quad S_z = \frac{1}{2}\begin{pmatrix} \frac{1}{2} & 0 \\ 0 & -\frac{1}{2} \end{pmatrix} \tag{A.9}$$

$$S_x = \frac{1}{2}\begin{pmatrix} 0 & \sqrt{2} & 0 \\ \sqrt{2} & 0 & \sqrt{2} \\ 0 & \sqrt{2} & 0 \end{pmatrix} \quad S_y = \frac{i}{2}\begin{pmatrix} 0 & -\sqrt{2} & 0 \\ \sqrt{2} & 0 & -\sqrt{2} \\ 0 & \sqrt{2} & 0 \end{pmatrix} \quad S_z = \begin{pmatrix} 1 & 0 & 0 \\ 0 & 0 & 0 \\ 0 & 0 & -1 \end{pmatrix} \tag{A.10}$$

$$S_x = \frac{1}{2}\begin{pmatrix} 0 & \sqrt{3} & 0 & 0 \\ \sqrt{3} & 0 & \sqrt{4} & 0 \\ 0 & \sqrt{4} & 0 & \sqrt{3} \\ 0 & 0 & \sqrt{3} & 0 \end{pmatrix} \qquad S_y = \frac{i}{2}\begin{pmatrix} 0 & -\sqrt{3} & 0 & 0 \\ \sqrt{3} & 0 & -2 & 0 \\ 0 & 2 & 0 & -\sqrt{3} \\ 0 & 0 & \sqrt{3} & 0 \end{pmatrix}$$

$$S_z = \frac{1}{2}\begin{pmatrix} \frac{3}{2} & 0 & 0 & 0 \\ 0 & \frac{1}{2} & 0 & 0 \\ 0 & 0 & -\frac{1}{2} & 0 \\ 0 & 0 & 0 & -\frac{3}{2} \end{pmatrix} . \tag{A.11}$$

The cartesian operators are orthogonal and satisfy

$$\mathrm{tr}(S_k S_l) = \frac{1}{3}S(S+1)(2S+1)\delta_{kl} \qquad k,l = x,y,z . \tag{A.12}$$

Product basis　　Zeeman states of a spin system with more than one spin are the tensor product of the states of the individual spins

$$|S, m_S, I, m_I\rangle \equiv |m_S, m_I\rangle = |m_S\rangle \otimes |m_I\rangle \tag{A.13}$$

Table A.1: Extended Stevens operators $O_k^q(S)$. The notation $[A, B]_+$ indicates the anticommutator $AB + BA$, and $s = S(S+1)$, $c_+ = 1/4$, $c_- = -i/4$. Taken from Appendix V (p. 512) of [Alt74], compatible with Table 16 (p. 863) from [Abr86].

k	q	$O_k^q(S)$
2	0	$3S_z^2 - s\mathbb{1}$
	± 1	$c_\pm [S_z, S_+ \pm S_-]_+$
	± 2	$2c_\pm (S_+^2 \pm S_-^2)$
4	0	$35S_z^4 - (30s - 25)S_z^2 + (3s^2 - 6s)\mathbb{1}$
	± 1	$c_\pm [7S_z^3 - (3s+1)S_z, S_+ \pm S_-]_+$
	± 2	$c_\pm [7S_z^2 - (s+5)\mathbb{1}, S_+^2 \pm S_-^2]_+$
	± 3	$c_\pm [S_z, S_+^3 \pm S_-^3]_+$
	± 4	$2c_\pm (S_+^4 \pm S_-^4)$
6	0	$231S_z^6 - (315s - 735)S_z^4 + (105s^2 - 525s + 294)S_z^2 - (5s^3 - 40s^2 + 60s)\mathbb{1}$
	± 1	$c_\pm [33S_z^5 - (30s - 15)S_z^3 + (5s^2 - 10s + 12)S_z, S_+ \pm S_-]_+$
	± 2	$c_\pm [33S_z^4 - (18s + 123)S_z^2 + (s^2 + 10s + 102)\mathbb{1}, S_+^2 \pm S_-^2]_+$
	± 3	$c_\pm [11S_z^3 - (3s + 59)S_z, S_+^3 \pm S_-^3]_+$
	± 4	$c_\pm [11S_z^2 - (s + 38)\mathbb{1}, S_+^4 \pm S_-^4]_+$
	± 5	$c_\pm [S_z, S_+^5 \pm S_-^5]_+$
	± 6	$2c_\pm (S_+^6 \pm S_-^6)$

Spin operators of the the two-spin system are tensor products as well, e.g. $S_x \otimes I_z$ or $\mathbb{1}_{2S+1} \otimes I_y$.

These tensor products are computed using the Kronecker product

$$
A \otimes B = \begin{pmatrix} A_{11}B & A_{12}B & \cdots & A_{1m}B \\ A_{21}B & A_{22}B & \cdots & A_{2m}B \\ \vdots & \vdots & & \vdots \\ A_{n1}B & A_{n2}B & \cdots & A_{nm}B \end{pmatrix} \tag{A.14}
$$

Kronecker product

where A and B can be vectors (states) or matrices (operators). The standard ordering of the product states is illustrated in Figure A.1(b).

For higher-order terms in the spin Hamiltonian a plethora of different operator sets exists. For an enlightening discussion of them and the confusion in the literature, see [Rud01]. The most common definition

Higher-order terms

$$
\mathcal{H}_{ZF}(S)/h = H_{ZF}(S) = \sum_{k=2,4,6} \sum_{q=-k}^{k} B_k^q O_k^q(S) \tag{A.15}
$$

uses the extended Stevens operators[1] O_k^q and real coefficients B_k^q. Sometimes normalised coefficients $b_k^q = B_k^q/f_k$ with $f_2 = 1/3$, $f_4 = 1/60$ and $f_6 = 1/1260$ are used. $O_k^q(S)$ are polynomials in S and are Hermitian. They are listed in Table A.1. If $q \geq 0$, $O_k^q(S)$ is real, else imaginary. This behaviour is analogous to S_x and S_y.

S^2 terms   A few other parameters for high-order terms are conventionally used. D and E of the ZF Hamiltonian in Eq. (1.16) on p. 9 are

$$\frac{1}{3}DO_2^0 + EO_2^2 \qquad\qquad D = 3B_2^0 \qquad E = B_2^2 \ . \qquad\qquad (A.16)$$

S^4 terms   For high-spin systems, S^4 terms with parameters a and F are often used, with

$$\frac{F}{180}O_4^0(S) \qquad\qquad \frac{a}{120}\left[O_4^0(S) + 5O_4^4(S)\right] \ , \qquad\qquad (A.17)$$

so that

$$a = 24B_4^4 \qquad\qquad F = 180B_4^0 - 36B_4^4 \ . \qquad\qquad (A.18)$$

S^6 terms   For S^6 terms, only one conventional parameter is occasionally used

$$\frac{G}{1260}O_6^3 \quad \text{hence} \quad G = 1260B_6^3 \ . \qquad\qquad (A.19)$$

---

[1] Stevens introduced only operators with $q \geq 0$. In this form they were also given in the famous Table in [Abr86]. Later the set was extended to $q < 0$. Altogether they form a set of tesseral tensor operators. Spherical tensor operators are rarely used in EPR.

B Line shapes

This appendix summarises formulas for Gaussian and Lorentzian line shapes (see Figure B.1), just for reference. For a full discussion, see [Poo99].

x_0 denotes the centre of the line, Γ the distance between the inflection points of the zero derivative function, satisfying

$$\left.\frac{\partial^2}{\partial x^2} f(x, x_0, \Gamma)\right|_{x=x_0 \pm \Gamma} = 0 , \tag{B.1}$$

that is, Γ is the peak-to-peak distance in the first derivative of function f. Γ is therefore the preferred parameterisation of first derivative shapes as encountered in cw EPR and ENDOR. For absorption spectra (pulse EPR, pulse ENDOR, etc.), the full width at half height Γ_{FWHH} is more intuitive. Its conversion to Γ depends on the nature of the line shape function

$$\text{Lorentzian:} \quad \Gamma_{\text{FWHH}} = \sqrt{3}\Gamma \tag{B.2}$$

$$\text{Gaussian:} \quad \Gamma_{\text{FWHH}} = \sqrt{2\ln 2}\,\Gamma . \tag{B.3}$$

For a Lorentzian line shape we have

$$\int_{-\infty}^{x} f_{\text{L}}(y, x_0, \Gamma)\,\mathrm{d}y = \frac{1}{2} + \frac{1}{\pi}\arctan\left(\frac{2}{\sqrt{3}}\frac{x - x_0}{\Gamma}\right) \tag{B.4}$$

$$f_{\text{L}}(x, x_0, \Gamma) = \frac{2}{\pi\sqrt{3}}\frac{1}{\Gamma}\left[1 + \frac{4}{3}\left(\frac{x - x_0}{\Gamma}\right)^2\right]^{-1} \tag{B.5}$$

$$\frac{\partial}{\partial x}f_{\text{L}}(x, x_0, \Gamma) = -\frac{16}{3\pi\sqrt{3}}\frac{1}{\Gamma^2}\frac{x - x_0}{\Gamma}\left[1 + \frac{4}{3}\left(\frac{x - x_0}{\Gamma}\right)^2\right]^{-2} \tag{B.6}$$

For a Gaussian

$$\int_{-\infty}^{x} f_{\text{G}}(y, x_0, \Gamma)\,\mathrm{d}y = \frac{1}{2} + \frac{1}{2}\text{erf}\left(\sqrt{2}\frac{x - x_0}{\Gamma}\right) \tag{B.7}$$

$$f_{\text{G}}(x, x_0, \Gamma) = \sqrt{\frac{2}{\pi}}\frac{1}{\Gamma}e^{-2\left(\frac{x-x_0}{\Gamma}\right)^2} \tag{B.8}$$

$$\frac{\partial}{\partial x}f_{\text{G}}(x, x_0, \Gamma) = -4\sqrt{\frac{2}{\pi}}\frac{1}{\Gamma^2}\frac{x - x_0}{\Gamma}e^{-2\left(\frac{x-x_0}{\Gamma}\right)^2} \tag{B.9}$$
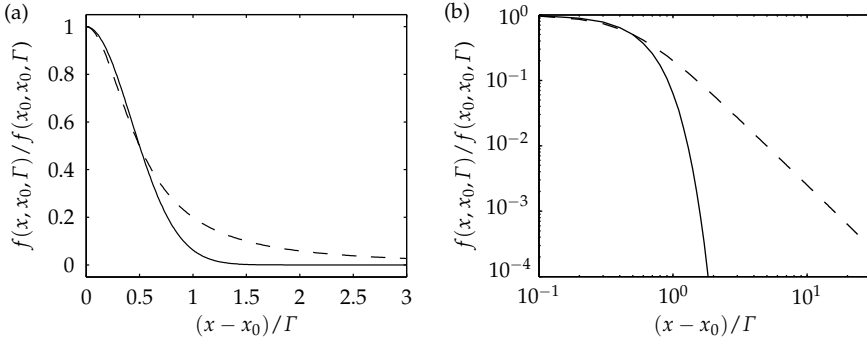
Figure B.1: Gaussian (solid) and Lorentzian (dashed) absorption line shape functions normalised to maximum amplitude 1. (a) Linear plot, (b) logarithmic plot.

The line shape functions $f_G(x)$ and $f_L(x)$ are normalised

$$\int_{-\infty}^{+\infty} f(x, x_0, \Gamma) \, dx = 1 \ . \tag{B.10}$$

Their values at $x = x_0$ are

$$f_L(x_0, x_0, \Gamma) = \frac{2}{\sqrt{3}\pi} \frac{1}{\Gamma} \qquad f_G(x_0, x_0, \Gamma) = \sqrt{\frac{2}{\pi}} \frac{1}{\Gamma} \ . \tag{B.11}$$

FT   The Fourier transform of a Gaussian is again Gaussian with $\Gamma_{FT} = 4/\Gamma$. The Fourier Transform of a Lorentzian is a exponential decay $e^{-t/\tau}$ with decay constant $\tau = 2/(\sqrt{3}\Gamma)$. For more details on these relationships, see [Poo87].

Convolution   The convolution of a Gaussian with line width Γ_1 with another Gaussian with line width Γ_2 gives again a Gaussian

$$f_G(x, x_1, \Gamma_1) * f_G(x, x_2, \Gamma_2) = f_G(x, x_1 + x_2, \Gamma) \quad \text{with} \quad \Gamma = \sqrt{\Gamma_1^2 + \Gamma_2^2} \ . \tag{B.12}$$

The convolution of a Lorentzian with a Gaussian (the so-called Voigt line shape) cannot be expressed in closed form. A close approximation is the pseudo-Voigt function

$$f_{pV}(x, x_0, \Gamma_G, \Gamma_L) = \alpha f_G(x, x_0, \Gamma_G) + (1 - \alpha) f_L(x, x_0, \Gamma_L) \tag{B.13}$$

with $0 \leq \alpha \leq 1$.

C Relative orientations

Relative orientations between two objects are usually defined by means of three rotation angles, the so-called Euler angles. Since their varying definitions[1] often cause confusion and they are difficult to grasp visually, this hopefully helpful appendix summarises definitions, formulas and two diagrams.

    In EPR, the relative orientation of an object (a matrix A or vector v) with respect to some reference object (the spectrometer, the molecule, the g matrix) is usually specified by the passive rotation R which transforms the coordinate system, in which the object is represented, into that of the reference object

$$v' = Rv \qquad A' = RAR^{\mathrm{T}} \, .\tag{C.1}$$

So the rotation is passive with respect to the object (it leaves its spatial orientation untouched, $v' \cong v$, $A' \cong A$), but *active* with respect to its frame of representation.

    Any relative orientation between a starting frame xyz and another frame XYZ can be described by three subsequent elementary rotations (see Figure C.1)

1. Rotation of xyz by angle α counterclockwise around the z axis gives a new frame $x'y'z'$ with $z' = z$.

2. Rotation of $x'y'z'$ by angle β counterclockwise around the new y' axis gives a new frame $x''y''z''$ with $y'' = y'$.

3. Rotation of $x''y''z''$ by angle γ counterclockwise around the new z'' axis gives the new frame XYZ with $Z = z''$.

The rotation matrix describing the transformation is

$$R(\alpha, \beta, \gamma) = R_{z''}(\gamma) R_{y'}(\beta) R_z(\alpha) \tag{C.2}$$

$$= \begin{pmatrix} c\gamma & s\gamma & 0 \\ -s\gamma & c\gamma & 0 \\ 0 & 0 & 1 \end{pmatrix} \begin{pmatrix} c\beta & 0 & -s\beta \\ 0 & 1 & 0 \\ s\beta & 0 & c\beta \end{pmatrix} \begin{pmatrix} c\alpha & s\alpha & 0 \\ -s\alpha & c\alpha & 0 \\ 0 & 0 & 1 \end{pmatrix} \tag{C.3}$$

$$= \begin{pmatrix} c\gamma c\beta c\alpha - s\gamma s\alpha & c\gamma c\beta s\alpha + s\gamma c\alpha & -c\gamma s\beta \\ -s\gamma c\beta c\alpha - c\gamma s\alpha & -s\gamma c\beta s\alpha + c\gamma c\alpha & s\gamma s\beta \\ s\gamma c\alpha & s\beta s\alpha & c\beta \end{pmatrix} \tag{C.4}$$

---

[1] The definitions here are used in [Sch01]. In NMR and angular momentum theory, other definitions are sometimes used, using active instead of passive rotations or other axes for the three elementary rotations.
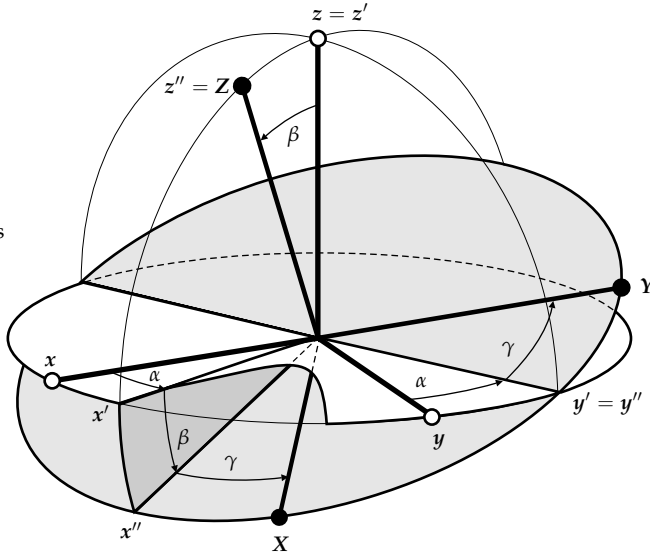
Figure C.1: Relative orientation between two frames *xyz* and *XYZ* described by three Euler angles α, β, and γ.

with the abbreviations $c\alpha = \cos\alpha$, $s\alpha = \sin\alpha$, etc. $\boldsymbol{R}$ is a special orthogonal matrix

$$\det(\boldsymbol{R}) = 1 \qquad \boldsymbol{R}^{-1} = \boldsymbol{R}^{\mathrm{T}} \ . \tag{C.5}$$

Ambiguity   The Euler angles are not a unique parameterisation for $\boldsymbol{R}$, there are several angle triplets that give the same $\boldsymbol{R}$ as (α, β, γ)

$$\begin{aligned}
\boldsymbol{R}(\alpha, \beta, \gamma) &= \boldsymbol{R}(\alpha \pm \pi, -\beta, \gamma \pm \pi) \\
&= \boldsymbol{R}^{\mathrm{T}}(-\gamma, -\beta, -\alpha) = \boldsymbol{R}^{\mathrm{T}}(\pm\pi - \gamma, \beta, \pm\pi - \alpha) \ .
\end{aligned} \tag{C.6}$$

In the special case $\beta = 0$, the first and the third rotation degenerate, that is, they are around the same axis ($\boldsymbol{z} = \boldsymbol{z}''$), and α and γ cannot be distinguished, since $\boldsymbol{R}(\alpha, 0, \gamma) = \boldsymbol{R}(0, 0, \alpha + \gamma) = \boldsymbol{R}(\alpha + \gamma, 0, 0)$ etc. The transformation $(\alpha, \beta, \gamma) \to \boldsymbol{R}$ is unique, if one restricts the domain of the angles, e.g.

$$0 < \alpha \leq \pi, \quad \beta > 0, \quad 0 < \gamma < \pi \ . \tag{C.7}$$

With this domain restriction, it is possible to compute the angles from a given $\boldsymbol{R}$.

Publications

Conference posters

P1 S. Stoll and A. Schweiger, *A MATLAB toolbox for modelling EPR spectra*. EMARDIS'99 Conference, Sofija, Bulgaria (1999)

P2 S. Stoll and A. Schweiger, *Generalized Frequency Domain Calculations of Pulse EPR Spectra of Disordered Systems*. 23rd International EPR Symposium at the Rocky Mountain Conference on Analytical Chemistry, Denver, USA (2000)

Conference talks

T1 *Pulse EPR investigations of axially coordinated Co(II)-heptamethyl corbyrinate, a coenzyme B_{12} model*. EMARDIS'99, Sofija, Bulgaria (1999)

T2 *Advances in EPR Spectral Simulations of Disordered Systems*. Annual Meeting of the Israel Magnetic Resonance Club, Haifa, Israel (2001)

T3 *Fast and accurate construction of time-domain signals in frequency domain simulations of ESEEM spectra of disordered systems*. 14th ISMAR conference, Rhodes, Greece (2001)

T4 *New approaches in computational EPR spectroscopy*. Colloquium, Laboratory of Physical Chemistry, ETH Zürich, Switzerland (2002)

T5 *A Robust and Fast Algorithm for the Computation of cw EPR Resonance Fields*. EPR group meeting of the Royal Society of Chemistry, Manchester, UK (2003)

Reviewed articles

A1 S. Stoll, G. Jeschke, M. Willer and A. Schweiger, *Nutation-Frequency Correlated EPR Spectroscopy: The PEANUT Experiment*. J. Magn. Reson. **130**(1), 86–96 (1998)

A2 S. Van Doorslaer, J. J. Shane, S. Stoll, A. Schweiger, M. Kranenburg and R. J. Meier. *Continuous wave and pulse EPR as a tool for the characterization of monocyclopentadienyl Ti(III) catalysts*. J. Organomet. Chem. **634**(2), 185–192 (2001)

A3 S. Stoll and A. Schweiger, *Rapid Construction of Time-Domain Signals from Frequencies and Amplitudes*. J. Magn. Reson., in print (2003)

A4 S. Stoll and A. Schweiger, *A Robust and Fast Algorithm for the Computation of cw EPR Resonance Fields*. In preparation.

A5 S. Stoll and A. Schweiger, *Adaptive orientation meshes for the simulation of magnetic resonance spectra of disordered systems*. In preparation.

A6 S. Stoll and A. Schweiger, *Frequency-domain simulation of ESEEM spectra*. In preparation.

Bibliography

[Aas75]   R. Aasa and T. Vänngård, *EPR Signal Intensity and Powder Shapes: A Reexamination*. J. Magn. Reson. **19**(3), 308–315 (1975)

[Abr86]   A. Abragam and B. Bleaney, *Electron Paramagnetic Resonance of Transition Ions*. Dover (1986)

[Ald86]   D. W. Alderman, M. S. Solum and D. M. Grant, *Methods for analyzing spectroscopic line shapes. NMR solid powder patterns*. J. Chem. Phys. **84**(7), 3717–3725 (1986)

[Alt74]   S. A. Altshuler and B. M. Kozyrev, *Electron Paramagnetic Resonance in Compounds of Transition Elements*. Wiley, 2nd edn. (1974)

[And99]   E. Anderson, Z. Bai, C. Bischof, J. Demmel, J. Dongarra, J. D. Croz, A. Greenbaum, S. Hammarling, A. McKenney, S. Ostrouchov and D. Sorensen, *LAPACK's User's Guide*. Society for Industrial and Applied Mathematics, 3rd edn. (1999), ISBN 0-89871-294-7

[Ast02]   A. V. Astashkin and A. M. Raitsimring, *Electron spin echo envelope modulation theory for high electron spin systems in weak crystal field*. J. Chem. Phys. **117**(13), 6121–6132 (2002)

[Aug85]   J. M. Augenbaum and C. S. Peskin, *On the Construction of the Voronoi Mesh on a Sphere*. J. Comput. Phys. **59**(2), 177–192 (1985)

[Bai00]   W. C. Bailey, *DFT and HF–DFT calculations of ^{14}N quadrupole coupling constants in molecules*. Chem. Phys. **252**(1–2), 57–66 (2000)

[Bak97]   M. Bak and N. C. Nielsen, *REPULSION, A Novel Approach to Efficient Powder Averaging in Solid-State NMR*. J. Magn. Reson. **125**(1), 181–190 (1997)

[Bak00]   M. Bak, J. T. Rasmussen and N. C. Nielsen, *SIMPSON: A General Simulation Program for Solid-State NMR Spectroscopy*. J. Magn. Reson. **147**(2), 296–330 (2000)

[Bar96]   C. B. Barber, D. P. Dobkin and H. Huhdanpaa, *The Quickhull Algorithm for Convex Hulls*. ACM Trans. Math. Softw. **22**(4), 469–483 (1996)

[Bel73]   G. G. Belford, R. L. Belford and J. F. Burkhalter, *Eigenfields: A Practical Direct Calculation of Resonance Fields and Intensities for Field-Swept Fixed-Frequency Spectrometers*. J. Magn. Reson. **11**(2), 251–265 (1973)

[Bel74]   R. L. Belford, P. H. Davies, G. G. Belford and T. M. Lenhardt, *Computation of Field-Swept EPR Spectra for Systems with Large Interelectronic Interactions*. Am. Chem. Soc. Symp. Ser. **5**, 40–50 (1974)

[Bel96]   V. Beltrán-López, B. Mile and C. C. Rowlands, *Exact analytical solution for the powder pattern of orthorhombic-g systems*. J. Chem. Soc., Farad. Trans. **92**(12), 2303–2310 (1996)

[Bel99]   V. Beltrán-López, *Closed Form Solutions in EPR Computer Simulations*. Mol. Phys. Rep. **26**, 25–38 (1999)

[Ben90]   A. Bencini and D. Gatteschi, *EPR of exchange coupled systems*. Springer (1990)

[Ben02]   N. P. Benetis, P. C. Dave and D. Goldfarb, *Characteristics of ESEEM and HYSCORE spectra of $S > 1/2$ centers in orientationally disordered systems*. J. Magn. Reson. **158**(1–2), 126–142 (2002)

[Bla02]   W. B. Blanton, *High Performance Computations in NMR*. Ph.D. thesis, University of California, Berkeley (2002)

[Bro00]   J. M. Brown, R. J. Buenker, A. Carrington, C. di Lauro, R. N. Dixon, R. W. Field, J. T. Hougen, W. Hüttner, K. Kuchitsu, M. Mehring, A. J. Merer, T. A. Miller, M. Quack, D. A. Ramsay, L. Veseth and R. Zare, *Remarks on the signs of g factors in atomic and molecular Zeeman spectroscopy*. Mol. Phys. **98**(20), 1597–1601 (2000)

[Cha98]   T. Charpentier, C. Fermon and J. Virlet, *Efficient Time Propagation Technique for MAS NMR Simulation: Application to Quadrupolar Nuclei*. J. Magn. Reson. **132**(2), 181–190 (1998)

[Čug94]   L. Čugunov, A. Mednis and J. Kliava, *Computer Simulations of the EPR Spectra for Ions with S>1/2 by the Eigenfield and Related Methods*. J. Magn. Reson. A **106**(2), 153–158 (1994)

[dB97]   M. de Berg, M. van Kreveld, M. Overmars and O. Schwarzkopf, *Computational Geometry: algorithms and applications*. Springer (1997)

[Ebe83]   H. Ebert, J. Abart and J. Voitländer, *Simulation of quadrupole disturbed NMR field spectra by using perturbation theory and the triangle integration method*. J. Chem. Phys. **79**(10), 4719–4723 (1983)

[Edé98]   M. Edén and M. H. Levitt, *Computation of Orientational Averages in Solid-State NMR by Gaussian Spherical Quadrature*. J. Magn. Reson. **132**(2), 220–239 (1998)

[Epe00]   B. Epel and D. Goldfarb, *Two-Dimensional Pulsed TRIPLE at 95 GHz*. J. Magn. Reson. **146**(1), 196–203 (2000)

[Epe01]   B. Epel, A. Pöppl, P. Manikandan, S. Vega and D. Goldfarb, *The Effect of Spin Relaxation on ENDOR Spectra Recorded at High Magnetic Fields and Low Temperatures*. J. Magn. Reson. **148**(2), 388–397 (2001)

[Ern89]   R. R. Ernst, G. Bodenhausen and A. Wokaun, *Principles of Nuclear Magnetic Resonance in One and Two Dimensions*, vol. 14 of *Interantional Series of Monographcs on Chemistry*. Oxford University Press (1989)

[Fer50]   E. Fermi, *Nuclear Physics*. University of Chicago Press (1950)

[Fey39]   R. P. Feynman, *Forces in Molecules*. Phys. Rev. **56**, 340–343 (1939)

[Fri80]   F. N. Frisch and R. E. Carlson, *Monotone Piecewise Cubic Interpolation*. SIAM J. Numer. Anal. **17**(2), 238–246 (1980)

[Gaf93]   B. J. Gaffney and H. J. Silverstone, *Simulation of the EMR Spectra of High-Spin Iron in Proteins*. Biol. Magn. Reson. **13**, 1–57 (1993)

[Gaf98]   B. J. Gaffney and H. J. Silverstone, *Simulation Methods for Looping Transitions*. J. Magn. Reson. **134**(1), 57–66 (1998)

[Gal81]   S. Galindo and L. Gonzáles-Tovany, *Monte Carlo Simulation of EPR Spectra of Polycrystalline Samples*. J. Magn. Reson. **44**(2), 250–254 (1981)

[Gat98]   K. E. Gates, M. Griffin, G. H. Hanson and K. Burrage, *Computer Simulation of Magnetic Resonance Spectra Employing Homotopy*. J. Magn. Reson. **135**(1), 103–112 (1998)

[Gle91]   J. Glerup and H. Weihe, *Magnetic Susceptibility and EPR Spectra of µ-Cyano-bis[pentaaminechromium(III)] perchlorate*. Acta Chem. Scand. **45**, 444–448 (1991)

[Gol96]   G. H. Golub and C. F. V. Loan, *Matrix computations*. Johns Hopkins University Press, 3rd edn. (1996)

[Gra01]   V. Grachëv, *Double spiral and fractal approaches for calculations of EPR and NMR spectra in amorphous solids and powders*, Specialized Colloque AMPERE, Stuttgart (2001)

[Gri90]   G. C. M. Gribnau, J. L. C. van Tits and E. J. Reijerse, *An Efficient General Algorithm for the Simulation of Magnetic Resonance Spectra of Orientationally Disordered Solids*. J. Magn. Reson. **90**(3), 474–485 (1990)

[Gri99]   M. Griffin, A. Muys, C. Noble, D. Wang, C. Eldershaw, K. E. Gates, K. Burrage and G. R. Hanson, *XSophe, a Computer Simuation Software Suite for the Analysis of Electron Paramagnetic Resonance Spectra*. Mol. Phys. Rep. **26**, 60–84 (1999)

Bibliography

[Hag85a] W. R. Hagen, D. O. Hearshen, L. J. Harding and W. R. Dunham, *Quantitative Numerical Analysis of g Strain in the EPR of Distributed Systems and Its Importance for Multicenter Metalloproteins*. J. Magn. Reson. **61**(2), 233–244 (1985)

[Hag85b] W. R. Hagen, D. O. Hearshen, R. H. Sands and W. R. Dunham, *A Statistical Theory for Powder EPR in Distributed Systems*. J. Magn. Reson. **61**(2), 220–232 (1985)

[Hoh99] M. Hohwy, H. Bildsoe, H. J. Jakobsen and N. C. Nielsen, *Efficient Spectral Simulations in NMR of Rotating Solids. The γ-COMPUTE Algorithm*. J. Magn. Reson. **136**(1), 6–14 (1999)

[Hub96] M. Hubrich, G. Jeschke and A. Schweiger, *The generalized hyperfine sublevel coherence transfer experiment in one and two dimensions*. J. Chem. Phys. **104**(6), 2172–2184 (1996)

[Hyd90] J. S. Hyde, M. Pasenkiewicz-Gierula, A. Jesmanowicz and W. E. Antholine, *Pseudo Field Modulation EPR Spectroscopy*. Appl. Magn. Reson. **1**, 483–496 (1990)

[Jen99] F. Jensen, *Introduction to Computational Chemistry*. Wiley (1999)

[Kat82] T. Kato, *A Short Introduction to Perturbation Theory for Linear Operators*. Springer (1982)

[Kau02a] M. Kaupp, C. Remenyi, J. Vaara, O. L. Malkina and V. G. Malkin, *Density Functional Calculations of Electronic g-Tensors for Semiquinone Radical Anions. The Role of Hydrogen Bonding and Substituent Effects*. J. Am. Chem. Soc. **124**(11), 2709–2722 (2002)

[Kau02b] M. Kaupp, R. Reviakine, O. L. Malkina, A. Arbuznikov, B. Schimmelpfennig and V. G. Malkin, *Calculation of Electronic g-Tensors for Transition Metal Complexes Using Hybrid Density Functionals and Atomic Meanfield Spin-Orbit Operators*. J. Comput. Chem. **23**(8), 794–803 (2002)

[Kei87] C. P. Keijzers, E. J. Reijerse, P. Stam, M. F. Dumont and M. C. M. Gribnau, *MAGRES: A General Program for Electron Spin Resonance, ENDOR and ESEEM*. J. Chem. Soc., Faraday Trans. 1 **83**(12), 3493–3503 (1987)

[Kne60] F. K. Kneubühl, *Line Shapes of Electron Paramagnetic Resonance Signals Produced by Powders, Glasses and Viscous Liquids*. J. Chem. Phys. **33**(4), 1074–1078 (1960)

[Kno99] G. D. Knott, *Interpolating Cubic Splines*. Birkhäuser (1999)

[Koo95] J. M. Koons, E. Hughes, H. M. Cho and P. D. Ellis, *Extracting Multitensor Solid-State NMR Parameters from Lineshapes*. J. Magn. Reson. A **114**(1), 12–23 (1995)

[Kre91]   A. Kreiter and J. Hüttermann, *Simultaneous EPR and ENDOR Powder-Spectra Synthesis by Direct Hamiltonian Diagonalization*. J. Magn. Reson. **93**(1), 12–26 (1991)

[Kva00]   B. I. Kvasov, *Shape-Preserving Spline Approximation*. World Scientific (2000)

[Käl03]   M. Kälin, I. Gromov and A. Schweiger, *The cw EPR experiment revisited*. J. Magn. Reson. (2003)

[Lév67]   J.-M. Lévy-Leblond, *Nonrelativistic Particles and Wave Equations*. Commun. Math. Phys. **6**, 286–311 (1967)

[Mab92]   F. E. Mabbs and D. Collison, *Electron Paramagnetic Resonance of d Transition Metal Compounds*, vol. 16 of *Studies in Inorganic Chemistry*. Elsevier (1992)

[Mac69]   J. H. Mackey, M. Kopp, E. C. Tynan and T. F. Yen, *Computer synthesis of Electron Paramagnetic Resonance Spectra from a Parametric(Spin) Hamiltonian*. In T. F. Yen (ed.), *Electron Spin Resonance of Metal Complexes*, 33–57, Plenum Press (1969)

[Mád02]   Z. Mádi, S. Van Doorslaer and A. Schweiger, *Numerical Simulation of One- and Two-Dimensional ESEEM Experiments*. J. Magn. Reson. **154**(2), 181–191 (2002)

[Mim65]   W. B. Mims, *Electron Echo Methods in Spin Resonance Spectroscopy*. Rev. Sci. Instr. **36**(10), 1472–1479 (1965)

[Mis76]   S. K. Misra, *Evaluation of Spin-Hamiltonian Parameters from EPR data by the Method of Least-Squares Fitting*. J. Magn. Reson. **23**(3), 403–410 (1976)

[Mis99]   S. K. Misra, *A Rigorous Evaluation of Spin-Hamiltonian Parameters and Linewidth from a Polycrystalline EPR Spectrum*. J. Magn. Reson. **140**(1), 179–188 (1999)

[Mom92]   M. J. Mombourquette and J. A. Weil, *Simulation of Magnetic Resonance Powder Spectra* . J. Magn. Reson. **99**(1), 37–44 (1992)

[Mor99]   G. Morin and D. Bonnin, *Modeling EPR Powder Spectra Using Numerical Diagonalization of the Spin Hamiltonian*. J. Magn. Reson. **136**(2), 176–199 (1999)

[Mun99]   M. Munzarová and M. Kaupp, *A Critical Validation of Density Functional and Coupled-Cluster Approaches for the Calculation of EPR Hyperfine Coupling Constants in Transition Metal Complexes*. J. Phys. Chem. A **103**(48), 9966–9983 (1999)

[Mun00] M. Munzarová and M. Kaupp, *Mechanisms of EPR Hyperfine Coupling in Transition Metal Complexes*. J. Am. Chem. Soc. **122**(48), 11900–11913 (2000)

[Nee98] F. Neese and E. I. Solomon, *Calculation of Zero-Field Splittings, g-Values, and the Relativistic Nephelauxetic Effect in Transition Metal Complexes. Application to High-Spin Ferric Complexes*. Inorg. Chem. **37**(26), 6568–6582 (1998)

[Net85] D. Nettar and J. J. Villafranca, *A Program for EPR Powder Spectrum Simulation*. J. Magn. Reson. **64**(1), 61–65 (1985)

[Nic00] P. Nicholas, D. Fushman, V. Ruchinsky and D. Cowburn, *The Virtual NMR Spectrometer: A Computer Program for Efficient Simulation of NMR Experiments Involving Pulsed Field Gradients*. J. Magn. Reson. **145**(2), 262–275 (2000)

[Nil79] M. J. Nilges, *Electron paramagnetic resonance studies of low symmetry nickel(I) and molybdenum(V) complexes*. Ph.D. thesis, University of Illinois, Urbana (1979)

[Nob02a] C. J. Noble, G. R. Hanson and K. E. Gates, *Strategies for the efficient computer simulation of pulsed electron paramagnetic resonance spectra*, 44th Rocky Mountain Conference on Analytical Chemistry, Denver, USA (2002)

[Nob02b] C. J. Noble, G. R. Hanson and K. E. Gates, *XSophe, A Computer Simulation Software Suite (V 1.1) and its Application to the Analysis of EPR Spectra from the Molybdoenzyme Dimethylsulfide Dehydrogenase*, 44th Rocky Mountain Conference on Analytical Chemistry, Denver, USA (2002)

[Oka00] A. Okabe, B. Boots, K. Sugihara and S. N. Chiu, *Spatial Tessellations. Concepts and Applications of Voronoi Diagrams*. Wiley, 2nd edn. (2000)

[Oli96] P. B. Oliete, V. M. Orera and P. J. Alonso, *Structure of the Jahn-Teller distorted Cr^2+ defect in SrF_2:Cr by electron-spin-echo envelope modulation*. Phys. Rev. B **54**(17), 12100–12108 (1996)

[Opp01] A. V. Oppenheim and R. W. Schafer, *Discrete-Time Signal Processing*. Prentice Hall, Englewood Cliffs, New Jersey (2001)

[Pil90] J. Pilbrow, *Transition Ion Electron Paramagnetic Resonance*. Clarendon Press (1990)

[Pil99] J. R. Pilbrow and A. Rockenbauer (eds.), *Computer Simulations in EPR Spectroscopy*, vol. 26 of *Mol. Phys. Rep.* Polish Academy of Sciences (1999)

[Pon97]   A. Ponti, *Electron-Spin-Echo Envelope Modulation Arising from Hyperfine Coupling to a Nucleus of Arbitrary Spin*. J. Magn. Reson. **127**(1), 87–104 (1997)

[Pon99a]   A. Ponti, *Simulation of Magnetic Resonance Static Powder Lineshapes: A Quantitative Assessment of Spherical Codes*. J. Magn. Reson. **138**(2), 288–297 (1999)

[Pon99b]   A. Ponti, *Simulation of one-dimensional magnetic resonance powder lineshapes reduced to area computation*. Chem. Phys. Lett. **302**(3–4), 224–230 (1999)

[Poo87]   C. P. Poole and H. A. Farach, *Theory of Magnetic Resonance*. Wiley, 2nd edn. (1987)

[Poo99]   C. P. Poole and H. A. Farrach (eds.), *Handbook of Electron Spin Resonance*, vol. 2. Springer (1999)

[Pre92]   W. H. Press, S. A. Teukolsky, W. T. Vetterling and B. P. Flannery, *Numerical Recipes in C*. Cambridge University Press, 2nd edn. (1992)

[Rud87]   C. Rudowicz, *Concept of Spin Hamiltonian, Forms of Zero Field Splitting and Electronic Zeeman Hamiltonians and Relations between Parameters used in EPR. A Critical Review*. Magn. Reson. Rev. **13**(1), 1–89 (1987)

[Rud01]   C. Rudowicz and S. K. Misra, *Spin-Hamiltonian Formalisms in Electron Magnetic Resonance (EMR) and Related Spectroscopies*. Appl. Spectrosc. Rev. **36**(1), 11–63 (2001)

[Sak85]   J. J. Sakurai, *Modern Quantum Mechanics*. Addison-Wesley (1985)

[Sam95]   M. Sambridge, J. Braun and H. McQueen, *Geophysical parameterization and interpolation of irregular data using natural neighbors*. Geophys. J. Int. **122**(3), 837–857 (1995)

[Sch89]   D. J. Schneider and J. H. Freed, *Calculating Slow Motional Magnetic Resonance Spectra: A User's Guide*. Biol. Magn. Reson. **8**, 1–76 (1989)

[Sch98]   G. Schreckenbach and T. Ziegler, *Density functional calculations of NMR chemical shifts and ESR g-tensors*. Theor. Chem. Acc. **99**(2), 71–82 (1998)

[Sch01]   A. Schweiger and G. Jeschke, *Principles of pulse electron paramagnetic resonance*. Oxford University Press (2001)

[Scu82]   M. I. Scullane, L. K. White and N. D. Chasteen, *An Efficient Approach to Computer Simulation of EPR Spectra of High-Spin Fe(III) in Rhombic Ligand Fields*. J. Magn. Reson. **47**(3), 383–397 (1982)

[Sha98]   J. J. Shane, L. P. Liesum and A. Schweiger, *Efficient Simulation of ESEEM Spectra Using Gamma*. J. Magn. Reson. **134**(1), 72–75 (1998)

[Sid98]   R. B. Sidje, *Expokit: A Software Package for Computing Matrix Exponentials*. ACM Trans. Mathem. Softw. **24**(1), 130–156 (1998)

[Sig77]   R. Sigl, *Ebene und sphärische Trigonometrie: mit Anwendungen auf Kartographie, Geodäsie und Astronomie*. Wichmann (1977)

[Smi94]   S. A. Smith, T. O. Levante, B. H. Meier and R. R. Ernst, *Computer-simulations in Magnetic Resonance—An object-oriented programming approach*. J. Magn. Reson. A **106**(1), 75–105 (1994)

[Sta02]   C. Stadler, A. L. de Lacey, B. Hernández, V. M. Fernández and J. C. Conesa, *Density Functional Calculations for Modeling the Oxidized States of the Active Site of Nickel-Iron Hydrogenases. 1. Verification of the Method with Paramagnetic Ni and Co Complexes*. Inorg. Chem. **41**(17), 4417–4423 (2002)

[Swa64]   J. D. Swalen and H. M. Gladney, *Computer Analysis of Electron Paramagnetic Resonance Spectra*. IBM J. Res. Dev. **8**(5), 515–526 (1964)

[Szo98]   R. Szosenfogel and D. Goldfarb, *Simulations of HYSCORE spectra obtained with ideal and non-ideal pulses*. Mol. Phys. **95**(6), 1295–1308 (1998)

[Tay75]   P. C. Taylor, J. F. Baugher and H. M. Kritz, *Magnetic Resonance Spectra in Polycrystalline Solids*. Chem. Rev. **75**(2), 203–240 (1975)

[Van99]   S. Van Doorslaer, G. Sierra and A. Schweiger, *Dead Time-Dependent Line Distortions in Absolute-Value Electron Spin Echo Envelope Modulation Spectra*. J. Magn. Reson. **136**(2), 152–158 (1999)

[Var96]   S. J. Varner, R. L. Vold and G. L. Hoatson, *An Efficient Method for Calculating Powder Patterns*. J. Magn. Reson. A **123**(1), 72–80 (1996)

[vV78]   G. van Veen, *Simulation and Analysis of EPR Spectra of Paramagnetic Ions in Powders*. J. Magn. Reson. **30**(1), 91–109 (1978)

[Wan95]   D. Wang and G. R. Hanson, *A New Method for Simulating Randomly Oriented Powder Spectra in Magnetic Resonance: The Sydney Opera House (SOPHE) Method*. J. Magn. Reson. A **117**(1), 1–8 (1995)

[Wan96]   D. Wang and G. R. Hanson, *New Methodologies for Computer Simulation of Paramagnetic Resonance Spectra*. Appl. Magn. Reson. **11**(3–4), 401–415 (1996)

[Was64]   E. Wasserman, L. C. Snyder and W. A. Yager, *ESR of the Triplet States of Randomly Oriented Molecules*. J. Chem. Phys. **41**(6), 1763–1772 (1964)

[Wat86]   D. F. Watson, *Contouring. A Guide to the Analysis and Display of Spatial Data*, vol. 10 of *Computer Methods in the Geoscience*. Pergamon Press (1986)

[Wei94]   J. A. Weil, J. R. Bolton and J. E. Wertz, *Electron Paramagnetic Resonance*. Wiley (1994)

Curriculum vitae

Personal details
Birth   27 October 1973 in Meran, Italy
Citizenship   Italy and Austria

Education, main line
1987–1992   High school "A. Einstein" (Meran), gradutation with 60 of 60 points
1992–1997   Technical Chemistry at TU Graz, Austria
                    1st and 2nd diploma with distinction
1998–2003   PhD student at ETHZ Zürich (Prof. A. Schweiger)

Education, additional
1992   Special award "Alfiere del Lavoro" from Italian president
                    for outstanding achievements
1991, 1992   1st prize at the Chemistry Olympiad in Austria
1992   3rd at the International Chemistry Olympiad in Pittsburgh (USA)
1995   Vising student at the Academy of Sciences in Sofija, Bulgaria (2 months)
1996   Visiting student at ETH Zürich, Switzerland. Master's thesis (6 months)
1996   In addition Russian and French at University of Graz
1997   Completion of Technical Chemistry Course, with distinction
1998   Visiting student at State University Moscow (2 months),learning Russian
2000   Visiting student at Weizmann Institute of Science, Israel (3 months)

Musical Activities
1990–1992   Conservatory "C. Monteverdi", Bozen, Italy
1997   Final diploma in Bozen, cum laude
1992–2000   Flute at the Academy of Music, Graz, Austria
                    1st and 2nd diploma with distinction

Repeatedly prices at youth competitions, many chamber music concerts throughout Europe. Occasional perfomances in the Vienna Philharmonic Orchestra since 1999. Participation in several international music competitions, including Barcelona (1996), Munich (2000).

Other activities
1991   Programmer for accounting software (3 months)
1994–1998   Chief editor of a students' magazine
1997   Internship at McKinsey&Co, Vienna (2 months)

Languages and Certificates
Languages   German (mother tongue), Italian and English (proficient)
                    Russian (advanced), French (intermediate)
Certificates   TOEFL 640 total score (1995), GMAT 99% below (1996)
                    GRE general 90% below (1995), GRE chemistry 90% below (1995)